공학박사 학위논문

다양한 열유동부하 시스템의 반응 유동 및 구조 상호작용 해석을 위한 3차원 코드 개발 연구

Development of 3D Software for Analysis of Reactive Flow and Structure Interaction in Various Thermal Hydrodynamic Loading Systems

2019년 2월

서울대학교 대학원

기계항공공학부

이 영 헌

다양한 열유동부하 시스템의 반응 유동 및 구조 상호작용 해석을 위한 3차원 코드 개발 연구

Development of 3D Software for Analysis of Reactive Flow and Structure Interaction in Various Thermal Hydrodynamic Loading Systems

지도 교수 여 재 익

이 논문을 공학박사 학위논문으로 제출함

2018년 12월

서울대학교 대학원

기계항공공학부

이 영 헌

이영헌의 공학박사 학위논문을 인준함

2018년 12월

위 원 장 _____ (인)

부위원장 _____ (인)

위 원 _____ (인)

위 원 _____ (인)

위 원 _____ (인)

Abstract

Development of 3D Software for Analysis of Reactive Flow and Structure Interaction in Various Thermal Hydrodynamic Loading Systems

Younghun Lee
Mechanical and Aerospace Engineering
The Graduate School
Seoul National University

Previously researched fluid-structure interaction analysis has mostly simulated an interaction between a structure and non-reactive flow, which does not consider the chemical reaction in flow. In the interaction analysis of large deformation of a structure due to high temperature and pressure flow accompanied by chemical reactions such as explosion or combustion, it is difficult to apply the geometry of the deformed structure to the fluid flow domain. In this reason, many studies have not been conducted to simultaneously analyze the interaction between the reactive flow and the structure deformation. Instead, the temperature and pressure conditions of the flow field analyzed in the body are applied to the boundary conditions of the

structure analysis. In this case, the flow could not be interpreted according to the behavior of the structure, so the exact pressure and temperature near the structure could not be calculated. In this study, a three-dimensional simulation techniques were developed for analyze the reactive flow including the chemical reaction with the large deformation of structure. The numerical code is verified by comparing the simulation results with the experimental values.

In this study, various reactive flows were considered. The ethylene-air mixture and the kerosene-air mixture, which are gaseous high energy materials, simulate the combustion reaction through the 1-step Arrhenius equation. In addition, combustion characteristics of anisotropic PETN and HMX, which are solid energetic materials, were analyzed by using the modified anisotropic I&G model. The developed combustion model compared the C-J condition and the detonation cell size. Structure deformation was performed by using Eulerian or Lagrangian analysis method and the method was verified by comparing with the experimental data of Taylor impact problem. A level set technique and a ghost fluid method (GFM) were used to set boundary values and trace the interface between the reactive flow and the structure. In order to verify the multi-material analysis method, the cantilever motion in the flow field and the tube deformation problem due to detonation load were simulated. The numerical results are verified by comparing with the theoretical and experimental values. For the three dimensional simulation, the STL file to level converting algorithm was developed. Moreover, the adaptive

mesh refinement (AMR) and message passing interface (MPI) for parallel processing were conducted to reduce the computation time and resources.

The interactions between reactive flow and structure under various thermal hydrodynamic loading systems were analyzed based by developed code. The behavior of rear cover which is deformed by the launching rocket plume inside a vertical launching system (VLS) is analyzed. This analysis results were verified by comparing with the experimental data, and the influence of rear cover deformation on the flow was confirmed through the analysis results. In addition, the explosion of the solid explosives in the three-dimensional concrete building, which cannot be simplified in two dimensions, and the pressure transmitted to the wall are analyzed. The numerical analysis results were compared with experimental data. In the analysis of tube deformation due to detonation inside the metal tube was simulated. The yield stress of metal tube is dependent on wall temperature and thermal softening was considered. In case of pulse detonation engine (PDE), which is exposed to high temperature environment, accurate results can be obtained by using temperature dependent properties and simulation results verified by comparison with theoretical failure model. The elastically vibrating tube was considered for detonation inside the PDE simulation. Due to the repetitively detonation propagation inside PDE, the PDE wall is vibrated with its natural frequency even if the PDE does not be destroyed. The simulation results confirms that propagation of detonation is affected by the deformation of tube.

Keywords: Gaseous energetic material, Solid energetic material, Detonation, Elasto-plastic deformation, Multi-material analysis, Reactive fluid-structure interaction analysis

Student Number: 2014-30357

Contents

List of Tables

List of Figures

Preface

This thesis is based on the following publications and manuscripts.

Paper 1
Younghun Lee, Min-cheol Gwak, Heaseong Cho, Hyun Shig Joo, Sang Joon Shin, and Jack J. Yoh, "Numerical Simulation of Fluid-Structure Interaction Problem Associated with Vertical Launching System," *Journal of spacecraft and Rockets*, Vol. 55, No. 4, pp. 948-958, 2018

Paper 2
Min-cheol Gwak, Younghun Lee, and Jack J. Yoh, "Numerical Investigation of Kerosene-Based Pulse-Detonation Loading on the Metal Tubes," *Journal of Propulsion and Power*, Vol. 32, No. 5, pp. 1146-1152, 2016

Paper 3
Min-cheol Gwak, Younghun Lee, Ki-hong Kim, Haeseong Cho, Sang Joon Shin, and Jack J. Yoh, "All Eulerian method of computing elastic response of explosively pressurised metal tube," *Combustion Theory and Modelling*, Vol. 21, No. 2, pp. 293-308, 2017

Paper 4
Younghun Lee, Woong-Hyun Lee, Min-chel Gwak, Kihong Kim, and Jack J. Yoh, "A reactive flow simulation for the anisotropic ignition of an explosive crystal using adaptive mesh refinement," *Journal of Applied Physics*, Vol. 124, 145903, 2018.

Paper 5
HyunShig Joo, Haeseong Cho, Younghun Lee, SangJoon Shin, Jack J. Yoh, Jae-Cheol Shin, "Parametric study of a VLS based on 2-D FSI analysis," *Aerospace Science and Technology*, Vol. 84, No. 1, pp.530-542, 2019.

Chapter 1. Introduction

In the multi-material analysis of both fluid flow and solid motion, there are different numerical approaches that include Eulerian, Lagrangian, and combined Lagrangian-Eulerian methods. Previously researched fluid-structure interaction analysis has mostly simulated an interaction between a structure and non-reactive flow, which does not consider the chemical reaction in flow. In the interaction analysis of large deformation of a structure due to high temperature and pressure flow accompanied by chemical reactions such as explosion or combustion, it is difficult to apply the geometry of the deformed structure to the fluid flow domain. In this reason, many studies have not been conducted to simultaneously analyze the interaction between the reactive flow and the structure deformation. The Eulerian method is used in the calculation of fluid flow [1] while the Lagrangian method is employed to simulate solid dynamics [2]. To utilize the advantages of both methods, a combined Lagrangian-Eulerian method [3-10] has been in use for the integrated analysis of complex interactions between fluids and solids.

Using the combined method as an interface treatment methodology, the remeshing technique [10] of arbitrary Lagrangian-Eulerian (ALE) and the particle level set method using the ghost fluid concept [3, 5, 11] are proposed. The remeshing composes a new mesh in the Eulerian domain, based on a Lagrangian domain boundary surface when a solid structure is changed. Since the method fundamentally operates in an unstructured grid, the numerical

accuracy is secured by increasing the number of grid cells in a high gradient domain. However, in the case of a large deformation problem, the method is barely suitable for calculation due to the accumulated numerical errors and high computational costs associated with determining the values in the newly generated grids. On the other hand, the particle level set method with a ghost node concept can efficiently discriminate the interface between Eulerian and Lagrangian domains in transient FSI problems. This is quite evident in various studies that utilize the combined Lagrangian-Eulerian methods [3-6]. In this study, a three-dimensional simulation techniques were developed for analyze the reactive flow including the chemical reaction with the large deformation of structure. The numerical code is verified by comparing the simulation results with the experimental values.

In this study, various reactive flows were considered. The ethylene-air mixture and the kerosene-air mixture, which are gaseous high energy materials, simulate the combustion reaction through the 1-step Arrhenius equation [12]. In addition, combustion characteristics of anisotropic PETN and HMX, which are solid energetic materials, were analyzed by using the modified anisotropic I&G model [13]. The developed combustion model compared the C-J condition and the detonation cell size. Structure deformation was performed by using Eulerian or Lagrangian analysis method and the method was verified by comparing with the experimental data of Taylor impact problem. A level set technique and a ghost fluid method (GFM) [14] were used to set boundary values and trace the interface between the reactive flow and the structure. In order to verify the multi-material analysis

method, the cantilever motion in the flow field and the tube deformation problem due to detonation load were simulated. The numerical results are verified by comparing with the theoretical and experimental values. For the three dimensional simulation, the STL file to level converting algorithm was developed. Moreover, the adaptive mesh refinement (AMR) [15] and message passing interface (MPI) for parallel processing were conducted to reduce the computation time and resources.

The interactions between reactive flow and structure under various thermal hydrodynamic loading systems were analyzed by the developed code. The behavior of rear cover which is deformed by the launching rocket plume inside a vertical launching system (VLS) is analyzed. This analysis results were verified by comparing with the experimental data, and the influence of rear cover deformation on the flow was confirmed through the analysis results. In addition, the explosion of the solid explosives in the three-dimensional concrete building, which cannot be simplified in two dimensions, and the pressure transmitted to the wall are analyzed. The numerical analysis results were compared with experimental data. In the analysis of tube deformation due to detonation inside the metal tube was simulated. The yield stress of metal tube is dependent on wall temperature and thermal softening was considered. In case of pulse detonation engine (PDE), which is exposed to high temperature environment, accurate results can be obtained by using temperature dependent properties and simulation results verified by comparison with theoretical failure model. The elastically vibrating tube was considered for detonation inside the PDE simulation. Due to the repetitively

detonation propagation inside PDE, the PDE wall is vibrated with its natural frequency even if the PDE does not be destroyed. The simulation results confirms that propagation of detonation is affected by the deformation of tube.

Chapter 2. Numerical Method

2.1 Governing equations and constitutive relations

2.1.1 Two-dimensional Eulerian coordinate system

For a full dynamic simulation of reactive flow and deformation of structure, governing equations of two-dimensional cylindrical (α = 1) and rectangular coordinate (α = 0) system are as follows:

$$\frac{\partial \rho}{\partial t}+\frac{\partial(\rho u_r)}{\partial r}+\frac{\partial(\rho u_z)}{\partial z}+\alpha\left(\frac{\rho u_r}{r}\right)=0 \tag{2.1}$$

$$\frac{\partial(\rho u_r)}{\partial t}+\frac{\partial\left(\rho u_r^{\,2}+P\right)}{\partial r}+\frac{\partial(\rho u_r u_z)}{\partial z}+\alpha\left(\frac{\rho u_r^2}{r}\right)-\delta\left(\alpha\frac{\tau_{rr}}{r}+\frac{\partial \tau_{rr}}{\partial r}+\frac{\partial \tau_{rz}}{\partial z}\right)=0 \tag{2.2}$$

$$\frac{\partial(\rho u_z)}{\partial t}+\frac{\partial(\rho u_r u_z)}{\partial r}+\frac{\partial\left(\rho u_z^{\,2}+P\right)}{\partial z}+\alpha\left(\frac{\rho u_r u_z}{r}\right)-\delta\left(\alpha\frac{\tau_{zr}}{r}+\frac{\partial \tau_{rz}}{\partial r}+\frac{\partial \tau_{zz}}{\partial z}\right)=0 \tag{2.3}$$

$$\begin{aligned}&\frac{\partial(\rho e)}{\partial t}+\frac{\partial\left[u_r(\rho e+P)\right]}{\partial r}+\frac{\partial\left[u_z(\rho e+P)\right]}{\partial z}-\alpha\left(\frac{u_r(\rho e+p)}{r}\right)\\&-k\frac{\partial^2 T}{\partial z^2}-k\frac{\partial^2 T}{\partial r^2}-\varphi\rho Q_i\dot{\omega}_i+\delta T\left(\alpha(3\lambda+2G)(\dot{\varepsilon}_{rr}+\dot{\varepsilon}_{zz})+\frac{\rho c}{T}\dot{T}\right)\\&\quad-\delta\left(\alpha\left(\frac{u_r\tau_{rr}+u_z\tau_{rz}}{r}\right)+\frac{\partial\left(u_r\tau_{zr}+u_z\tau_{zz}\right)}{\partial z}+\frac{\partial\left(u_r\tau_{rr}+u_z\tau_{rz}\right)}{\partial r}\right)=0\end{aligned} \tag{2.4}$$

$$\varphi\left\{\frac{\partial(\rho Y_i)}{\partial t}+\frac{\partial(\rho Y_i u_r)}{\partial r}+\frac{\partial(\rho Y_i u_z)}{\partial z}-\rho\dot{\omega}\right\}=0 \tag{2.5}$$

where parameters φ = 1 (and δ = 0) for the reactive flow or φ = 0 (and δ =1) for the structure. In the above equations ρ, u_r, u_z, P, τ_{ij}, e, Q_i, $\dot{\omega}$, T, k, α, λ, G, $\dot{\varepsilon}_{ij}$, and Y_i are density, r-axis velocity, z-axis velocity, pressure, deviatoric stress, total energy density, chemical energy released, chemical reaction rate,

temperature, conduction coefficient, thermal expansion coefficient, Lame's first parameter, shear modulus, strain rate, and mass fraction of the reactant mixture, respectively. In this model, the chemical reaction rate of the detonation is calculated by using the Arrhenius rate equation [16].

Inside the structure being an elasto-plastic medium, the deviatoric stresses are calculated in addition to the evolution equations, while the strain rate and Cauchy stress tensor are obtained by solving Eqs. (2.6)-(2.9).

$$\frac{\partial \tau_{rr}}{\partial t}+\frac{\partial\left(\tau_{rr}u_r\right)}{\partial r}+\frac{\partial\left(\tau_{rr}u_z\right)}{\partial z}=2\tau_{rz}\Omega_{rz}+\tau_{rr}\left(\frac{\partial u_r}{\partial r}+\frac{\partial u_z}{\partial z}\right)+2G\left(\frac{\partial u_r}{\partial r}-\sum-\eta D_{rr}^{p}\right) \tag{2.6}$$

$$\frac{\partial \tau_{zz}}{\partial t}+\frac{\partial\left(\tau_{zz}u_r\right)}{\partial r}+\frac{\partial\left(\tau_{zz}u_z\right)}{\partial z}=-2\tau_{rz}\Omega_{rz}+\tau_{zz}\left(\frac{\partial u_r}{\partial r}+\frac{\partial u_z}{\partial z}\right)+2G\left(\frac{\partial u_z}{\partial z}-\sum-\eta D_{zz}^{p}\right) \tag{2.7}$$

$$\frac{\partial \tau_{rz}}{\partial t}+\frac{\partial\left(\tau_{rz}u_r\right)}{\partial r}+\frac{\partial\left(\tau_{rz}u_z\right)}{\partial z}=\Omega_{rz}\left(\tau_{zz}-\tau_{rr}\right)+\tau_{rz}\left(\frac{\partial u_r}{\partial r}+\frac{\partial u_z}{\partial z}\right)+2G\left(\frac{1}{2}\left(\frac{\partial u_r}{\partial z}+\frac{\partial u_z}{\partial r}\right)-\eta D_{rr}^{p}\right) \tag{2.8}$$

$$\dot{\varepsilon}_{ij}=\frac{1}{2}\left(\frac{\partial u_i}{\partial x_j}+\frac{\partial u_j}{\partial x_i}\right) \tag{2.9}$$

In the case of $\bar{\sigma}>\sigma_Y$ after the time has evolved, the components of deviatoric stresses are located in an unphysical state. The allowable stresses must be back to the yield surface which will satisfy the physical constraint using the radial return algorithm stated in Eq. (2.10).

$$\begin{aligned}&\xi=\int_t^{t+\Delta t}\Lambda dt=\frac{\bar{\sigma}-\sigma_Y}{\sqrt{6}G\left(1+\frac{h}{3G}\right)}\rightarrow\Lambda=\frac{d\xi}{dt}\\&\Rightarrow D_{ij}^{P}=\Lambda N_{ij}=\Lambda\frac{S_{ij}}{\sqrt{S_{kl}S_{kl}}}=\frac{d}{dt}\left(\frac{\bar{\sigma}-\sigma_Y}{\sqrt{6}G\left(1+\frac{h}{3G}\right)}\right)\frac{S_{ij}}{\sqrt{S_{kl}S_{kl}}}\end{aligned} \tag{2.10}$$

Here, Ω_{ij}, Σ, D_{ij}^{P}, Λ, N_{ij}, ξ, $\bar{\sigma}$, σ_Y, h and δ_{ij} are spin tensor, volume strain rate, plastic strain rate tensor, positive (consistency) parameter, unit outward

normal to the yield surface, return algorithm variable, effective stress, current yield stress, hardening coefficient, and Kronecker delta, respectively. η equals to 0 (or 1) in the elastic (or plastic) state. Similar discussions on the parameters can be found in Ref. [17].

The governing equations are solved by a third-order RK (Runge-Kutta) and the ENO (essentially non-oscillatory) method in temporal and spatial discretizations, respectively. As for the sructure, the Mie-Gruneisen equation of state Eq. (2.11), and the rate-dependent Johnson-Cook strength model, Eq. (2.12) are used:

$$p(\rho,e)=\rho_0\Gamma_0 e+\begin{cases}\dfrac{\rho_0 c_0^2\varphi}{(1-s\varphi)^2}\left[1-\dfrac{\Gamma_0}{2}\varphi\right] & \text{if } \rho\geq\rho_0\\ c_0^2\left(\rho-\rho_0\right) & \text{otherwise}\end{cases} \tag{2.11}$$

$$\sigma_Y=\left(\sigma_{Y,0}+A\left(\bar{\varepsilon}^P\right)^n\right)\left(1+B\ln\left(\frac{\dot{\bar{\varepsilon}}^P}{\dot{\varepsilon}_0}\right)\right)\left(1-\left(\frac{T-T_0}{T_m-T_0}\right)^m\right) \tag{2.12}$$

where Γ_0, s, c_0, A, B, n and m are material constants, and ρ_0, T_m, T_0, and are initial density, melting temperature, ambient temperature, and effective plastic strain rate, respectively..

2.1.2 Three-dimensional Eulerian coordinate system

For the three-dimensional reactive flow analysis, the governing equations of three-dimensional rectangular coordinate system were as follows:

$$\frac{\partial\rho}{\partial t}+\frac{\partial\rho u}{\partial x}+\frac{\partial\rho v}{\partial y}+\frac{\partial\rho w}{\partial z}=0 \tag{2.13}$$

$$\frac{\partial \rho u}{\partial t}+\frac{\partial(\rho u^2+p)}{\partial x}+\frac{\partial \rho uv}{\partial y}+\frac{\partial \rho uw}{\partial z}-\delta\left(\frac{\partial S_{xx}}{\partial x}+\frac{\partial S_{xy}}{\partial y}+\frac{\partial S_{xz}}{\partial z}\right)=0 \tag{2.14}$$

$$\frac{\partial \rho v}{\partial t}+\frac{\partial \rho vu}{\partial x}+\frac{\partial(\rho v^2+p)}{\partial y}+\frac{\partial \rho vw}{\partial z}-\delta\left(\frac{\partial S_{yx}}{\partial x}+\frac{\partial S_{yy}}{\partial y}+\frac{\partial S_{yz}}{\partial z}\right)=0 \tag{2.15}$$

$$\frac{\partial \rho w}{\partial t}+\frac{\partial \rho wu}{\partial x}+\frac{\partial \rho wv}{\partial y}+\frac{\partial(\rho w^2+p)}{\partial z}-\delta\left(\frac{\partial S_{zx}}{\partial x}+\frac{\partial S_{zy}}{\partial y}+\frac{\partial S_{zz}}{\partial z}\right)=0 \tag{2.16}$$

$$\begin{aligned}&\frac{\partial \rho E}{\partial t}+\frac{\partial u(\rho E+p)}{\partial x}+\frac{\partial v(\rho E+p)}{\partial y}+\frac{\partial w(\rho E+p)}{\partial z}-k\frac{\partial^2 T}{\partial x^2}-k\frac{\partial^2 T}{\partial y^2}-k\frac{\partial^2 T}{\partial z^2}\\&\qquad-\varphi\rho Q_i\dot{\omega}_i+\delta T\left(\alpha(3\lambda+2G)\left(\dot{\varepsilon}_{xx}+\dot{\varepsilon}_{yy}+\dot{\varepsilon}_{zz}\right)+\frac{\rho c}{T}\dot{T}\right)-\delta S_E=0\end{aligned} \tag{2.17}$$

$$\varphi\left(\frac{\partial Y_i}{\partial t}+\frac{\partial Y_i u}{\partial x}+\frac{\partial Y_i v}{\partial y}+\frac{\partial Y_i w}{\partial z}-\dot{\omega}\right)=0 \tag{2.18}$$

$$\begin{aligned}S_E=&\frac{\partial\left(uS_{xx}+vS_{xy}+wS_{xz}\right)}{\partial x}+\frac{\partial\left(uS_{xy}+vS_{yy}+wS_{yz}\right)}{\partial y}\\&+\frac{\partial\left(uS_{xz}+vS_{yz}+wS_{zz}\right)}{\partial z}\end{aligned} \tag{2.19}$$

where, parameters $\varphi = 1$ (and $\delta = 0$) for the reactive flow or $\varphi = 0$ (and $\delta = 1$) for the structure. In the above equations, ρ, u, v, w, E, p, $Q_i, \dot{\omega}$, T, k, α, λ, G, $\dot{\varepsilon}_{ij}$, Y_i and S_{ij} are density, velocity components in the x-, y-, z-directions, energy per unit mass, hydrostatic pressure, chemical energy released, chemical reaction rate, temperature, conduction coefficient, thermal expansion coefficient, Lame's first parameter, shear modulus, strain rate, mass fraction of the reactant mixture, deviatoric stress, respectively.

Inside the structure being an elasto-plastic medium, the deviatoric stresses are calculated in addition to the evolution equations[18] as follows:

$$\frac{\partial S_{xx}}{\partial t}+\frac{\partial\left(uS_{xx}\right)}{\partial x}+\frac{\partial\left(vS_{xx}\right)}{\partial y}+\frac{\partial\left(wS_{xx}\right)}{\partial z}=2\Omega_{xy}S_{xy}+2\Omega_{xz}S_{xz}+2G\bar{D}_{xx} \tag{2.20}$$

$$\frac{\partial S_{xy}}{\partial t}+\frac{\partial\left(uS_{xy}\right)}{\partial x}+\frac{\partial\left(vS_{xy}\right)}{\partial y}+\frac{\partial\left(wS_{xy}\right)}{\partial z}=\Omega_{xy}\left(S_{yy}-S_{xx}\right)+\Omega_{xz}S_{zy}-\Omega_{zy}S_{xz}+2G\bar{D}_{xy} \tag{2.21}$$

$$\frac{\partial S_{yy}}{\partial t}+\frac{\partial\left(uS_{yy}\right)}{\partial x}+\frac{\partial\left(vS_{yy}\right)}{\partial y}+\frac{\partial\left(wS_{yy}\right)}{\partial z}=2\Omega_{xy}S_{xy}+2\Omega_{yz}S_{yz}+2G\bar{D}_{yy} \tag{2.22}$$

$$\frac{\partial S_{xz}}{\partial t}+\frac{\partial\left(uS_{xz}\right)}{\partial x}+\frac{\partial\left(vS_{xz}\right)}{\partial y}+\frac{\partial\left(wS_{xz}\right)}{\partial z}=\Omega_{xz}\left(S_{zz}-S_{xx}\right)+\Omega_{xy}S_{yz}-\Omega_{yz}S_{xy}+2G\bar{D}_{xz} \tag{2.23}$$

$$\frac{\partial S_{yz}}{\partial t}+\frac{\partial\left(uS_{yz}\right)}{\partial x}+\frac{\partial\left(vS_{yz}\right)}{\partial y}+\frac{\partial\left(wS_{yz}\right)}{\partial z}=\Omega_{yz}\left(S_{zz}-S_{yy}\right)+\Omega_{yx}S_{xz}-\Omega_{xz}S_{xy}+2G\bar{D}_{yz} \tag{2.24}$$

$$\frac{\partial S_{zz}}{\partial t}+\frac{\partial\left(uS_{zz}\right)}{\partial x}+\frac{\partial\left(vS_{zz}\right)}{\partial y}+\frac{\partial\left(wS_{zz}\right)}{\partial z}=2\Omega_{yz}S_{yz}+2\Omega_{xz}S_{xz}+2G\bar{D}_{zz} \tag{2.25}$$

$$\Omega_{ij}=\frac{1}{2}\left(\frac{\partial u_i}{\partial x_j}+\frac{\partial u_j}{\partial x_i}\right) \tag{2.26}$$

$$\bar{D}_{ij}=\frac{1}{2}\left(\frac{\partial u_i}{\partial x_j}+\frac{\partial u_j}{\partial x_i}\right)-\frac{1}{3}D_{kk}\delta_{ij} \tag{2.27}$$

Here, $S_{ij}, \Omega_{ij}, \bar{D}_{ij}$, and δ_{ij} are deviatoric stress, spin tensor, deviatoric strain rate tensor, and Kronecker delta, respectively. The governing equations are solved by a third-order RK (Runge-Kutta) and the ENO (essentially non-oscillatory) method in temporal and spatial discretizations, respectively. The gas pressure of the reactive fluid is calculated by the ideal equation of state, As for the structure, the Mie-Gruneisen equation of state and the rate-dependent Johnson-Cook strength model are used

2.1.3 Lagrangian coordinate system

For the simulate a realistic elastic motion of structure, a nine node quadrilateral element based on total Lagrangian formulation is used to capture the geometrically nonlinear behavior [19], and is further extended to

predict the materially nonlinear behavior. All element quantities in the total Lagrangian description are expressed with respect to the initial configuration. Using the deformation gradient, Green-Lagrange strain components are defined and the relevant stresses are then calculated by the constituting equation. The following relationship is applied for elastic analysis. For plastic analysis, the defining the strain components and the constituting matrix need to be modified.

$$S = C\left\{\varepsilon_{xx} \quad \varepsilon_{yy} \quad 2\varepsilon_{xy}\right\}^{\mathrm{T}} = \left\{\sigma_{xx} \quad \sigma_{yy} \quad \sigma_{xy}\right\}^{\mathrm{T}} \tag{2.28}$$

$$\frac{1}{2}\left(F^{\mathrm{T}}F - I\right) = \left\{\varepsilon_{xx} \quad \varepsilon_{yy} \quad \varepsilon_{xy}\right\}^{\mathrm{T}} \tag{2.29}$$

$$\bar{S} = \begin{bmatrix} \hat{S} & 0 \\ 0 & \hat{S} \end{bmatrix}, \quad \hat{S} = \begin{bmatrix} \sigma_{xx} & \sigma_{xy} \\ \sigma_{xy} & \sigma_{yy} \end{bmatrix} \tag{2.30}$$

where *S, C, ε, σ, F, I*, and $\bar{S}$ are stress vector, constituting matrix, strain, stress, deformation gradient, identity matrix, and second Piola-Krchhoff (PK) stresses, respectively.

Virtual work linearization can be expressed by taking the deformation gradients and the second Piola-Kirchhoff (PK) stresses into account.

$$\left(k_g + k_h\right)\Delta d = -f_i + f_{ext} \tag{2.31}$$

$$\left(\iint_{\Omega^0} B\bar{S}B^{\mathrm{T}}d\Omega^0 + \iint_{\Omega^0} B\bar{F}^{\mathrm{T}}C\bar{F}B^{\mathrm{T}}d\Omega^0\right)\Delta d = -\iint_{\Omega^0} B\bar{F}^{\mathrm{T}}Sd\Omega^0 + f_{ext} \tag{2.32}$$

where k_g, k_k, *d*, f_i, f_{ext}, *B, S, C,* $\bar{F}$, and Ω are geometric stiffness matrix, current stiffness matrix, displacement, internal force vector, external force

vector, strain displacement relation matrix, second PK stresses matrix, constitutive matrix, deformation gradient matrix, and current domain, respectively. f_{ext} is external load vector defined by pressure loading from fluid analysis.

$$f_{ext} = \int_{\Gamma^e} N^{\mathrm{T}} p d\Gamma^e, \quad p = \begin{Bmatrix} p_x & p_y & 0 \end{Bmatrix}^{\mathrm{T}} \tag{2.33}$$

where N, p, and Γ are elemental shape function, pressure, and surface of domain, respectively.

The plane stress projected plasticity model based on the incremental plastic flow prediction and a von Mises equation with isotropic hardening is used to calculate the rear cover material nonlinearity [20]. This approach is appropriate for elastoplasticity in a metallic structure that undergoes large displacement and small strain. Using this plastic model, the updated strain and stress components are employed in Eqs. (2.28-29).

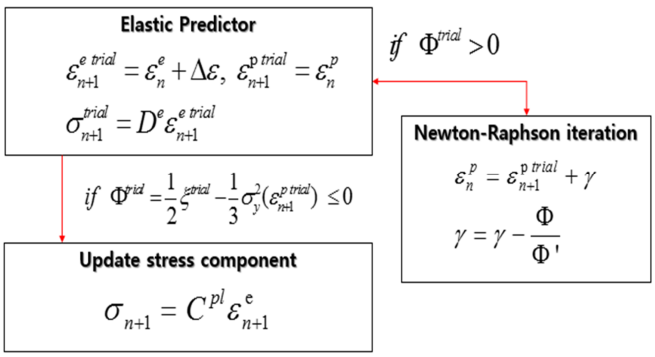

Fig. 2.1 Newton Raphson return mapping algorithm.

In Fig. 2.1, the defined elastic strain ($\underline{\varepsilon}$), the corresponding trial stress ($\underline{\varepsilon}^{e\ trial}$) and the accumulated plastic strain ($\underline{\varepsilon}^{p\ trial}$) are calculated to check for plastic admissibility. To comply with the von Mises model, a yield function equation (Φ) is used. By applying plastic multiplier (γ) in order to satisfy hardening slope, the elastoplastic tangent operator ($\underline{\underline{C}}^{ep}$) is iteratively defined by matrix $\underline{\underline{A}}$. The detailed mathematics and the relevant descriptions are described in Ref. [20]. For time transient analysis, the Hilbert Hughes Taylor (HHT)-α method is used. The final form of the governing equation for the flexible structure is:

$$(1+\alpha)(f_{ext}^{n+1} - f_i^{n+1}) - \underline{\underline{M}}\ddot{q}_G^{n+1} + \alpha(f_i^n - f_{ext}^n) = 0 \tag{2.34}$$

where, the inertial matrix $\underline{\underline{M}}$ is defined using the elemental shape function, $\underline{\underline{M}} = \rho\int_\Omega \underline{\underline{N}}^{\mathrm{T}}\underline{\underline{N}}d\Omega$. f_i is the internal load vector defined by the right side of Eq. (2.31). The contact analysis is based on the global Lagrange multiplier. This approach is realized by multiplying the gap condition. Gap condition is defined by the position of slave and master bodies.

2.2 Interface tracking and treatment method

To track the interface and define the boundary value between the hot rocket plume and the rear cover, a level-set method based on ghost fluid method (GFM) is applied [21]. The level (ϕ) defines a distance of each material

surface from the contact interface. So the zero level (ϕ = 0) represents the interface of the two materials and the signs of level classify the material, meaning the region with ϕ < 0 indicates the inner side of the target material that is either fluid or solid. At the interface, the boundary conditions are determined by the GFM. The properties of ghost nodes are addressed by the values of symmetric real nodes which are determined by extrapolation. At the ghost nodes, normal to the interface is calculated by Eq. (2.35)

$$n = \frac{\nabla \phi}{|\nabla \phi|} \tag{2.35}$$

The following sections describe the level conversion methods and GFM in detail.

2.2.1 Level conversion method

For the complex geometry of three-dimensional shape, level conversion method was developed. A STL file, which is the most common three-dimensional shape file format, was converted as level in Eulerian domain. The STL file stores geometry information as a combination of triangles, and the data of the triangle is the vertex positions and the vertical vector. As shown in Fig. 2.2. (a), the distance to the boundary (triangle) of the grid point inside the triangle is calculated by Eq. (2.36).

$$D = \frac{aX[i] + bY[j] + cZ[k] - aP_{x1} - bP_{y1} - cP_{z1}}{\sqrt{a^2 + b^2 + c^2}} \tag{2.36}$$

Where a, b, c, $X[i]$, $Y[j]$, $Z[k]$, P_{x1}, P_{y1}, P_{z1}, and D are x-, y-, z-axis component of vector, x, y, z-axis location of grid, x, y, z-axis location of triangle point

and distance, respectively. By this equation, a positive distance value is calculated on the upper side which is the same direction as the vertical vector, and a negative distance value is calculated on the lower side opposite to the vertical vector. However, for a the grid point located outside of the triangle as shown in Fig. 2.2. (b), the distance could not be calculated by Eq. (2.36). Therefore, the minimum distance between the line of the triangle and the grid point is defined as the level value, and the sign of the level is obtained through the normal vector. The sign of distance is determined the material and the signed distance could be considered as level in Eulerian domain.

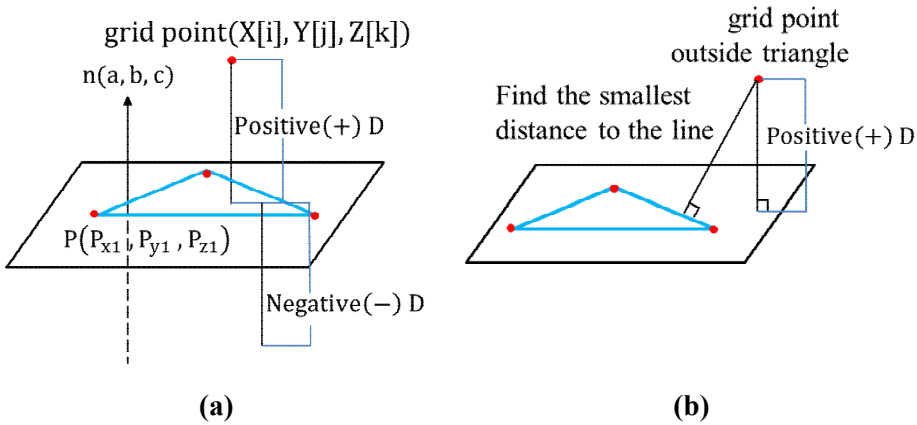

Fig. 2.2. Schematic diagram of triangles in STL file with grid point located (a) inside and (b) outside of the triangles.

The minimum distance from the line defined as follows. Although fine grids are necessary for handling the complex supersonic flow of reactive flow, the structure deformation can be simulated with a relatively coarse mesh. If the distance between the Lagrangian nodes or the line length of triangles in STL file is larger than the Eulerian mesh size, the level is represented as Fig.

2.4 (a). The interface (ϕ = 0, blue) does not appear as a line and a normal vector to the boundary at each Eulerian node is not defined. So one discretizes the lines as white dots. The white dots are artificial nodes that define the intended geometry in terms of Eulerian quantity. The distance between the white dots is one half of the Eulerian mesh size, and the level is converted as in Fig. 2.4 (b). The interface and normal vectors are clearly defined and thus the ghost node values can be determined.

To set different sign for each material, the normal vector and the Jordan curve theorem [22] is applied. In Fig. 2.3 (a), the sign of the interior level is negative when the number of point is odd, where the straight line starting from an inner point intersects the boundary. In the opposite case, the level sign is positive. Using this approach in the Eulerian domain, the Lagrangian geometry described by signed level is shown as in Fig. 2.3 (b).

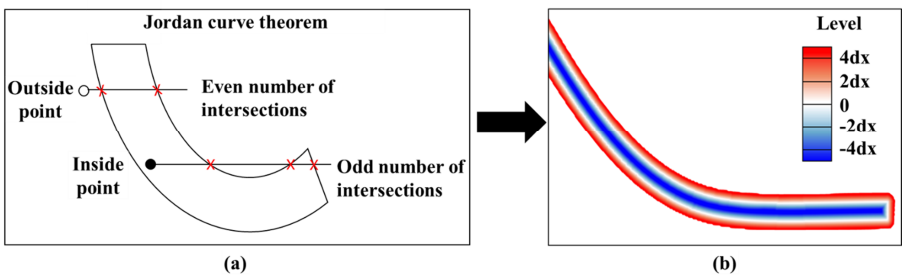

Fig. 2.3. Conceptual diagram of Jordan curve theorem and (b) Lagrangian geometry described by signed level ($\phi < 0$: inside (solid, blue), $\phi > 0$: outside (fluid, red) $\phi = 0$: interface (white line)) in Eulerian domain.

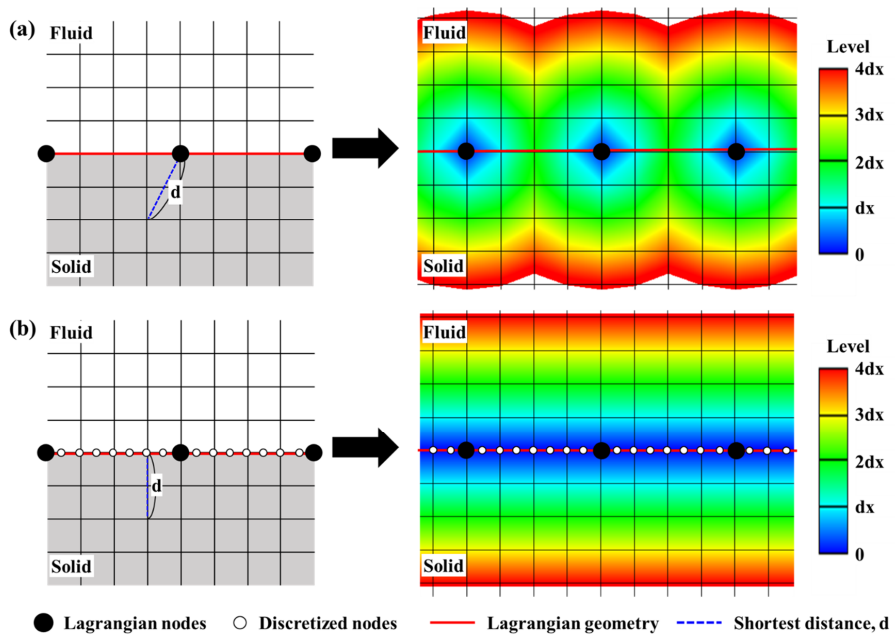

Fig. 2.4. Lagrangian geometry (red line) represented as an unsigned level in Eulerian domain: (a) original and (b) discretized Lagrangian nodes.

2.2.3 Ghost fluid method

At the interface of material, boundary conditions need to be determined because of the discontinuous entropy distribution. A GFM is used to address the multi-material problem. In this method, ghost nodes are distributed on outside of the target material of interest using an extrapolation on the basis of the continuous entropy assumption. Here, the real discontinuity in the entropy merged with the ghost nodes generates the proper boundary conditions. Then the same pressure and velocity are imposed in the ghost nodes. The entropies in the ghost nodes are obtained from the real material. Then the remaining

variables are determined from the entropy relation and the equation of state. More in-depth descriptions of variables are explained in Refs. [21, 23]. At the three-dimensional interface, there are normal vector and two tangential vectors are needed for defining the ghost values at ghost node. Figure 2.5. shows the normal and tangential vectors in three-dimensional Eulerian domain and details of defining ghost value method is described in Ref. [18].

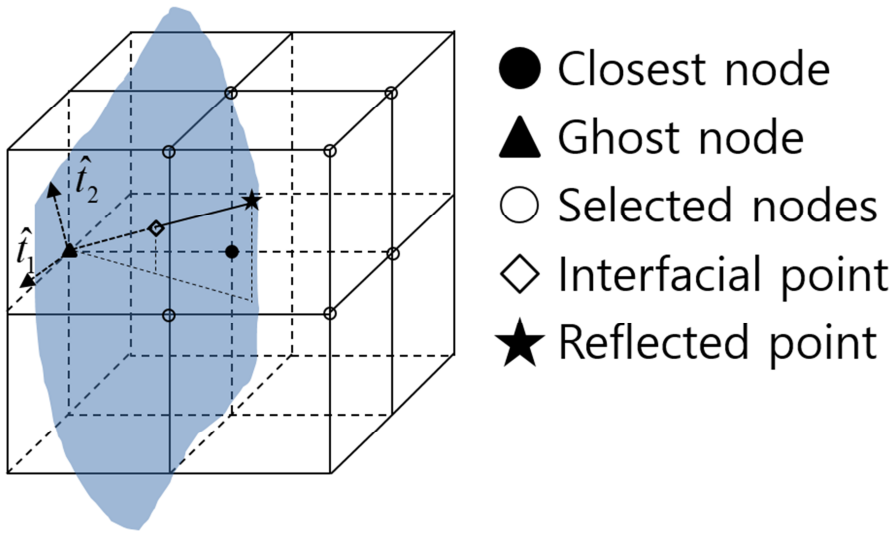

Fig. 2.5. Defining ghost node in three-dimensional Eulerian domain

At the reflected point, the interpolated variables (density, velocity, energy, pressure, deviatoric stresses, species) are transformed to normal and tangential components in ghost nodes. For the velocity components at the reflected point calculated as follows:

$$\left[u_n \quad u_{t_1} \quad u_{t_2}\right] = \left[\left|\vec{u}_n\right| \quad \left|\vec{u}_{t_1}\right| \quad \left|\vec{u}_{t_2}\right|\right] = \left[\vec{u}\cdot\hat{n} \quad \vec{u}\cdot\hat{t}_1 \quad \vec{u}\cdot\hat{t}_2\right] \tag{2.37}$$

where, $\vec{u}$, $\vec{u}_n$, $\vec{u}_{t_1}$, $\vec{u}_{t_2}$, $\hat{n}$, $\hat{t}_1$, and $\hat{t}_2$ are velocity vector, normal, tangential

velocity vectors, normal, and tangential vector at reflected node.

A first invariant of the stress tensor, J_1, at the interface must be zero. Thus the deviatoric stress S_{zz} set as follows.

$$J_1 = S_{xx} + S_{yy} + S_{zz} = 0, \quad S_{zz} = -(S_{xx} - S_{yy}) \tag{2.38}$$

The S_{zz} calculated by Eq. (2.38) in the real fluid, and the stress at ghost node is calculated as follows:

$$\left[\sigma_{nn}^{G} \quad \sigma_{t_1t_1}^{G} \quad \sigma_{t_2t_2}^{G}\right] = \left[\left(\sigma_{nn}^{D}\right)_P \quad \left(\sigma_{t_1t_1}^{N}\right)_P + \Delta\sigma \quad \left(\sigma_{t_2t_2}^{N}\right)_P + \Delta\sigma\right] \tag{2.39}$$

$$2\Delta\sigma = \left(\sigma_{nn}^{D} + \sigma_{t_1t_1}^{N} + \sigma_{t_2t_2}^{N}\right)_P \tag{2.40}$$

Before the correction, $J_1 \neq 0$ in the Taylor impact problems as shown in Fig. 2.6. (a), Using the correction method for total stress tensor at the ghost node *P*, $J_1 = 0$ as shown in Fig. 2.6. (b).

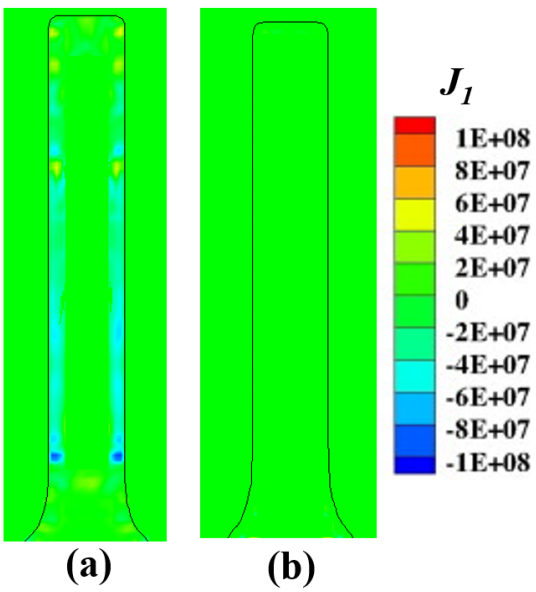

Fig. 2.6. Comparison between J_1 (a) uncorrected stress, (b)corrected stress

2.2.4 Fluid-solid interaction algorithm

In order to unify a hydrodynamic Eulerian solver for plume and a Lagrangian solver for non-linear rear cover, the outline of the developed algorithm is as follows in Fig. 2.7.

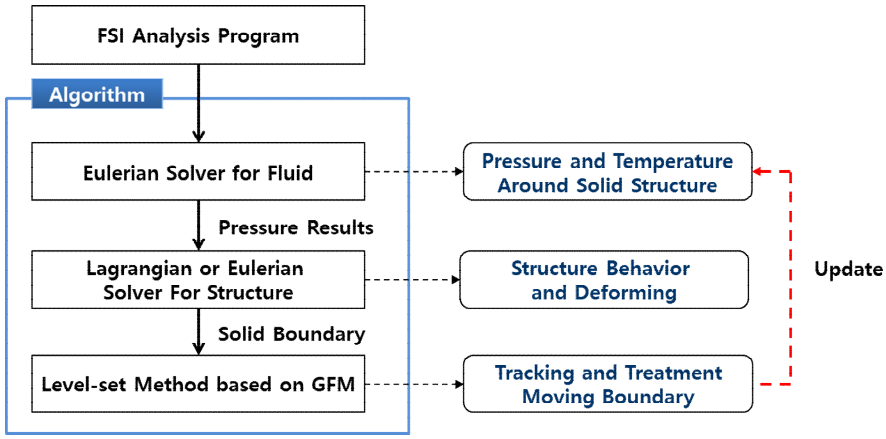

Fig. 2.7. Fluid structure interaction method algorithm.

Initially, the reactive fluid flow and solid dynamics are described in the Eulerian configuration. The outer boundary of the structure is represented by the level sets and the boundary conditions are determined by the values of ghost nodes. Then the fluid flow is solved by the Eulerian solver. The ghost node values are obtained by the real material while normal and tangential velocities are calculated. The calculated total pressure near the structure is used as the boundary value update for the external force for a structure solver. The solver calculates the deformed geometry and converts it into a level in the next time step. The reactive fluid flow and structure are strongly coupled in this sense, and the pressure and geometry data are exchanged at every time step to minimize the numerical errors in the unified simulation.

2.3 Advanced numerical technics for 3D simulation

In addition, to ensure the efficiency of the 3D computation, AMR was developed based on previous studies [24-26] Cell-based AMR was implemented to concentrate the computational resources in the required regions. Generated from a coarse uniform structured computational grid, the refined grid forms a system of meshes with various sizes similar to an unstructured grid. Mesh division proceeds prior to the flux calculation and time integration. A numerical error indicator is calculated for all the existing cells to determine which region requires a finer mesh to accurately capture the physical phenomena. A refined cell should be removed if it is no longer required.

For the boundary condition treatment, ghost cells are implemented. These cells are generated just outside of the computational domain, following the division level of the adjacent cells. Because a third-order spatial discretization requires three cells in its stencil, three ghost cells are generated for each outermost cell.

The developed AMR works were confirmed well using four validation problems: 2D shock diffraction, 2D Riemann problems, and a simple 3D shock tube. First, numerical simulations of shock diffraction were performed under the same experimental setup[27] with the intensity of the shock wave being the Mach number, 1.3. The simulation result using a shadowgraph image is shown in Fig. 2.8. (b), which is compared to an experimental shadowgraph image in Fig. 2.8. (a). In both Fig. 2.8. (a) and Fig. 2.8. (b), the

normal shock, bow shock, and expansion pan induced by the shock diffraction are identical and it can be confirmed that their positions are nearly the same.

(a) **(b)**

Fig. 2.8. Comparison between (a) an experimental shadowgraph image18 and (b) the numerical shadowgraph image of our AMR result for the shock diffraction problem.

Next, the 2D Riemann problem was considered. This problem is an extension of the Sod shock tube problem, which assigns initial conditions to four separated regions. Mesh refinement was performed for up to four divisions. The result of the simulation was compared to a previous numerical study[19]. In the simulation, working fluid is ideal gas with $\gamma = 1.4$ and density, velocity, and pressure normalized. The initial conditions are listed in Table 2.1 In this table, parts 1, 2, 3, and 4 refer to the upper left, upper right, lower left, and lower right areas, respectively, where the entire domain is divided

into four regions. The variables are non-dimensional. Figure 2.9 shows a comparison between the reference result and our numerical result for each case. The AMR results are very similar to those of the reference at each illustrated time step.

Table 2.1. Initial conditions for the 2D Riemann problem.

	Part 1	Part 2	Part 3	Part 4
Case 1				
Pressure	0.35	1.1	1.1	0.35
Density	0.5065	1.1	1.1	0.5065
x-axis velocity	0.8939	0	0.8939	0
y-axis velocity	0	0	0.8939	0.8939
Case 2				
Pressure	1	0.4	1	1
Density	1	0.5313	0.8	1
x-axis velocity	0.7276	0	0	0
y-axis velocity	0	0	0	0.7276
Case 3				
Pressure	1	1	0.4	0.4
Density	2	1	1.0625	0.5197
x-axis velocity	0	0	0	0
y-axis velocity	−0.3	−0.4	0.2145	−1.1259

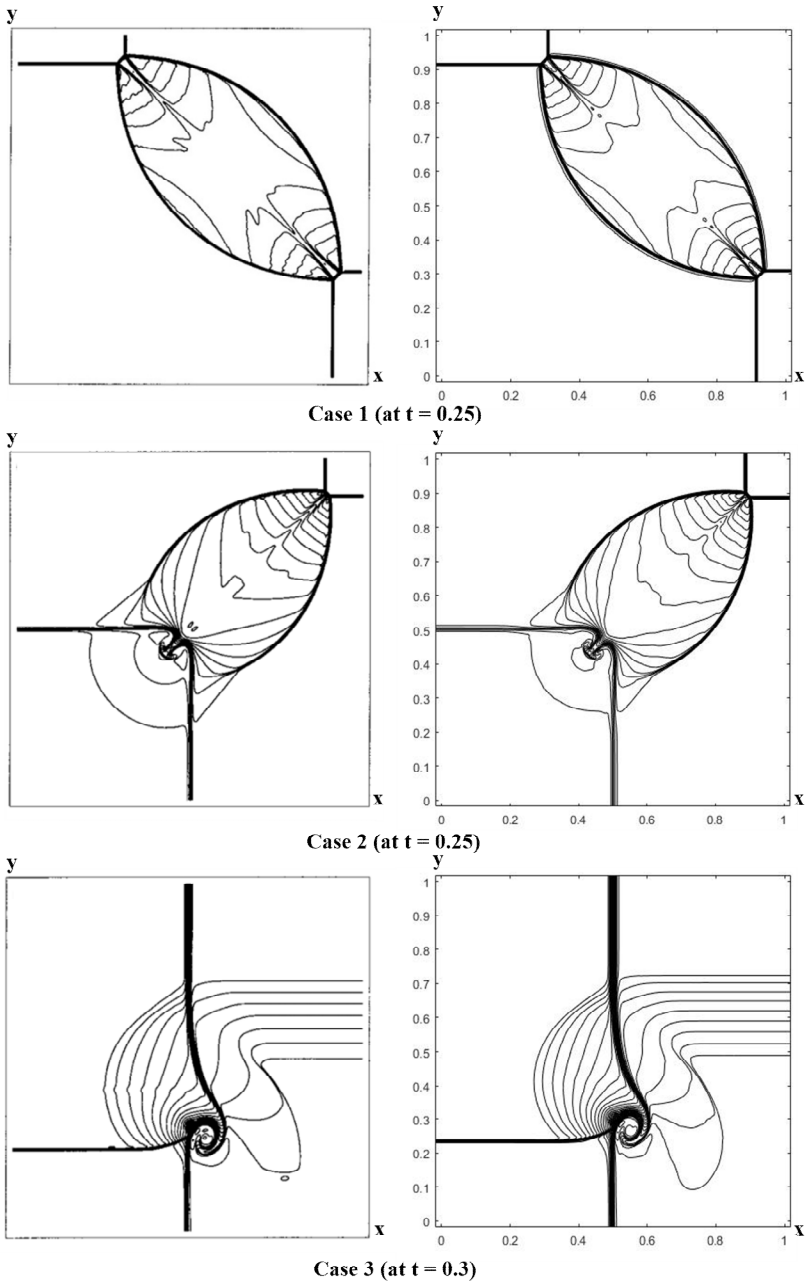

Fig. 2.9. Comparison between the density contour results of a previous study19 (left) and our AMR result (right) for the 2D Riemann problem.

Finally, a simple non-reactive shock tube problem with an ideal gas EOS was considered in three-dimensions. The calculation size is 0.4 m × 0.4 m × 1 m, and it is initially separated into two regions: left (ρ_L = 0.125, P_L = 0.1) and right (ρ_R = 1.0, P_R = 1.0). Figures 2.10. (a) and 2.10. (b) show the computational mesh and the density contour at 0.2 s. In these figures, the shock front, contact surface, and expansion pan are well tracked by the mesh refinement. In addition, the density profile on the z-axis line reproduces the exact solution and calculation result of the uniform mesh, as shown in in Fig. 2.10. (c). When using AMR (max level = 3), the computation time can be shortened by approximately five times even though the result is same as that for the uniform mesh result. Therefore, the AMR technique was used in the 3D anisotropic ignition model to save computation time while securing the resolution near the discontinuities.

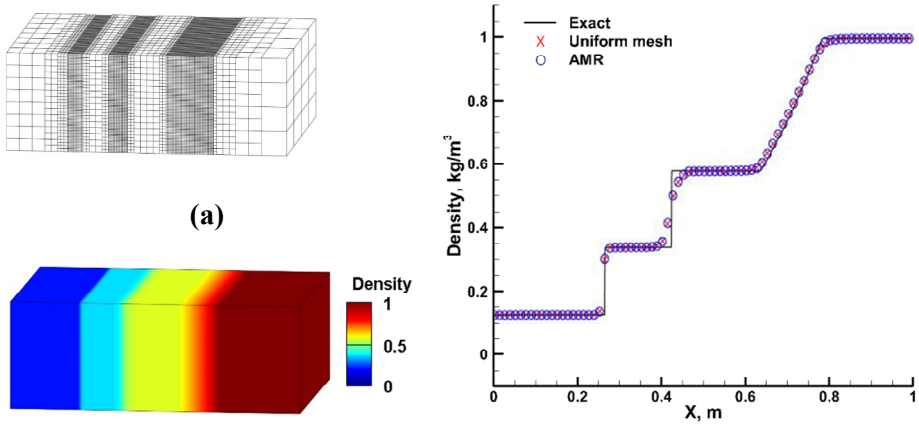

(a) **(b)** **(c)**

Fig. 2.10. (a) Computational mesh, (b) density contour, and (c) density profiles for the exact and the simulation results on the z-axis line at 0.2 s.

Chapter 3. Validation

3.1 Gaseous energetic materials

3.1.1 Kerosene-air mixture

To assure numerical accuracy during simulation of the kerosesne-air detonation, the mesh refinement must be conducted based on the parameters of Table 3.1. Figure 3.1. shows pressure profiles of three different mesh sizes 1/15, 1/50, and 1/100 mm for addressing the reaction zone refinement requirement. Both von Neumann spike and CJ presure based on 1/50 and 1/100 mm resolutions are similar, and thus 1/50 (0.02) mm is chosen for all detonation calculations of this paper.

Table 3.1. Initial conditions and material properties of a kerosene-air mixture

Parameter	Kerosene-air mixture	C_2H_4-air mixture
Initial density, ρ_0	1.236 kg/m^3	1.58 kg/m^3
Initial pressure, P_0	1.01x10^5 Pa	1.33x10^5 Pa
Initial temperature, T_0	433 K	293 K
Specific heat ratio, γ	1.33	1.15
Molecular weight, M_W	0.03036 kg/mol	29x10^{-3} kg/mol
Pre-exponential factor, A	8.0x10^8 m^3/(kg-s)	3.2x10^8 m^3/(kg·s)
Activation energy, E_a	71036 J/mol	35.351RT_0 J/mol
Chemical heat release, Q	1.9x10^6 J/kg	48.824RT_0/M_w J/kg
CJ detonation pressure	18 P_0	*12 P_0*
CJ detonation velocity	1780 m/s	1870 m/s

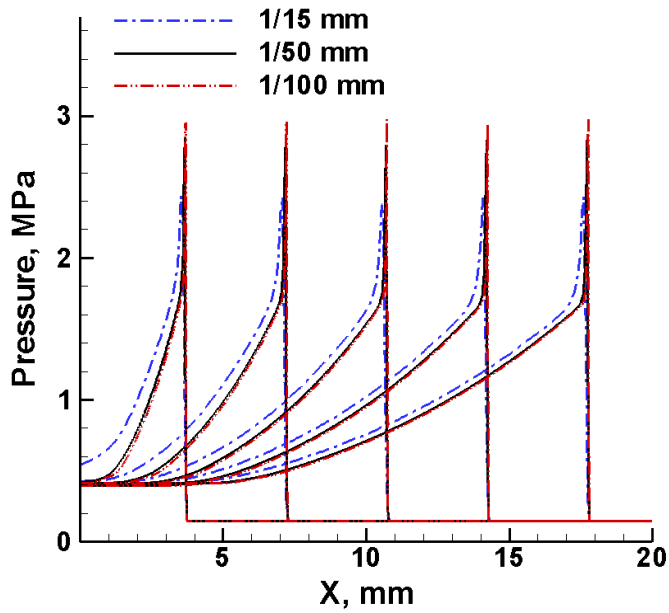

Fig. 3.1. Mesh resolution test for kerosene-air mixture detonation (1/15, 1/50, and 1/100 mm)

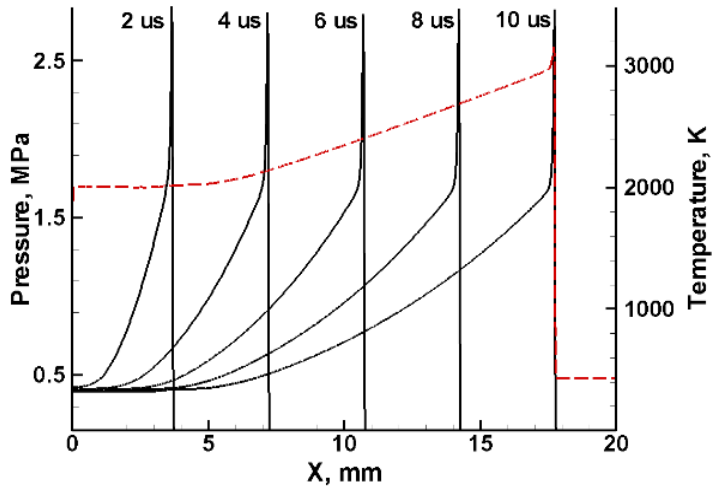

Fig. 3.2. Pressure history in solid line and temperature in dashed shown at 10 μs

Figure 3.2 shows the pressure history together with temperature of the propagating detonation wave. The CJ pressure (1.8 MPa) and velocity (1750 m/s) are in agreement with the reference values[28, 29].

Following the Arrhenius rate law of detonation, two-dimensional cell structure of the kerosene-air mixture is sought. The domain is a tube of inner radius r_i = 200 mm as depicted in Fig. 3.3. The boundary conditions on top, bottom, right, and left are symmetric, wall, zero gradient, and extrapolated ($X_{boundary}$ = $0.95X_1$+$0.05X_0$), respectively. Initially the CJ values are used to provide onset of detonation on the left. The numerically attained cell size of the kerosene-air mixture is validated against the experiment data[30]. Three different initial mixture pressures of 1, 1.5, and 2 bars are considered.

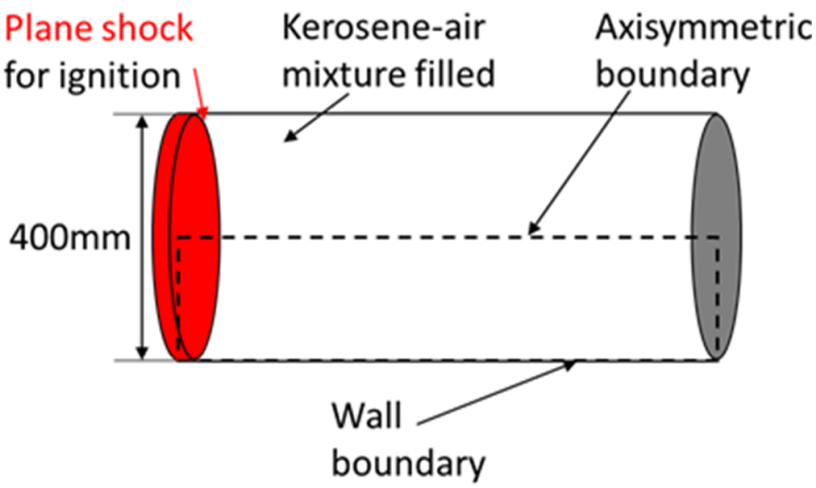

Fig. 3.3. Schematic of shock tube simulation for kerosene-air mixture detonation at various initial gas pressures

The transverse wave formation gives rise to the unstable Mach stems as triple points appear in the two-dimensional detonation propagation. Shown in Fig. 3.4 is a shadowgraph image of the resulting cell size for 1 bar initial gas pressure shown at 15μs. The cell width is approximately 40 mm, and the comparison between the experimental cell sizes for different pressure conditions is shown in Fig. 3.5. Higher initial gas pressure influences the CJ pressure, and thus triple point formation occurs sooner where the stronger incident shock and transverse waves leave the trace of narrower-width cells.

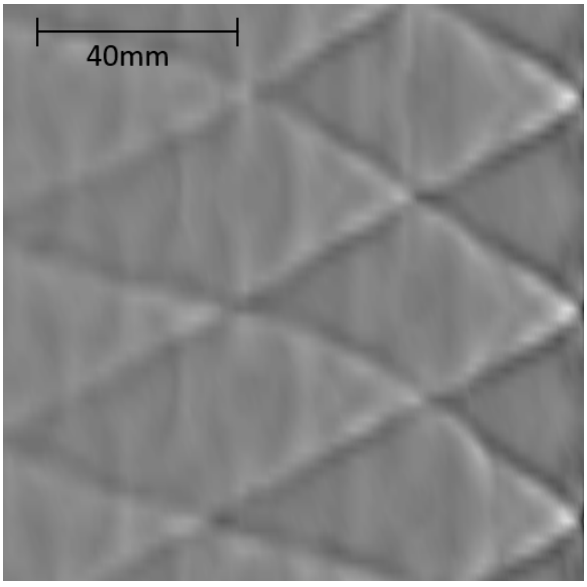

Fig. 3.4. Shadowgraph of calculated detonation cell structure of kerosene-air mixture at 1 bar initial pressure

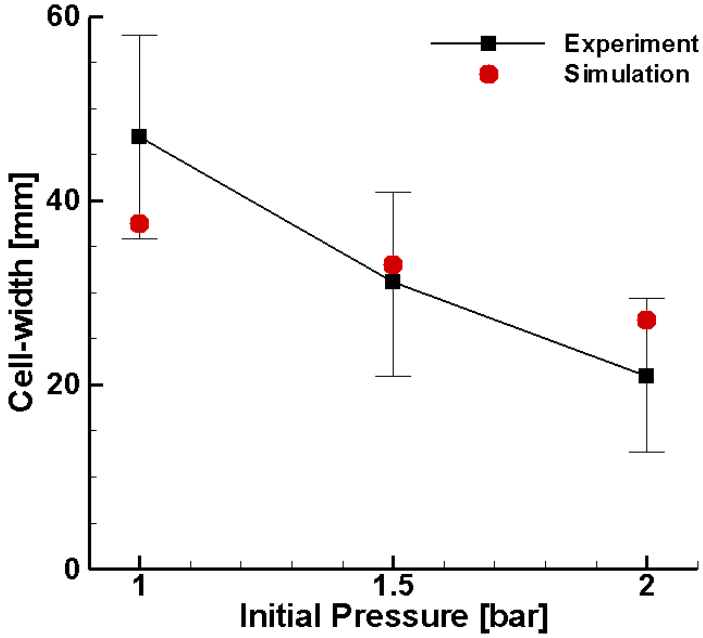

Fig. 3.5. Detonation cell width comparison for kerosene-air mixture for three different gas pressures

3.2 Solid energetic materials

3.2.1 Anisotropic PETN

In the reaction progress (Eq. 3.1), an anisotropic chemical kinetics based on the conventional form of the I&G model [31] was proposed to simulate a heterogeneous high explosive.

$$\dot{w} = I_{Ani}\left(1-Y_i\right)^b\Big|_{0\le Y_i<Y_{i,ig,\max}} + G_{1,Ani}\left(1-Y_i\right)^c Y_i^d p^Y\Big|_{Y_{i,G1,\min}<Y_i<Y_{i,G1,\max}} + G_{2,Ani}\left(1-Y_i\right)^e Y_i^g p^Z\Big|_{Y_{i,G2,\min}<Y_i<1} \tag{3.1}$$

To formulate the general anisotropic ignition, first growth, and second

growth terms in three dimensions, we assume that the dislocation and slip systems at the microscale[32, 33] are effective primarily in the early stages of shock initiation. Instead of directly modeling the dislocation and slip of the micro-structural system, we observe the strain field, which is closely related to the macroscopic variables. The ignition term in our chemical kinetics originates from the anisotropic characteristics, and we consider the anisotropic concept in addition to the isotropic term describing the initial growth of the reaction via pressure. In the model, we assume that the shock waves are sufficiently strong that the elasto-plastic behavior is negligible. The current model is general and can be extended to include the elasto-plastic effects if desired. For the later stages of the reaction, the second growth term was considered to only be dependent on the pressure. Accordingly, I_{Ani}, $G_{1,Ani}$, and $G_{2,Ani}$ in Eq. (3.1) are defined in Eq. (3.2).

$$
\begin{aligned}
I_{Ani} = I\Bigg[& f\left(\frac{\varepsilon_{<100>}}{\varepsilon_{<100>,0}}-1\right)H(\dot{\varepsilon}_{<100>}) + f\left(\frac{\varepsilon_{<010>}}{\varepsilon_{<010>,0}}-1\right)H(\dot{\varepsilon}_{<010>}) \\
& + f\left(\frac{\varepsilon_{<001>}}{\varepsilon_{<001>,0}}-1\right)H(\dot{\varepsilon}_{<001>}) + f\left(\frac{\varepsilon_{<110>}}{\varepsilon_{<110>,0}}-1\right)H(\dot{\varepsilon}_{<110>}) \\
& + f\left(\frac{\varepsilon_{<011>}}{\varepsilon_{<011>,0}}-1\right)H(\dot{\varepsilon}_{<011>}) + f\left(\frac{\varepsilon_{<101>}}{\varepsilon_{<101>,0}}-1\right)H(\dot{\varepsilon}_{<101>})\Bigg]^{X} \chi\left(\dot{\varepsilon}_{\exp}\right) \qquad (3.2) \\
G_{1,Ani} = [& G_{1,<100>}H(\dot{\varepsilon}_{<100>}) + G_{1,<010>}H(\dot{\varepsilon}_{<010>}) + G_{1,<001>}H(\dot{\varepsilon}_{<001>}) \\
& + G_{1,<110>}H(\dot{\varepsilon}_{<110>}) + G_{1,<011>}H(\dot{\varepsilon}_{<011>}) + G_{1,<101>}H(\dot{\varepsilon}_{<101>})]\,\chi\left(\dot{\varepsilon}_{\exp}\right) \\
G_{2,Ani} = & G_2
\end{aligned}
$$

Here, ε, $\dot{\varepsilon}$, $H(\dot{\varepsilon}_{<>})$, $\chi\left(\dot{\varepsilon}_{\exp}\right)$, and the function f are the strain, strain rate,

strain rate threshold function, an assessment function of whether a state of the explosive is in expansion or compression, and the positive part of its value, respectively. $H(\dot{\varepsilon}_{<>})$, $\chi\left(\dot{\varepsilon}_{\exp}\right)$, and the function f are defined in Eq. (3.3).

$$H(\dot{\varepsilon}_{<>}(t)) = \begin{cases} 1 & \text{if } \dot{\varepsilon}_{<>}(t_0) \le \dot{\varepsilon}_{<>,0} \text{ for <100>, <010>, <001> directions, any } t_0 \le t \\ \frac{1}{2} & \text{if } \dot{\varepsilon}_{<>}(t_0) \le \dot{\varepsilon}_{<>,0} \text{ for <110>, <101>, <011> directions, any } t_0 \le t \\ 0 & \text{otherwise} \end{cases} \quad (3.3\text{-}1)$$

$$\chi(\dot{\varepsilon}_{\exp}) = \begin{cases} 1 & \text{if } \dot{\varepsilon}_{<>} \ge \dot{\varepsilon}_{\exp} \text{ for <100>, <010>, <001> directions, any time} \\ 0 & \text{otherwise} \end{cases} \quad (3.3\text{-}2)$$

$$f(\text{value}) = \begin{cases} \text{value} & \text{if value} > 0 \\ 0 & \text{otherwise} \end{cases} \quad (3.3\text{-}3)$$

In Eq. (3.3), $\dot{\varepsilon}_{<>,0}$ are the reference strain rates. The range of the corresponding strain rate is between 10^7 s^{-1} and 10^8 s^{-1} in typical detonation phenomena. The purpose of the reference strain rate is to prevent initiation in response to a non-shock loading. The strain-based chemical kinetics of our anisotropic ignition model is intrinsically equivalent to the density-based chemical kinetics of the original I&G model; however, the former model has a vulnerability in multi-dimensional calculations. The I&G model implements a density function and restricts unphysical ignitions, violating the hot spot theory; however, the anisotropic ignition model based on the strain tensor inevitably experiences unphysical ignition near the edge of explosives due to the high magnitude of the negative strain. An expansion state representing the lateral region could be evoked by the proper positive value of the principal strain rate and used to effectively restrict incorrect calculations near the outer surfaces of explosives. A regulation term, $\chi\left(\dot{\varepsilon}_{\exp}\right)$,from the original anisotropic

chemical kinetics was added to counter any unphysical ignition that might occur in the lateral region of multi-dimensional explosives.

In other words, to consider anisotropic chemical kinetics, we hypothesize that (i) strain and strain rate dependent ignition is considered instead of neglecting the dislocation and slip system at the molecular scale, (ii) the anisotropic initiation of detonation is dependent on the impact (pressure) direction, (iii) the elasto-plastic behavior is negligible for strong impacts in the early stage of the simulation, and (iv) explosive runaway or growth is dominantly driven by the isotropic pressure.

Table 3.2. Parameters of the anisotropic ignition model.

Parameter [unit]	Value
I [μs^{-1}]	100
b, c, e, g	0.667
d	0.01
$\varepsilon_{<100>,0}$, $\varepsilon_{<010>,0}$, $\varepsilon_{<001>,0}$, $\varepsilon_{<110>,0}$, $\varepsilon_{<011>,0}$, $\varepsilon_{<101>,0}$	−0.199
X	8
$G_{1<110>}$ [$Mbar^{-Y}\,\mu s^{-1}$]	0.15
$G_{1<001>}$ [$Mbar^{-Y}\,\mu s^{-1}$]	0.015
$G_{1<100>}$, $G_{1<010>}$, $G_{1<011>}$, $G_{1<101>}$ [$Mbar^{-Y}\,\mu s^{-1}$]	0.001
Y	1
G_2 [$Mbar^{-Y}\,\mu s^{-1}$]	1500
Z	2
$Y_{i,\mathrm{G1min}}$	0
$Y_{i,\mathrm{igmax}}$, $Y_{i,\mathrm{G1max}}$, $Y_{i,\mathrm{G2min}}$	0.01
$\dot{\varepsilon}_{<110>}$,, $\dot{\varepsilon}_{<001>}$ [μs^{-1}]	−1600
$\dot{\varepsilon}_{<100>}$, $\dot{\varepsilon}_{<101>}$, $\dot{\varepsilon}_{<011>}$, $\dot{\varepsilon}_{<010>}$ [μs^{-1}]	−4200
$\dot{\varepsilon}_{\mathrm{exp}}$ [μs^{-1}]	0.1

Table 3.3 Parameters of the EOS for PETN[31]

Parameter [unit]	Unreacted	Reacted
ρ_0 [kg m^{-3}]	1778	-
A [GPa]	20208	1032.258
B [GPa]	−3.752	90.570
R_1	10	6
R_2	1	2.6
ω	0.568	0.57
C_v [GPa K^{-1}]	2.718e−3	1e−3
T_0 [K]	298	–
E_0 [GPa]	0	10.8

The pressure of the reacted states is determined via the Jones–Wilkins–Lee (JWL) equation of state (EOS).

$$P = A\left(1-\frac{\omega R_1}{V}\right)e^{-R_1 V} + B\left(1-\frac{\omega R_2}{V}\right)e^{-R_2 V} + \frac{\omega E}{V} \tag{3.4}$$

Tables 3.2 and 3.3 summarize the parameters of the anisotropic chemical kinetics and the EOS of PETN used for the numerical simulation. In Table 3.3, G_1 and $\dot{\varepsilon}_{<>}$ in the <101>, <011>, and <010> orientations are assumed to be insensitive as in the <100> orientation to eliminate ambiguity in the interpretation because there is no experimental data related to the <101>, <011>, and <010> orientations.

A series of problems was solved to test the anisotropic initiation in multi-dimensional reactive flows. Using 1D problems, the efficiency of AMR in terms of the computation time was checked by using a comparison between a uniform mesh and AMR with the same initial conditions. In addition,

experimental data were used to validate the anisotropic ignition model where plane shock initiation tests were used to analyze the reactive flow structure of single crystal PETN. In the 3D problem, the anisotropic initiation was confirmed by using various intensities of shock loading in the orientations including the <110>, <100>, and <001> and the development of strain in particular to a plane perpendicular to the impact (the left plane in Fig. 3.7), which has never been observed in the lower-dimensional simulations.

First, a 1D shock loading test (a shock impact test) of PETN was performed to validate our anisotropic chemical kinetics using the AMR technique. After impacting one end of the PETN, the shock wave progressed into the crystal. A uniform mesh of 2.5 μm per zone was used to adequately resolve the thin reaction length of 40 μm, and the shock loading varied from 8 GPa to 19 GPa. Figure 3.6 shows the pressure histories in the sensitive direction (the <110> direction) under the high-pressure shock loading (19 GPa) condition using a uniform mesh and AMR (max level = 4).

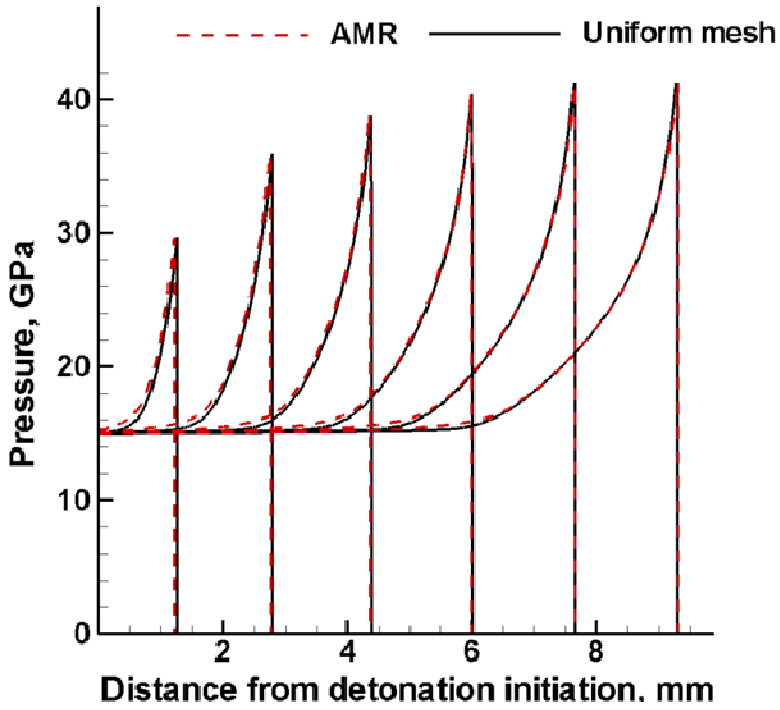

Fig. 3.6. Pressure histories of the PETN detonation in the 1D simulation under a shock loading of 19 GPa in the <110> direction using a uniform mesh or AMR (max level = 4).

This figure confirms that the detonation velocity is approximately 8400 m s^{-1} and that the peak front pressure is approximately 40 GPa; there are additional grids that were added to fully resolve the detonation front structure in the AMR calculation. Both the detonation velocities and the pressure profiles of these simulations are the same and reproduce the results of the previous study well[11]. The computation time for AMR is only 1/6 the computation time for the uniform mesh. When the run distance to detonation for various shock loadings are compared with the experiment[13, 32, 34, 35], our AMR results quantitatively reproduced the experimental data in the <110>

direction and captured the anticipated ignition behavior in the <001> direction, as did previous results on a uniform mesh[36]. Further details validating the anisotropic chemical kinetics associated with the 1D results have been described in our previous studies[12, 14].

An elaborate and full-scale 3D test in a rectangular system was performed. We observed additional features that have not been observed in the comparison groups (1D or 2D). Even though AMR is used in the 3D setup, the computational cost is dramatically increased by the dimensional augmentation, and therefore only a minimum requirement for the reaction front resolution is enforced in the preliminary attempt here. A quarter of the PETN crystal was simulated, and the computation domain is shown in Fig. 3.7(a). The impact boundary has a size of 0.65 mm × 0.65 mm, and the front surface has a detonation running distance of 0.65 mm. For the <100>, <001>, and <110> cases, the impact surface (front surface) is the yz-plane, the xy-plane, and the y'z'-plane, respectively. The left and bottom surfaces are the cutting surface of the PETN crystal with symmetric boundary conditions. The top and right surfaces are the outer surface of the crystal and are set to a void condition, which is defined in a previous paper[14]. The back surface is a cross section of the crystal, and a zero-gradient boundary condition is applied. The initial computational mesh in which the base mesh size is 40 μm was shown in Fig. 3.7(b), and the maximum level is three. A mesh size of 5 μm, which adequately resolves the thin reaction length of 40 μm, was used near discontinuities including shocks or detonations. Mesh refinement is observed near the detonation front as well as a reflected wave similar to that in Fig.

3.7(c), which is an example of the mesh distribution during detonation propagation.

In this study, three different shock loadings, i.e., 12 GPa, 20 GPa, and 32 GPa, were applied in various orientations with various sensitivities, i.e., in the sensitive, <110>; middle sensitive, <100>; and insensitive, <001> directions. To simulate the <110> direction initial loading on the x-axis, the calculation domain was rotated by 45° about the z-axis. The new axes X', Y', and Z' are defined by Eq. (3.5).

$$\begin{pmatrix} X' \\ Y' \\ Z' \end{pmatrix} = \begin{pmatrix} \cos(\pi/4) & -\sin(\pi/4) & 0 \\ \sin(\pi/4) & \cos(\pi/4) & 0 \\ 0 & 0 & 1 \end{pmatrix} \begin{pmatrix} X \\ Y \\ Z \end{pmatrix} \tag{3.5}$$

Figure 3.8 shows the response of the detonation initiation in each direction under the same incident shock loading, 12 GPa, using pressure and product ratio contours at 0.47 μs. In this figure, only the shock loading in the <110> direction develops into detonation and changes the product ratio of PETN from zero to one. Conversely, the product ratios of the other cases are not changed during the calculation even though the shock passes through the PETN single crystal. The chemical kinetics permits ignition if the strain rate exceeds the relatively small reference strain rate prescribed for the crystal along the shock travel direction of <110>. An impact pressure of 12 GPa is considered to be very low, and yet the ensuing detonation along this direction is possible due to the strain-governed ignition mechanism. The current strain rate in the <001> and <100> directions is substantially lower than the reference strain rate corresponding to a Chapman–Jouguet (C–J) pressure. Therefore, ignition is naturally prohibited over the entire domain and

dissipated shock (~2 GPa) is shown in Fig. 3.8 (b) and (c). In these figures, an interference wave pattern appears inside the unreacted crystal PETN due to a reflected shock wave from the wall.

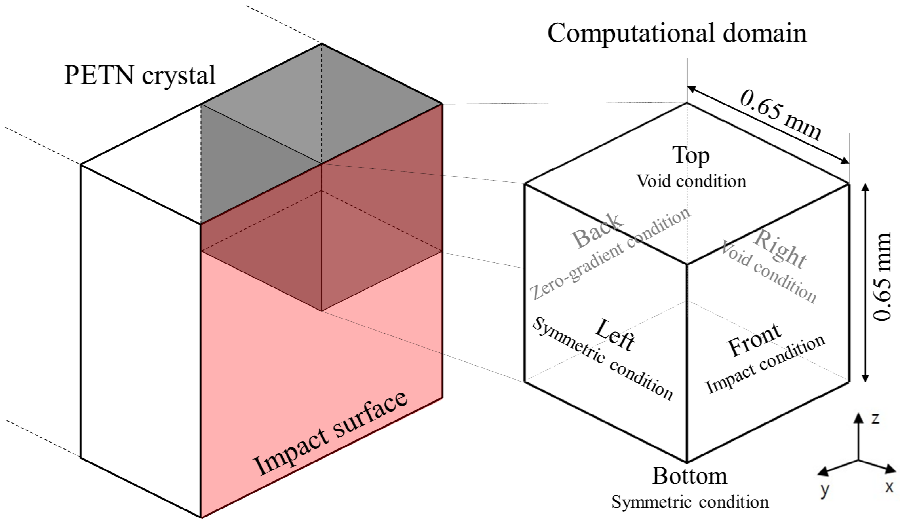

(a)

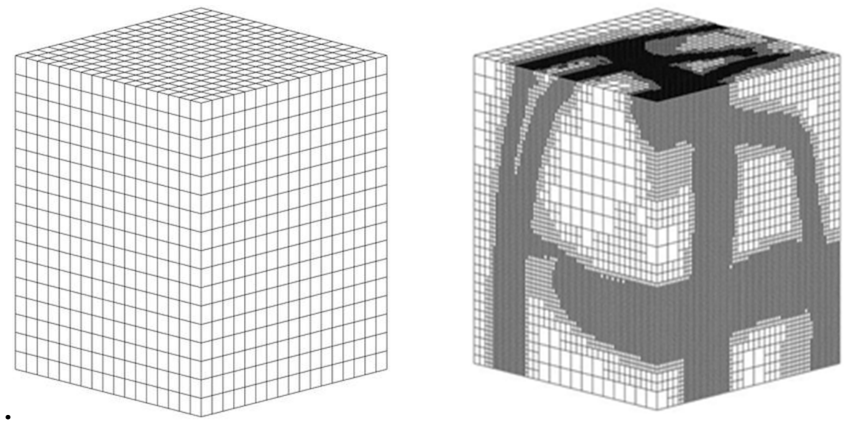

(b) **(c)**

Fig. 3.7. (a) Schematic of the 3D simulation setup, (b) the initial mesh distribution, and (c) an example of the mesh distribution during detonation propagation (impact loading of 32 GPa in the <100> direction at 0.08 μs).

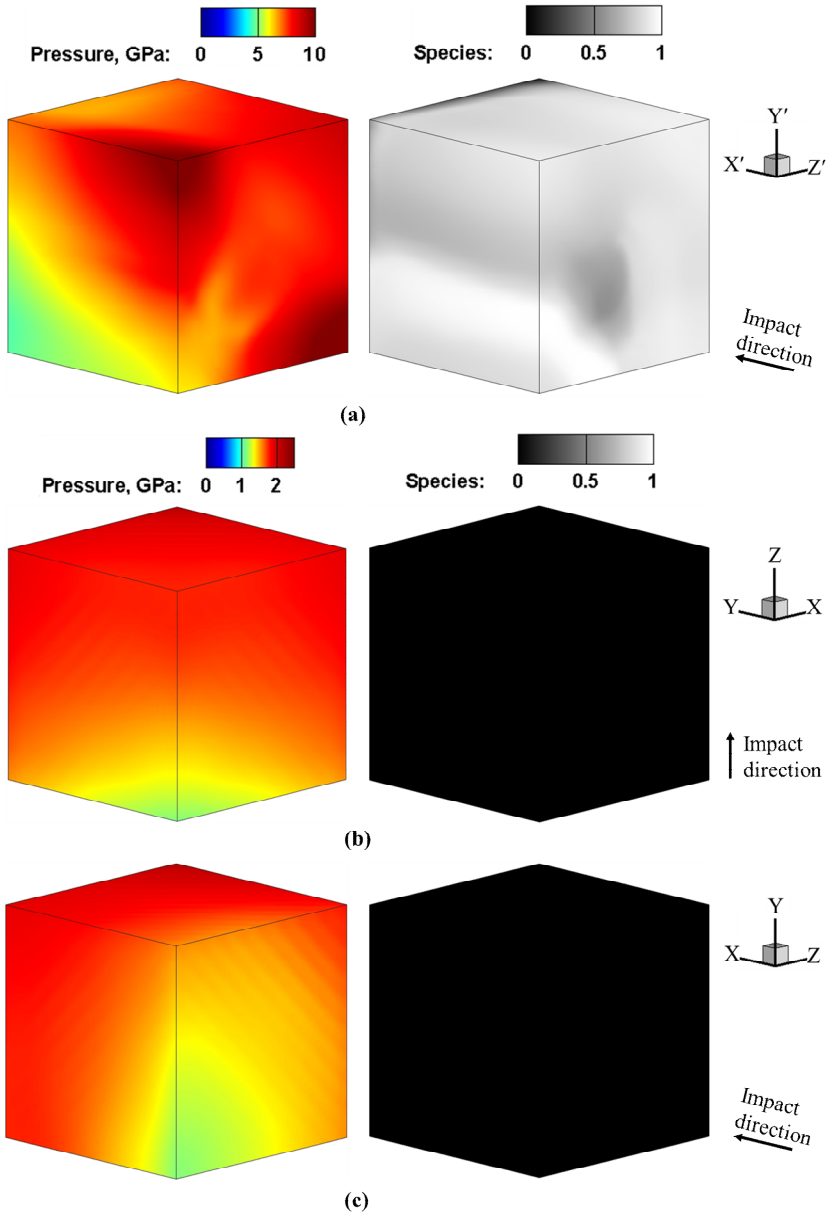

Fig. 3.8. Pressure contours (upper) [unit: GPa] and product ratio (lower) for (a) the <110> direction, (b) the <001> direction, and (c) the <100> direction (impact loading of 12 GPa at 0.47 μs).

When a stronger impact loading of 20 GPa is applied, not only does detonation develop within a relatively short time but also the <001> direction, which does not develop into a detonation at 12 GPa, develops into a detonation, as shown in Fig. 3.9 using the pressure and product ratio contours according to the shock loading directions at 0.11 μs. Figure 3.10 shows the line contour at the bottom surface (the cutting plane) where the <100> and <010> direction strain rates due to the loading shock and reflected shock wave from the right boundary (see Fig. 3.11) are greater than 0.1 μs^{-1} at 0.09 μs just before ignition. The <100> and <010> direction strain rates have a significant effect on the ignition of PETN. In Fig. 3.10. (a), the <110> case, and Fig. 3.10. (b), the <001> case, the strain rates are sufficiently strong to develop detonation and the cross sections are located near the center of the crystal; however, in Fig. 3.10. (c), the <100> case, the stain rates do not overlap and ignition fails. Therefore, we can predict that ignition occurs at the center of the PETN crystal in the cases of <110> and <001>. Figure 3.12 shows the reaction propagation in PETN via the isosurface of the reaction progress variable. The computational domain is shown with the mirror image on the bottom side. The isotropic ignition model is ignited according to the pressure loading regardless of the direction; therefore, ignition begins on the impacted plane, as shown in Fig. 3.12. (c). The anisotropic ignition model, however, predicts the hot spot using the strain rates in the sensitive directions. In the case of 20 GPa, because impact loading is in the <110> and <001> directions, ignition is delayed until a sufficiently large strain rate is concentrated at the center of the crystal representing the generation of the hot

spot, as shown in Figs. 3.12. (a) and (b). The hot spot is generated away from the impact surface, and the combustion propagates in a spherical form. The initial pressure in <110> and <001> cases are similar to ~27 GPa and detonation was not fully developed. In the Fig. 3.13., the values of run distance are 0.45 mm for <110> case and 0.6 mm for <001> case. The differences arise due to the propagation speed of the reaction, which depends on the sensitive direction. From the simulation results, if the geometry and size of crystals are similar, the ignition position and run distance might be similar at various lower pressure loads for the same direction. On the other hand, if sufficient pressure is applied to generate detonation initially, the high pressure of the detonation induces a reaction regardless of the crystal orientation sensitivity. Therefore, same C-J pressure and velocity are shown in fully developed detonation and the development of detonation is also similar to the isotropic model.

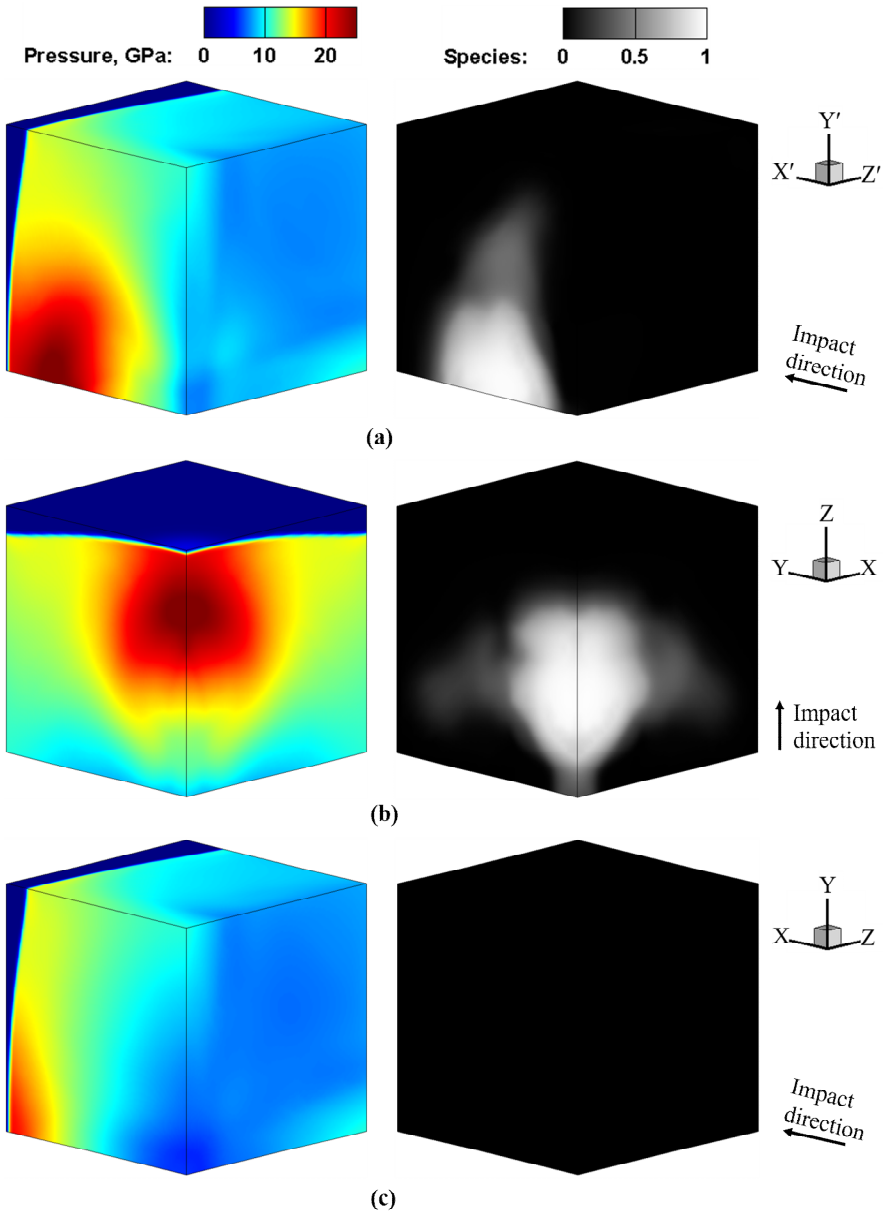

Fig. 3.9. Pressure contours (upper) [unit: GPa] and product ratio (lower) for (a) the <110> direction, (b) the <001> direction, and (c) the <100> direction (impact loading of 20 GPa at 0.11 μs).

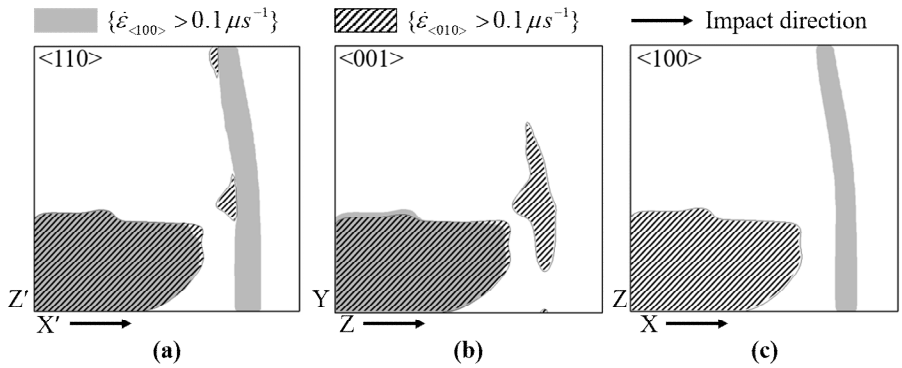

Fig. 3.10. Line contour at the bottom surface where the strain rate is greater than 0.1 μs−1 at 0.09 μs with an impact loading of 20 GPa in (a) the <110> direction, (b) the <001> direction, and (c) the <100> direction.

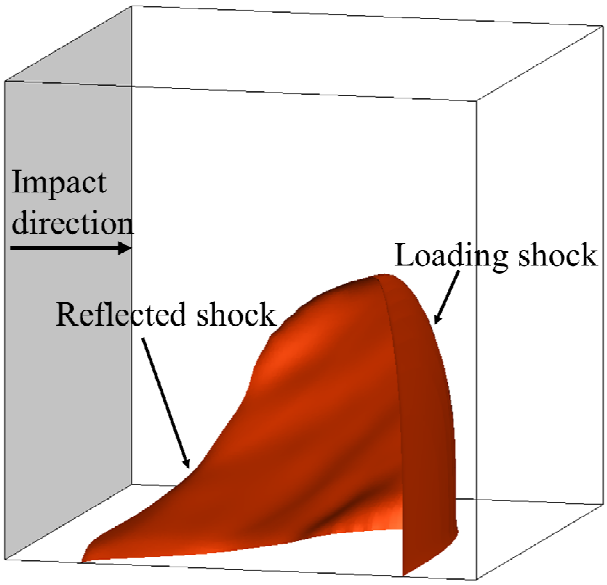

Fig. 3.11 Isosurface result of pressure (p = 15 GPa) at 0.09 μs with an impact loading of 20 GPa.

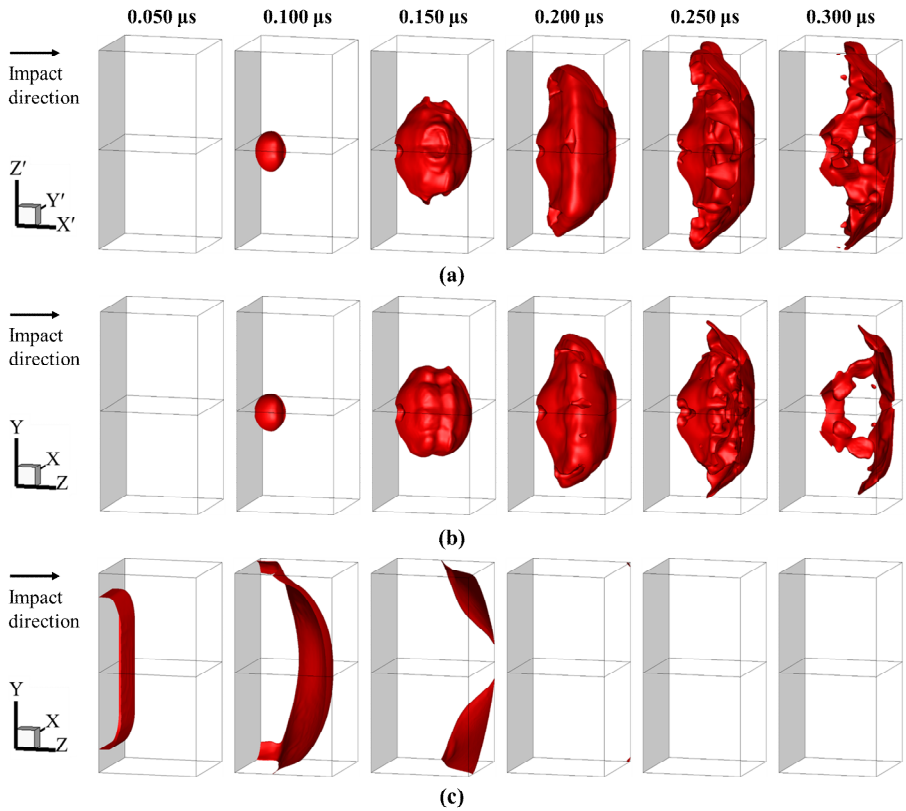

Fig. 3.12. Isosurface results of the reaction progress variable (λ = 0.85) at 0.050 μs, 0.100 μs, 0.150 μs, 0.200 μs, 0.250 μs, and 0.300 μs for impact loading of 20 GPa in (a) the anisotropic <110> direction, (b) the anisotropic <001> direction, and (c) the isotropic <001> direction.

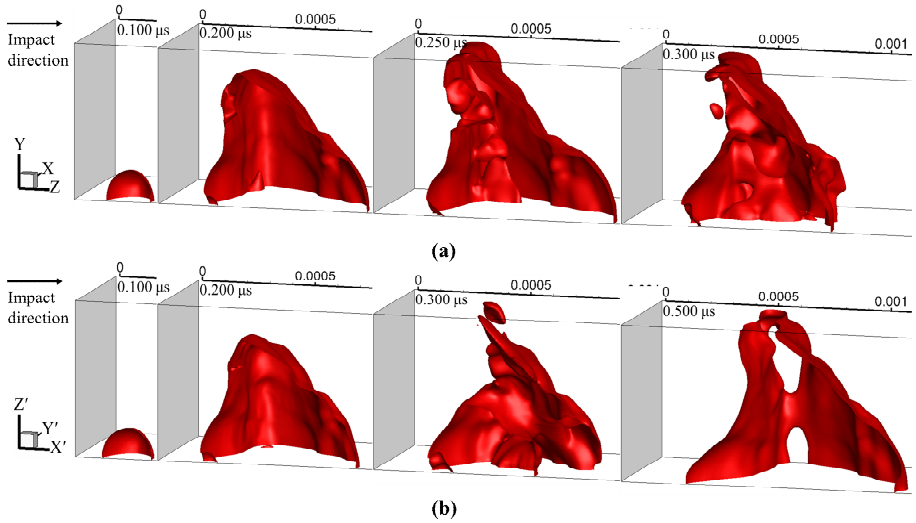

Fig. 3.13. Comparison of the isosurface (λ = 0.85) results for the anisotropic (a) <110> and (b) <001> direction cases with an impact loading of 20 GPa.

So an extremely strong shock loading of 32 GPa was consider as the impact loading in the <110>, <001>, and <100> directions. The PETN is ignited at 32 GPa for impact loading in all directions (see Fig. 13), and immediate ignition occurs because the induced strain rate due to the impact loading exceeds the reference strain rate for each direction. The responses of the anisotropic ignition model for various impact directions are displayed in Table 4 using go and no-go to represent ignition and non-ignition, respectively. The proposed anisotropic chemical kinetics and its numerical implementation seem very plausible, and the proposed anisotropic chemical kinetics can properly address the response of single crystal PETN subject to a directional shock loading for various innovative ignition purposes.

3.3 Structure deformation

3.3.1 Taylor impact problem

To confirm the plastic behavior of metal (copper) listed in Table 3.4, Taylor impact problem is considered that is a variant of the example considered in House et al. [37] based on three-dimensional rectangular coordinate. The schematic of the problem is shown in Fig. 3.14. The top, right, and left boundary conditions are zero gradient, wall, and zero gradient conditions, respectively.

Table 3.4 Initial conditions and material properties of the solid

Parameters	Copper [14, 17]	304 Stainless Steel [38]	Concrete [39]
Initial density, ρ_0	8930 kg/m^3	7900 kg/m^3	2400 kg/m^3
Shear modulus, G	45 GPa	77.5 GPa	9.8 GPa
Yield stress, Y	90 MPa	110 MPa	-
Gruneisen coefficient, Γ_0	2.0	1.93	1.22
Normal sound speed, c_0	3940 m/s	4570 m/s	2770 m/s
S	1.49	1.49	1.44
Thermal conductivity, k	400 W/(m-K)	16.2 W/(m-K)	2.5 W/(m-K)
Poisson's ratio, v	0.35	0.29	0.20
Melting temperature, T_m	1358 K	1694K	-

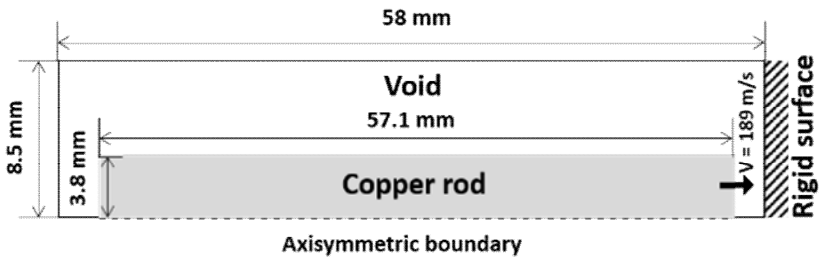

Fig. 3.14. Schematic of 2D & 3D cylinderical calculation setup for Taylor problem

Impact of rob is described by prescribing an initial particle velocity which is 189 m/s. Figure 3.15 shows the histories of kinetic, internal, and total energy densities, and indicates that the kinetic energy fully converts into internal energy under total energy conservation condition. The deformation stops at approximately 80 μs after the impact of copper rod and rigid wall.

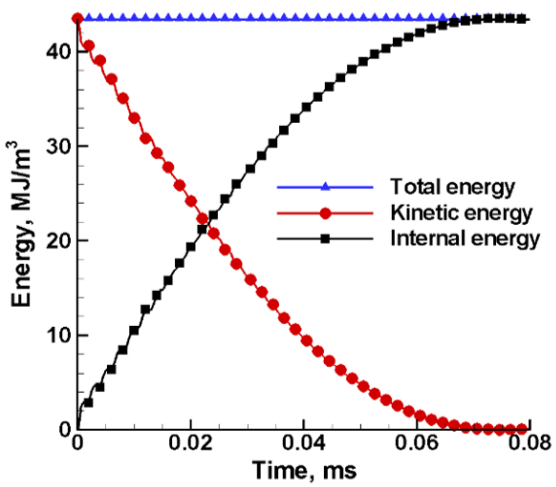

Fig. 3.15. Histories of the values of total, kinetic, and internal energy density under Taylor impact.

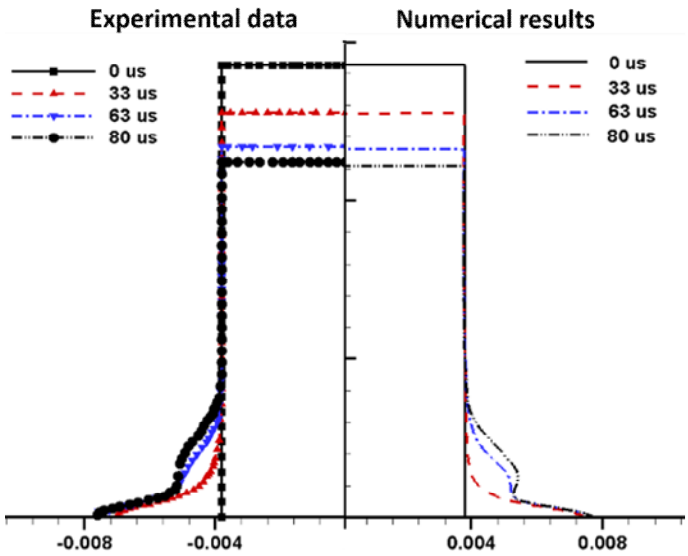

Fig. 3.16 Comparison between experimental data [37] and numerical results of copper rod shape.

Figure 3.16 and Table 3.5 show the comparison between the experimental data and the numerical results in deformed shape of the rod. The calculation error was 6~10% at early time (at 33 μs). And the results approach the measurement with error declined to 0.4~4 % with the time increase.

Table 3.5. Comparison between experimental data and simulation results

Time	**Experiment[37]**		**Simulation**	
	Length	Bottom radius	Length	Bottom radius
33 μs	51.34 mm	7.02 mm	50.97 mm	7.44 mm
63 μs	46.87 mm	7.68 mm	46.37 mm	7.70 mm
80 μs	44.89 mm	7.68 mm	44.33 mm	7.70 mm

3.4 Fluid-structure interaction method

An elastic vibration of a steel rod subjected to a high velocity fluid flow was considered to validate the strongly coupled FSI. The initial condition and two dimensional computational domains are shown in Fig. 3.17. The boundary conditions on top, bottom, left, and right are all outflows (or zero-gradient boundaries), slip, inflow (200 m/s), and outflow conditions, respectively. The 304 stainless steel parameters are as listed in Table 3.4.

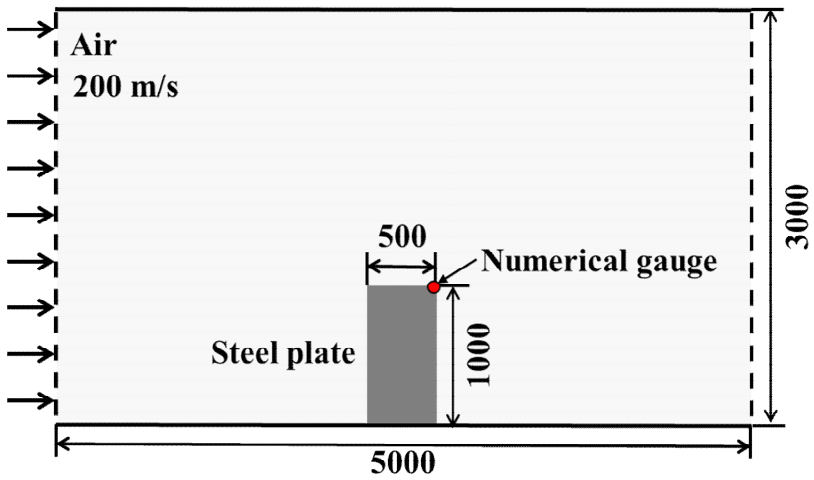

Fig. 3.17 Computational domain of steel bar vibration by a high speed uniform flow (length unit: mm).

Figure 3.18 shows the fluid pressure field and the elastic deformation recovery of the steel rod for increasing time sequences. In Fig. 3.18 (b), the steel rod is bent by the uniform flow from the left and the pressure increase is shown in the front tip of the rod. Figure 3.18 (c) is the elastic recovery which

resets the bent rod back to initial position. In the rear and top regions of the rod, the fluid pressure field is consistently changed in accordance with rod vibration. A gauge is placed at the edge of the rod and the results are compared with the ANSYS prediction. Figure 3.19 shows that the rod displacement compared to ANSYS is quite similar with the maximum displacement of 0.078 mm and frequency of 3.7 Hz.

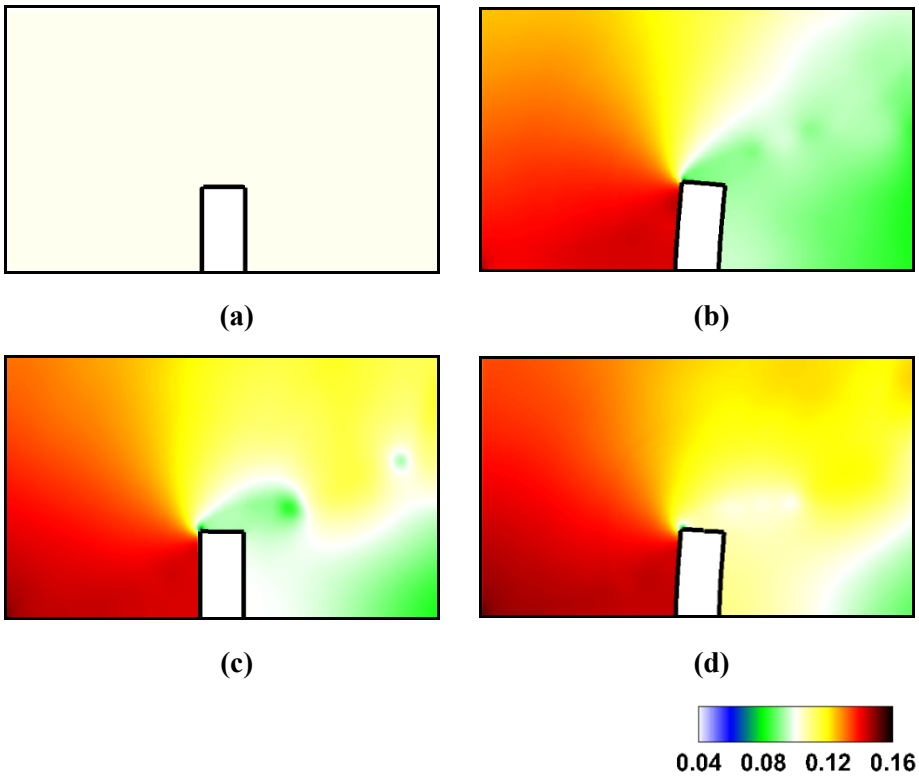

Fig. 3.18. Snapshots of air pressure fields and steel rod deformation & recovery [unit: MPa] at (a) 0 s, (b) 0.12 s, (c) 0.29 s, and (d) 0.44 s.

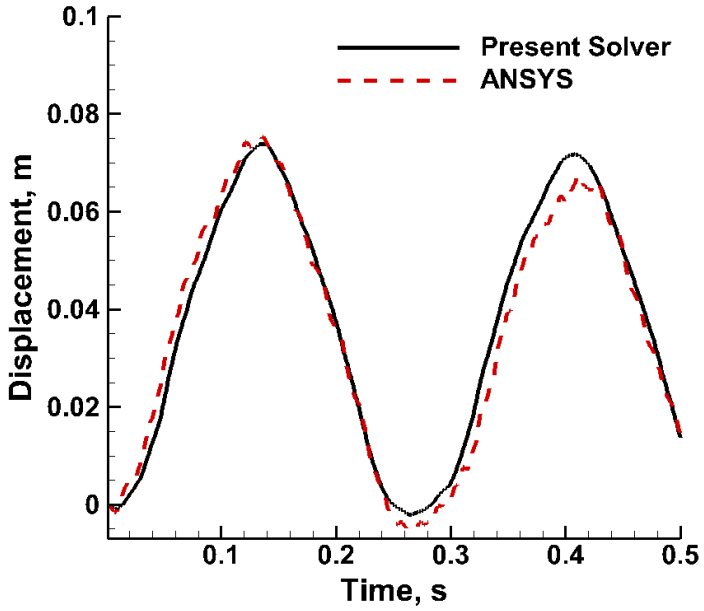

Fig. 3.19. Comparison between present solver and reference (ANSYS) using displacement histories in each numerical gauge.

Chapter 4. Vertical Launching System

4.1 Background and motivation

This reactive flow and structure interaction method is applied to a large deformation problem occurring when a vehicle launch system (VLS) rear cover opens and closes. During VLS operation, the rear cover rapidly deforms in milliseconds when opening at the high temperature (~2000 K) and pressure (6 bar) of the launch vehicle exhaust. Previously, for safety reasons, the fixed rear cover was analyzed in closed and opened states, and the plume dynamics were calculated in 1-D, 2-D [40-42] and in 3-D simulations [43, 44]. In this case, the rear cover deformation was not considered in the flow dynamics coupled with rocket structural changes during launch. Therefore, the rear cover pressure load induced from the exhaust plume was not calculated. In this work, the strongly coupled FSI between the rocket plume and the rear cover undergoing large deformation during opening and closing makes it possible to predict the resulting pressure distribution within the plenum. This also allows estimating the closing time for the neighboring rear cover in a paired VLS fresh launch.

Figure 4.1 shows the canister cross section view. When the missile is fired, the rear cover is deformed by the high pressure exhaust plume that fills the lower plenum with strong acoustic and shock waves that are reflected and transmitted.

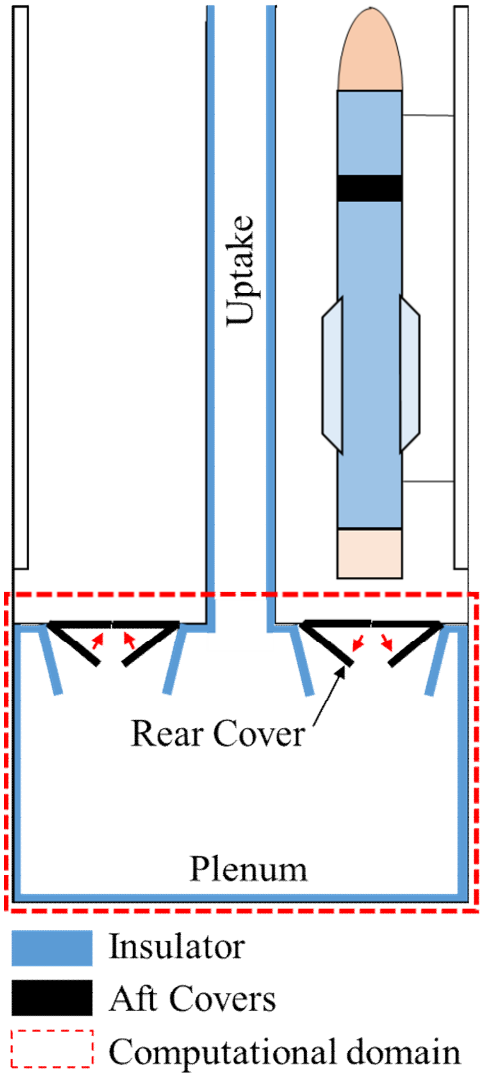

Fig. 4.1. Schematic diagram of a pair of launching tubes, separated by the plume exhaust uptake.

In this study, the rear cover deformation due to exhaust plume is a major concern. However, a three-dimensional VLS simulation with strong FSI demands extremely high cost for simulation. Alternatively, the problem is

reconfigured in two dimensions as shown in Fig. 4.1. Here, by cutting the VLS along a center axis of the two canisters and including the opening and closing of the rear covers. In each domain, the dynamics of plumes inside and deformation of each rear cover (either open or closure) can be as well represented by the two-dimensional flow. Case I is opening of the rear cover during the rocket launch. Case II is closing of the rear cover by the plenum pressure. In Case I, the rear cover is considered as either a elastoplastic plate or a inflexible plate which is fixed to a spring hinge. Both are simulated under the same loading by the rocket exhaust plume and different plume flows are observed.

Since there is no measured data of pressure or temperature in the plenum for monitoring the rear cover dynamics, the numerical simulation based on the modeled AP propellant combustion and subsequent pressure loading of the plume is used to understand the cover behavior. Inflexible plate was only considered in Case II, because the real rear cover is composed of both steel and a composite insulator. As the insulator is brittle and thicker than the steel cover, the deformation behavior of the rear cover is considered inflexible.

4.2 Results and discussion

4.2.1 Incoming rocket plume modeling

Figure 4.2 shows the calculation domain of the VLS, and in particular the boundary conditions around the red-dotted region for Case I are defined. In the figure, solid line defines the wall boundary while dash line is the zero-

gradient flow out condition. The top boundary is the incoming flow condition where the rocket exhaust plume is dispersed. A reacted or product gas of the AP/HTPB rocket plume is considered to be composed of elements listed in Table 4. Using the plume gas composition, the initial density, velocity, temperature and pressure of the hot product gas from the exhaust nozzle can be defined.

Table 4.1. Rocket plume composition AP/HTPB propellant for CEA input

Parameter	**AP/HTPB [45]**
Mole fraction of CO	0.26995
Mole fraction of CO2	0.04621
Mole fraction of Cl	0.00048
Mole fraction of H	0.00105
Mole fraction of HCl	0.14745
Mole fraction of H2	0.22737
Mole fraction of H2O	0.23329
Mole fraction of NH3	0.00002
Mole fraction of N2	0.07395
Mole fraction of OH	0.00021

The incoming velocity of the plume is determined by Eq. (4.1) by assuming the isentropic flow in a converging-diverging nozzle and the steady state condition of the combustion chamber, neither of which are included in the calculation domain.

$$u_e(t) = \sqrt{2\left(\frac{\gamma R}{\gamma - 1}\right) T_0 \left[1 - \left(\frac{p_e(t)}{p_0}\right)^{\frac{\gamma-1}{\gamma}}\right]} \tag{4.1}$$

Here, u_e, t, γ, R, T_0, p_e and p_0 are nozzle exit velocity or the plume velocity, time, specific heat ratio, gas constant, stagnation temperature, plume pressure, and stagnation pressure, respectively. Table 5 summarizes the rocket plume parameters obtained by running the NASA CEA code[46] using the presumed mole fractions in Table 4.1.

Table 4.2. Rocket plume parameters obtained from CEA calculation

Parameters	**NASA CEA [46]**
Specific heat ratio, γ	1.245
Gas constant, R (J/kg·K)	382.7
Stagnation pressure, p_0 (bar)	76.86
Stagnation temperature, T_0 (K)	2155

The initial plume pressure, $p_e(0)$ at position C in Fig. 4.2 is assigned 1 bar at 2000 K and Mach number 2.3, with initial density defined by the ideal gas equation of state. At every time step update, the transient incoming plume boundary condition is determined by Eq. (4.1) with $u_e(t)$ extrapolated from position C in Fig. 4.2.

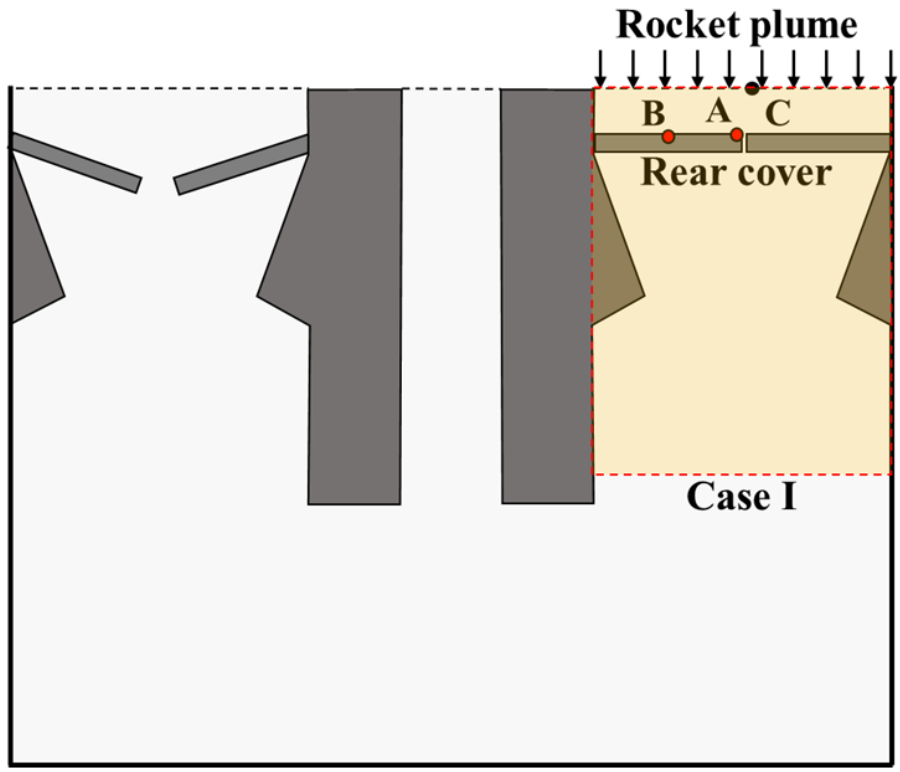

Fig. 4.2. Computational domain of the Case I (opening of launch tube rear cover) and Case II (closure of opened rear cover of left launch tube

4.2.2 Case I. Opening of the Rear Cover

The numerical simulation of the rocket plume loaded onto the elastoplastic rear cover was performed. Figure 4.3 shows the shadowgraph and temperature contours at 1.5, 2, 3, and 4 ms. In these figures, the complex plume dynamics and reflected acoustic waves are shown during rear cover opening. Two interesting points evident in the simulation are the contact surface formation

and the jet flow through the opening rear covers. The contact surface between the high temperature rocket plume and the cold air above the cover was observed and remained at all times. Noticeably, the hot plume gas never touches the cover plate during opening. Therefore, any temperature effect on the metal deformation may be neglected. This finding that thermal deformation does not play a significant role is important. The resulting jet forms a nozzle that allows hot gases to bypass the metal covers during the launch. From Fig. 4.3, one can see that then rear cover deformation pattern gives rise to the jet flow pattern resulting in a very complex flow and acoustic fields in the plenum.

The real source of rear cover deformation is the compressive force of the rocket plume. So the pressure account on rigid (closed) rear covers was taken into and compare that to the elastoplastic rear covers. Figure 4.4 shows the history of pressure readings at the rigid wall and two deformation plate locations. The fluid velocity near the wall becomes zero during the impact, and the pressure is doubled. After 0.2 ms, the pressure reaches 4 atm, which is twice the plume pressure, and remains at a high value. In the elastoplastic plate cases, the pressure starts to decrease once the plate opens and deforms. In particular, the pressure near the side wall (Point B) is higher than the pressure at the plate tip (Point A) because the flow velocity in the proximity of the tip is higher than at the nearby side wall. This indicates that the pressure boundary conditions for the Lagrangian solver are not uniform, and experimentally obtained pressure data would be invaluable for enhanced future calculations.

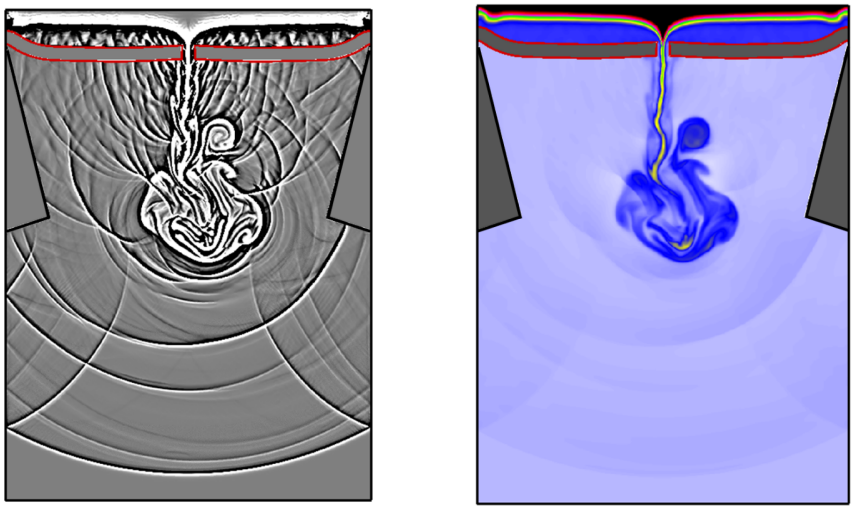

(a)

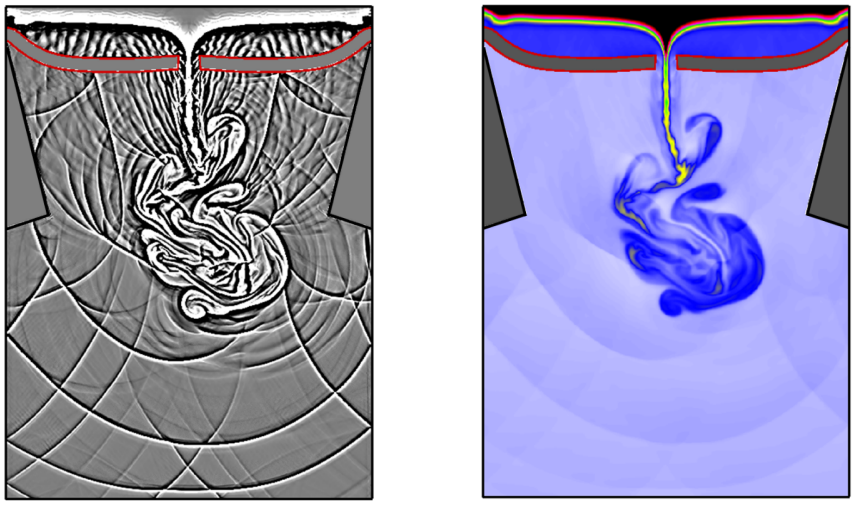

(b)

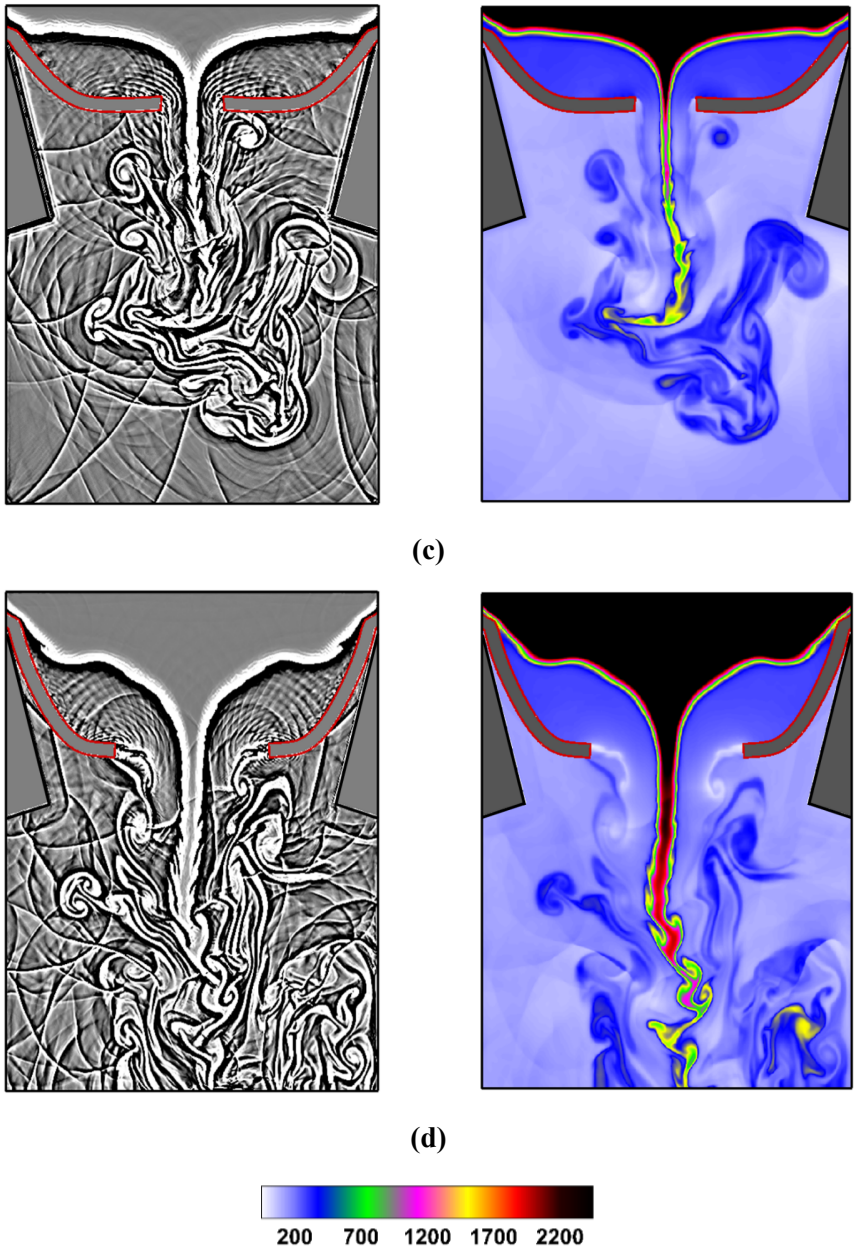

Fig. 4.3. Snapshots of shadowgraph (left) and temperature [unit: K] fields (right) coupled to the elastoplastic rear cover during opening at (a) 1.5 ms, (b) 2.0 ms, (c) 3.0 ms, and (d) 4.0 ms.

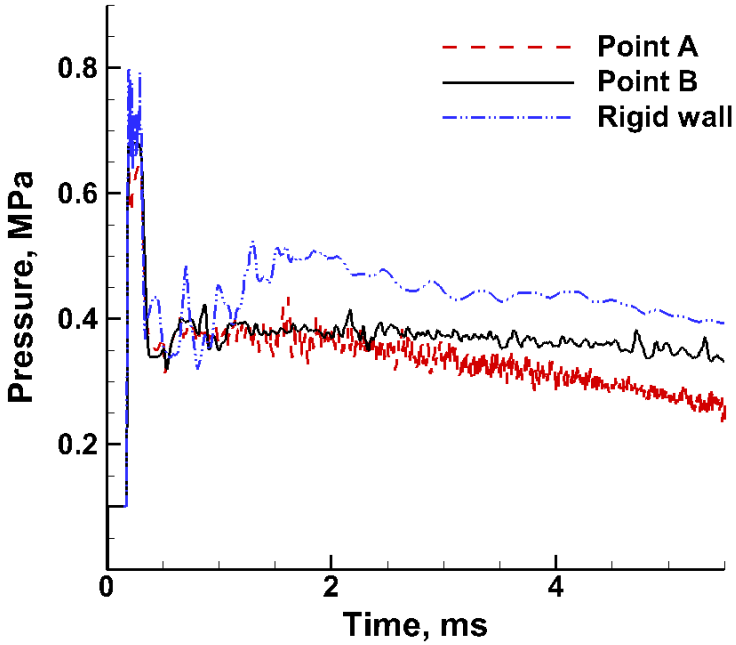

Fig. 4.4. Pressure history during rear cover opening recorded at positions A and B. Rigid wall corresponds to a pressure if both covers are assumed rigid and remained closed at all times

Next, inflexible rear cover plate deformation was considered by a fully reacted rocket plume. Figure 4.5 shows the shadowgraph and temperature contours at 1.5, 2, 3, and 4 ms. In this figure, the angular speed of the rear cover is almost the same as that of the elastoplastic case, but the tip deformation speed is approximately three times faster. Therefore, the jet flow due to the hot rocket plume is not seen in the inflexible plate case as shown in Fig. 4.5. (b). It is seen in the flexible plate case shown in Fig. 4.3. (b), although though the contact surface and shock propagation of both plates are nearly identical in the early stages. However, later in the inflexible plate case,

which opens more quickly, the velocity of the rocket plume increases. This can be seen by comparing Figs. 4.3. (d) and 4.5. (d). These observations point to the differences in plume speed and temperature distribution near the tip in each simulation. The rocket plume can ablate the VLS structure. Therefore, predicting the rocket plume around the structure is quite essential, especially around the rear cover and bottom of the VLS.

Due to severity of the detection environment near the rear cover, actual experimental data does not exist except for total deforming time, which was reported to be about 4 ms. In the simulations, the deforming time was calculated as 4.3 ms in flexible case and 3.8 ms in inflexible case. Therefore, the solid properties and pressure loading by the hot rocket plume were reasonable and simulation results can predict the flow conditions inside of VLS.

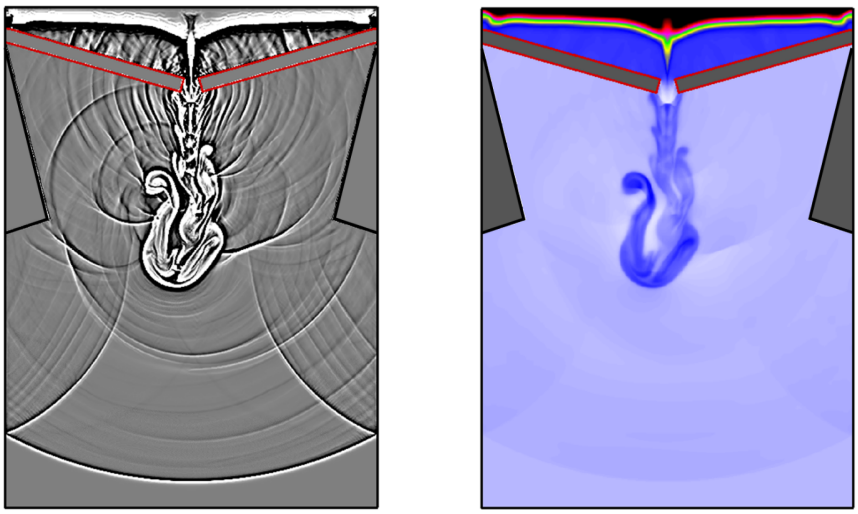

(a)

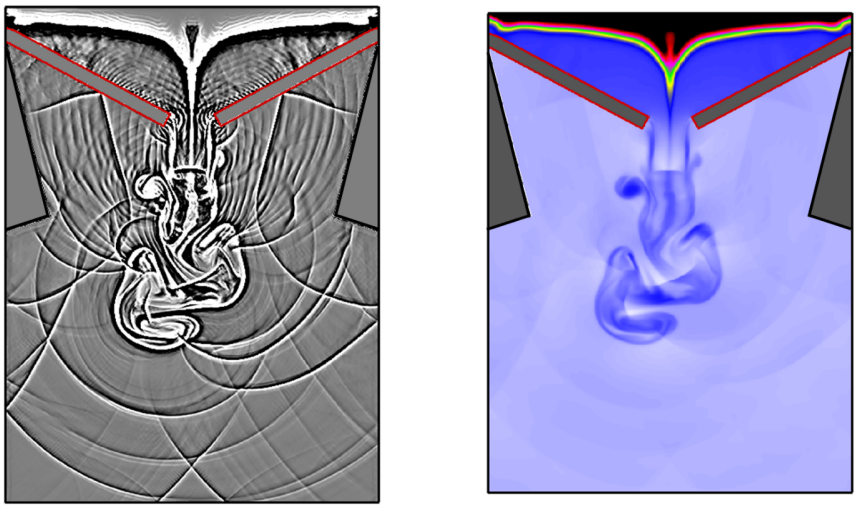

(b)

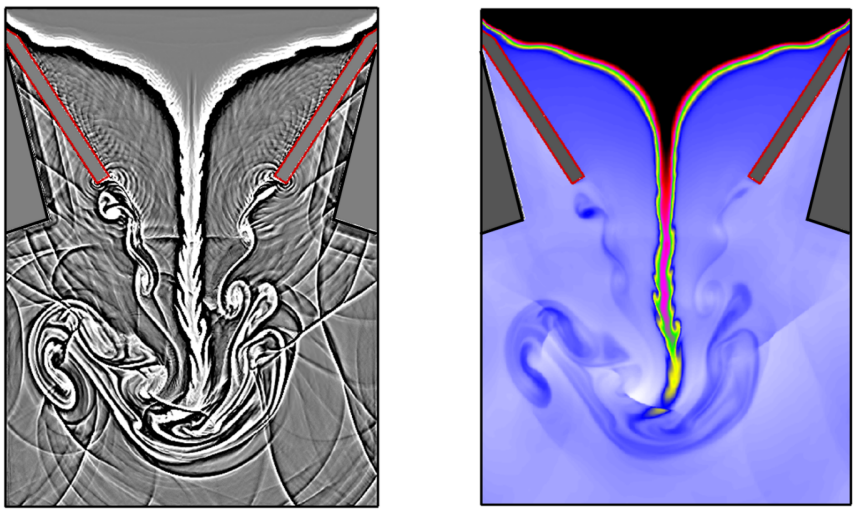

(c)

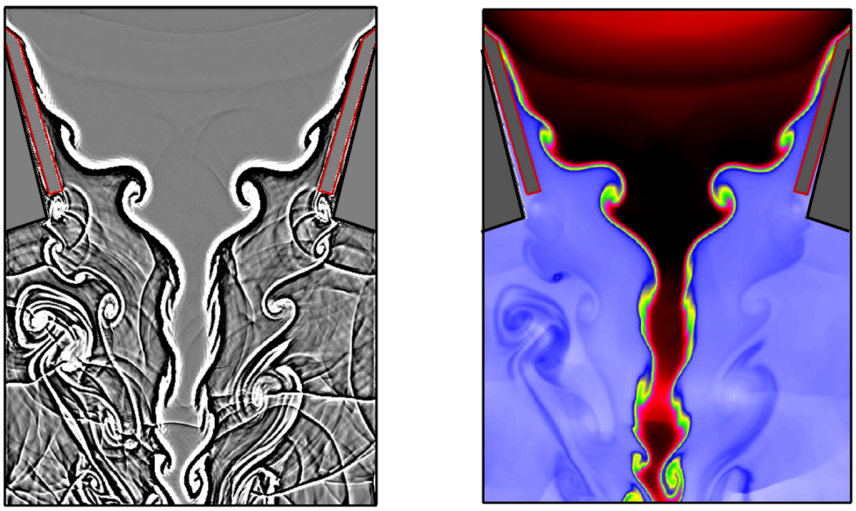

(d)

Fig. 4.5. Snapshots of shadowgraph (left) and temperature [unit: K] fields (right) coupled to the inflexible rear cover during opening at (a) 1.5 ms, (b) 2.0 ms, (c) 3.0 ms, and (d) 4.0 ms.

4.2.3 Case II. Closure of the Opened Rear Cover after Launch

In order to estimate the time elapsed for closure of the opened rear covers (on the left tube) by the launch of a fresh VLS tube (on the right), an extended domain is considered in Fig. 4.2. Only the inflexible rear cover is considered in the full calculation. The plume boundary condition on the top, initial conditions, and material properties are identical to Case I.

Figure 4.7 shows the hot gas propagation lead by multiple shock waves through the shadowgraphs. In early stages (Fig. 4.7 (a) and (b)), complex plume flow and reflected and transmitted shock waves are generated during opening of the right side launch tube. In Fig. 4.7 (c) and (d), a series of shock waves propagate towards the right side launch tube, followed by the distorted plume flows that also arrive at the used rear covers on the left. The primary shock wave, that makes heads on to the rear covers, pushes the cover to its original position and shuts it closed. This closure occurs at about 7 to 8 ms when the hot covers are completely closed as shown Figs 4.7 (d)-(f). Once closed, the hot gas plume has to find an alternative exit to depressurize and leaves through the center uptake as shown in Fig. 4.6 in the temperature contour. The hot gas or the flame speed through this uptake can be estimated from Fig. 4.6. (b) knowing the time elapsed and the length of the uptake chamber. The thermal condition in the plenum as well as maximum temperature induced near the rear cover are well predicted to be ~2000 K at 4~5 ms. This simulated thermal distribution is also useful for the design of any VLS insulator. Without the strongly coupled strategy for a combined

Lagrangian-Eulerian method, various hydrodynamic phenomena induced by transient structural changes, including the opening and closing of VLS rear covers by a hot rocket plume, would not have been captured and understood.

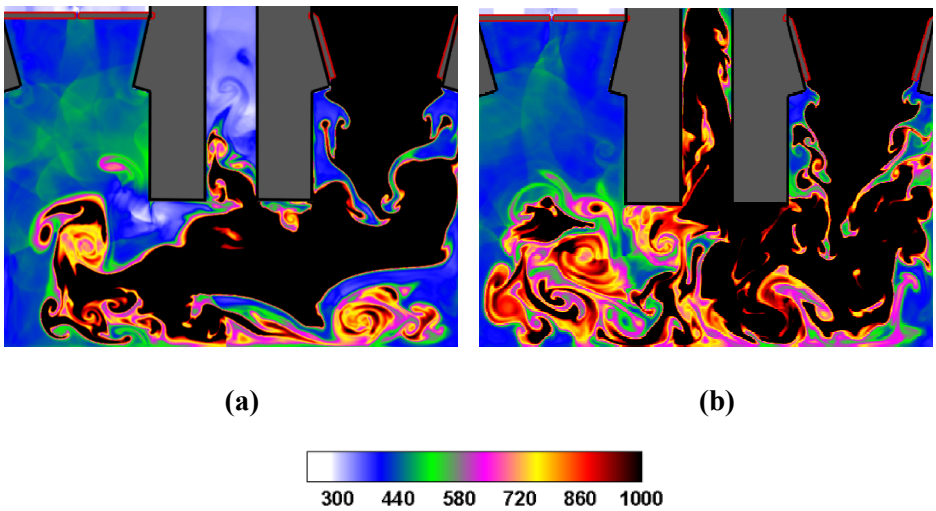

Fig. 4.6. Selective temperature [unit: K] contour of Case II showing hot gas released into a center uptake at (a) 8 ms and (b) 10 ms.

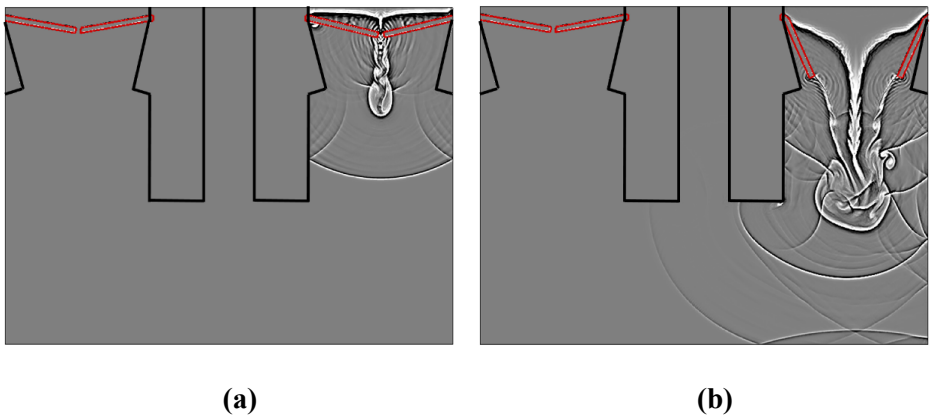

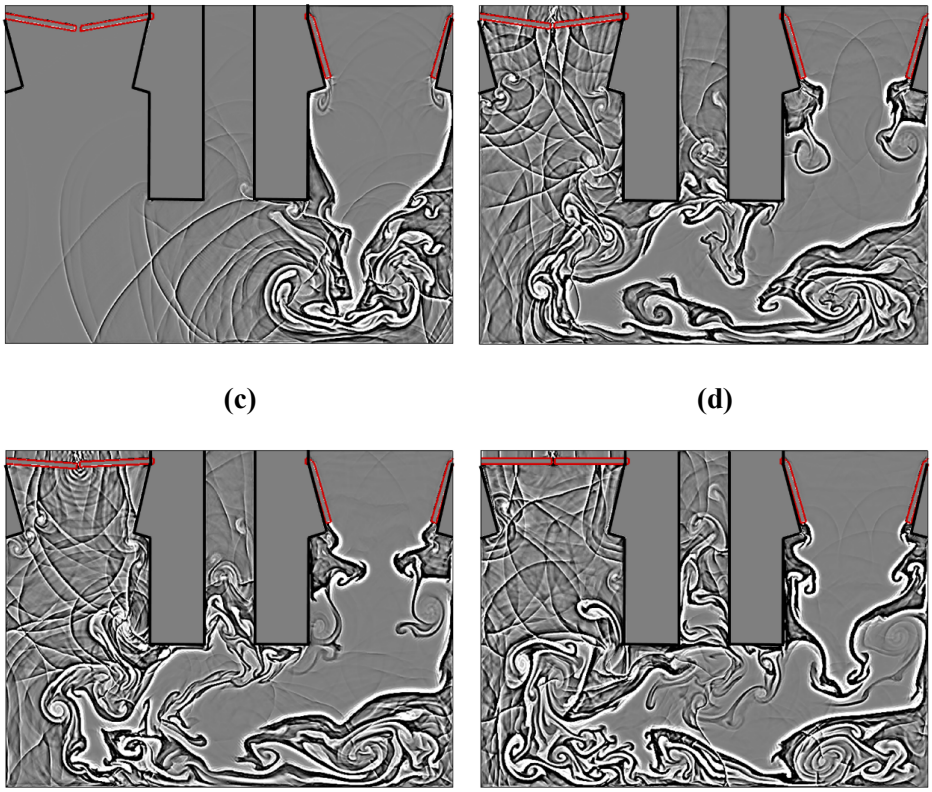

Fig. 4.7. Full simulation shadowgraph of Case II, showing closure of the left canister cover due to high pressure plenum flow at (a) 1 ms, (b) 3 ms, (c) 4.8 ms, (d) 7 ms, (e) 7.4 ms, and (f) 8 ms.

4.3 Conclusion

The severely transient FSI problem, that arises during the operation of vertical launch tubes, was simulate by the developed FSI code. The opening of tube rear covers due to AP propellant burning gases was dynamically

reproduced. The resulting plume that fills the lower plenum was analyzed to understand the hydrodynamic state of the gas filled plenum subjected to the structural motions of the deforming rear covers. The coupled algorithm and its capability to handle strongly coupled multi-material interactions was used to reproduce the hydrodynamic and thermal flow fields inside the plenum during launch tube operation. Future VLS designs that are exposed to unusually harsh interacting fluid and structure conditions can benefit from the results outlined in this work.

Chapter 5. Detonation in Concrete Building

5.1 Background and motivation

A single room explosion experiment for testing the power of a newly developed energetic material was analyzed by using the three-dimensional reactive fluid and structure interaction simulation code. The flow inside a complex geometry such as a concrete building could not be simplified to one or two-dimensional analysis. Therefore, the STL file, as shown in Fig. 5.1, of the concrete building was converted into the same level as Fig. 5.2 and the three-dimensional FSI analysis was performed. The energetic material reaction inside the concrete building was analyzed by the KYP model as shown in Table 5.1. The equation of state (EOS) of unreacted and reacted energetic materials listed in Table 5.2. The detailed composition of the energetic material, the chemical reaction, and EOS formulas are explained in the Ref. [47].

The solid energetic material explosion simulations were analyzed in a small calculation domains such as a rate stick [47-50], PMD [51, 52], and dent test [53] simulations. In these simulations, the physical phenomenon occurring at the boundary between reacted gas and environment was not significant. However, in the large scale (>2 m), shock propagation into the environment is important to analyzed the physics. A method to reconcile air and reacted gas EOS was developed. If the density of the reacted gas is sufficiently low, the calculated pressure by JWL EOS becomes equal to the ideal gas EOS. In this

sense, the shock propagation in the air such as air blast was analyzed.

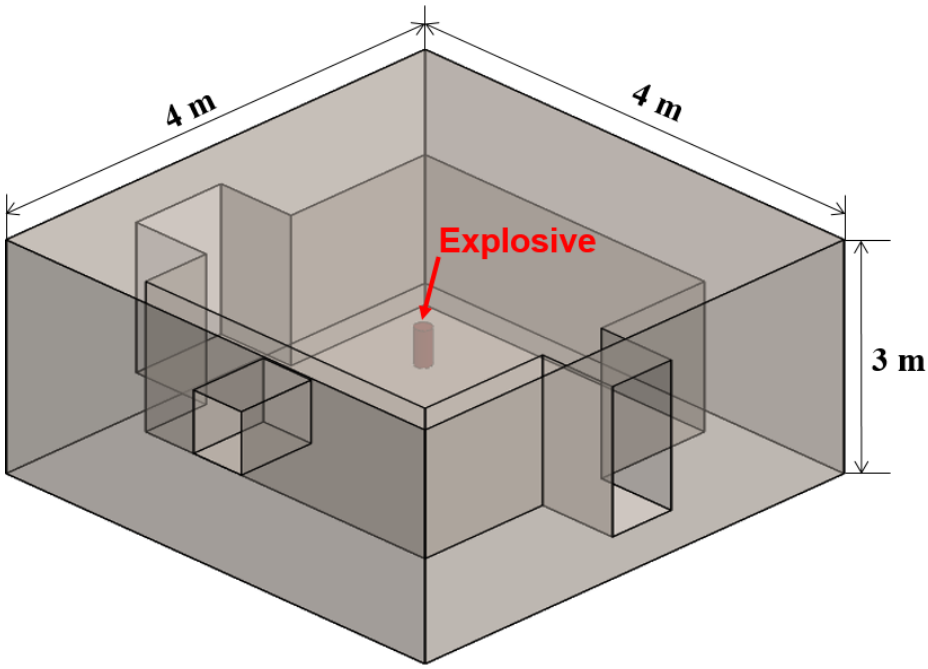

Fig. 5.1 Concrete building geometry described in STL file.

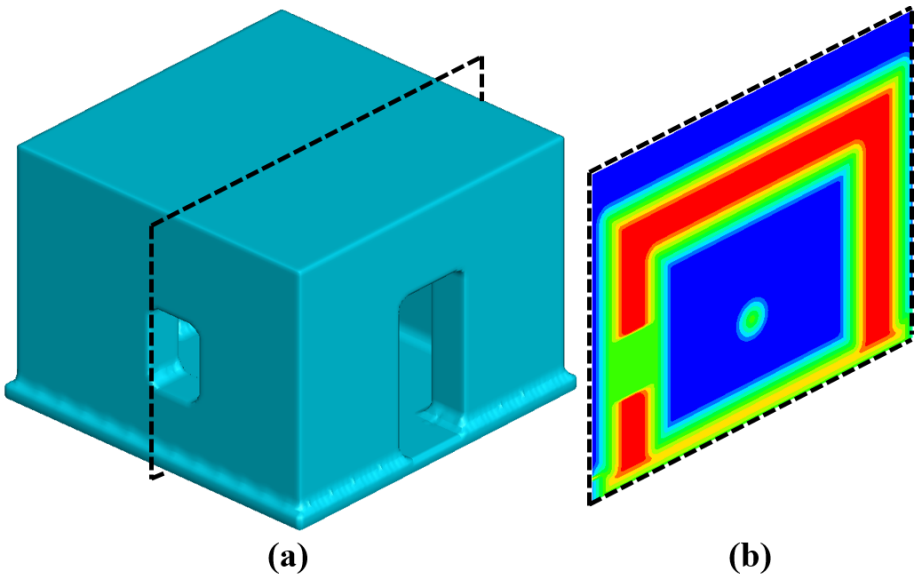

Fig. 5.2. The concrete building geometry converted into the level. (a) is iso-

surface (*level = 0*) and (b) is sliced contour at x = 2 m in Eulerian domain.

Table 5.1 Parameters of ignition model for aluminized explosive [47].

Parameter [unit]	Aluminized explosive [47]
I [μs^{-1}]	12.10
a	4.0
G [$\mu s^{-1} Mbar^{-b}$]	1074.4
b	1.65

Table 5.2 Parameters of the EOS for aluminized explosive [47].

Parameter [unit]	Unreacted JWL EOS	Parameter [unit]	Reacted Mie-gruneisen EOS
A [GPa]	458	C_0 [m/s]	2467
B [GPa]	8.30	S	1.89
R_1	3.72	Γ	1.09
R_2	1.06		
ω	0.359		

5.2 Results and discussion

Due to the explosion of energetic material inside the concrete building, the shock impacts the concrete wall and increases the pressure inside the concrete building Particularly, in the case of explosives containing a large amount of aluminum, a second pick pressure increased by delayed combustion of aluminum. The pressure wave propagation and the pressure transferred by the reflected shock from the concrete walls were shown in Fig. 5.3 through Fig. 5.5. In the figures, the shock waves generated by the explosion are transmitted

to the concrete to increase the pressure inside the concrete, and the reflected shock waves from the wall were superimposed inside the concrete building.

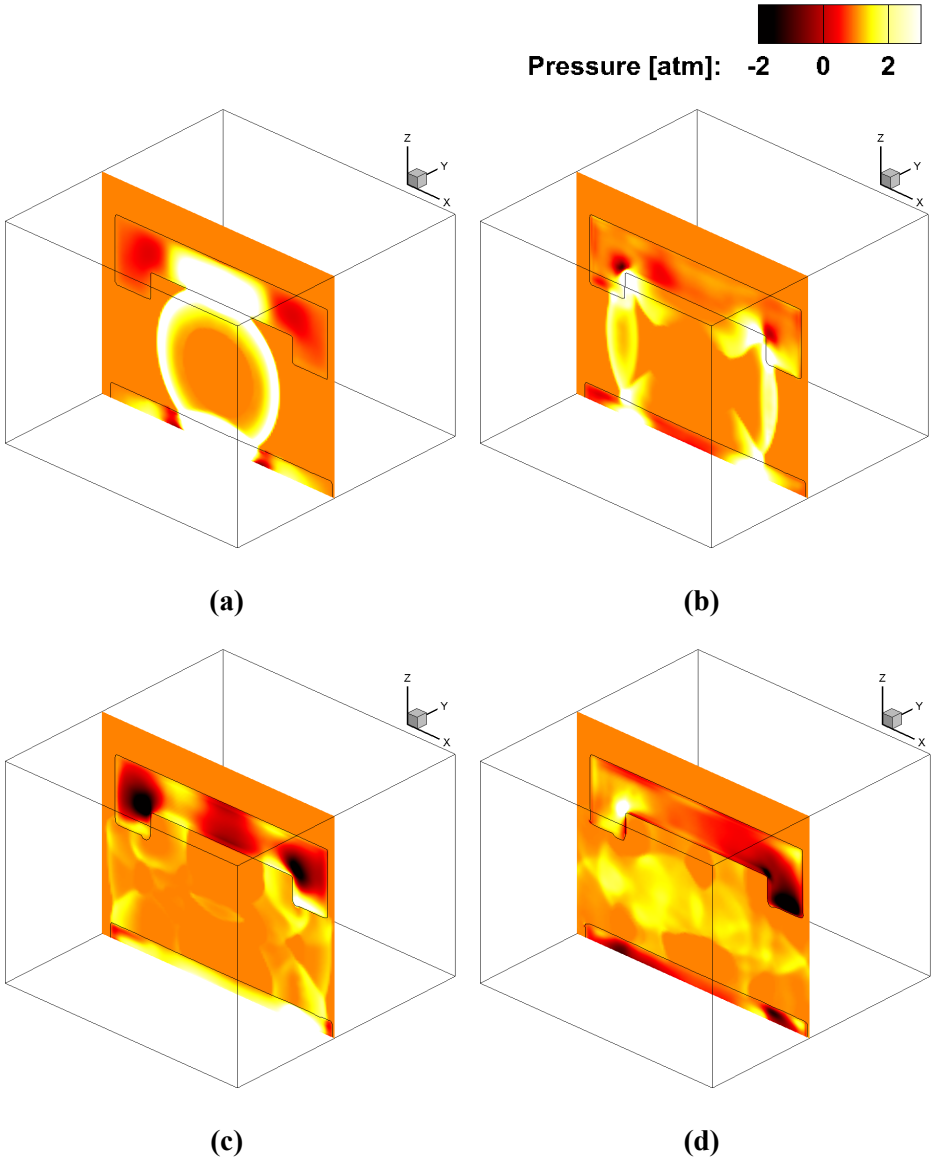

Fig. 5.3. Sliced contour (y = 2 m) of pressure at (a) 1 ms, (b) 2 ms, (c) 3.5 ms, and (d) 5 ms.

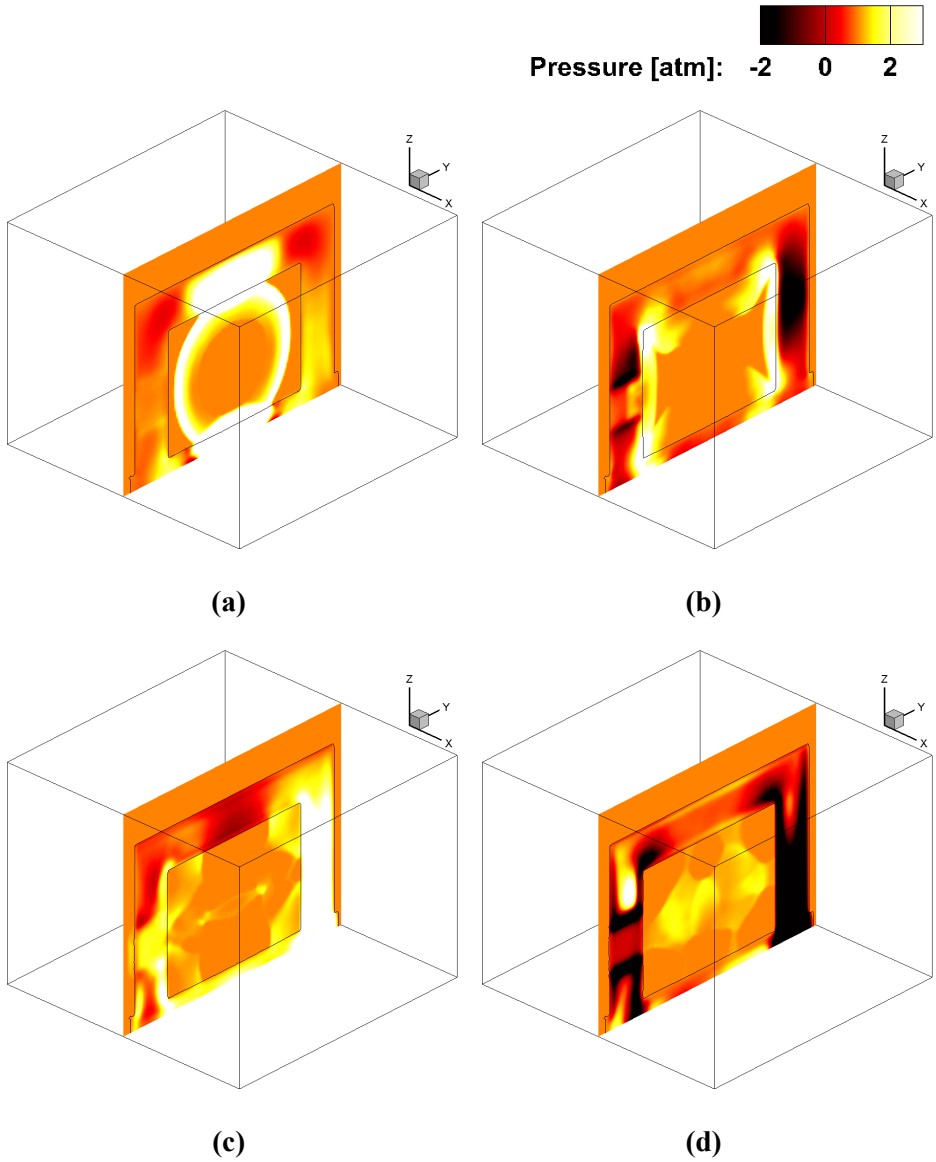

Fig. 5.4. Sliced contour (x = 2 m) of pressure at (a) 1 ms, (b) 2 ms, (c) 3.5 ms, and (d) 5 ms.

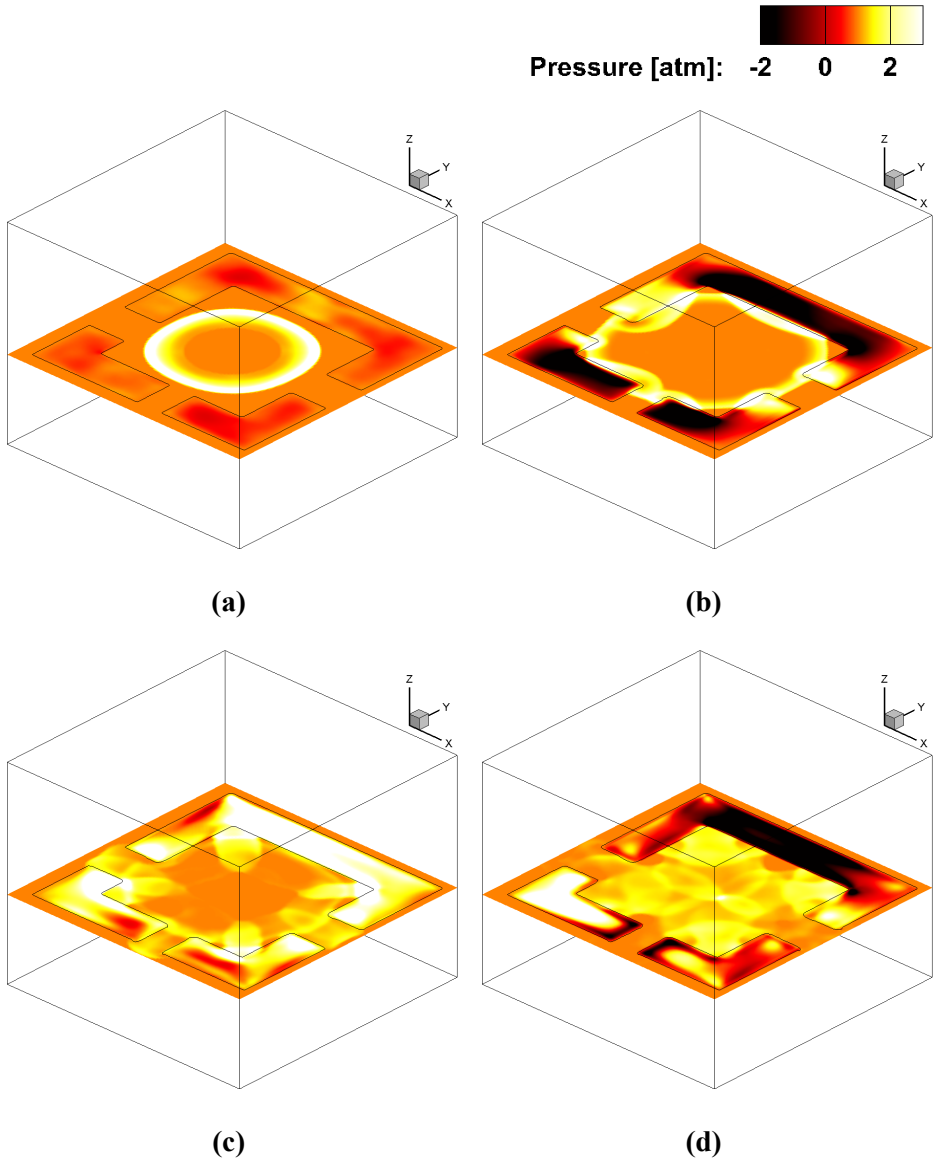

Fig. 5.5. Sliced contour (z = 1.5 m) of pressure at (a) 1 ms, (b) 2 ms, (c) 3.5 ms, and (d) 5 ms.

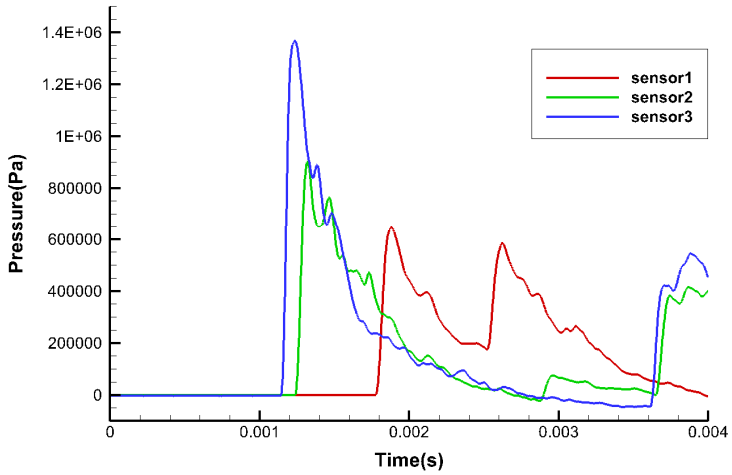

(a)

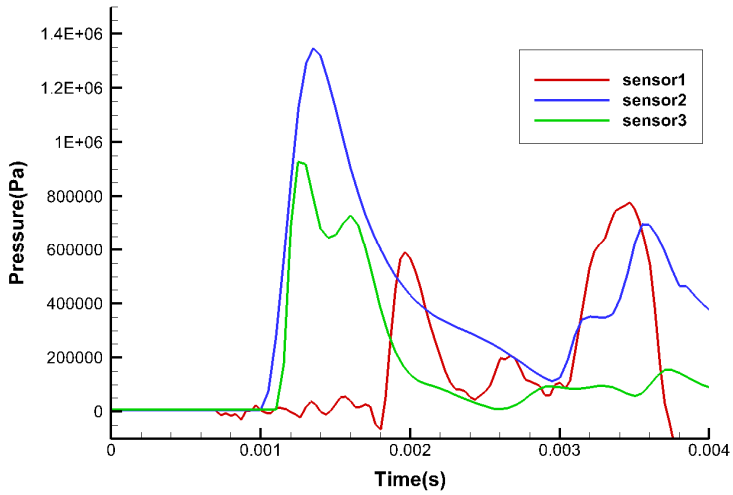

(b)

Fig. 5.6. Pressure history comparison graphs of (a) experiment results and (b) simulation results of

The simulated results were compared with experiments and the comparison is shown in Fig. 5.6. As a results in Fig. 5.7, the pressure is superimposed on

the edge of the inner part of the concrete building, which increases the pressure up to ~6 atm. Through the windows and doors of the concrete building, the shock waves are pulled out as shown in Fig. 5.8.

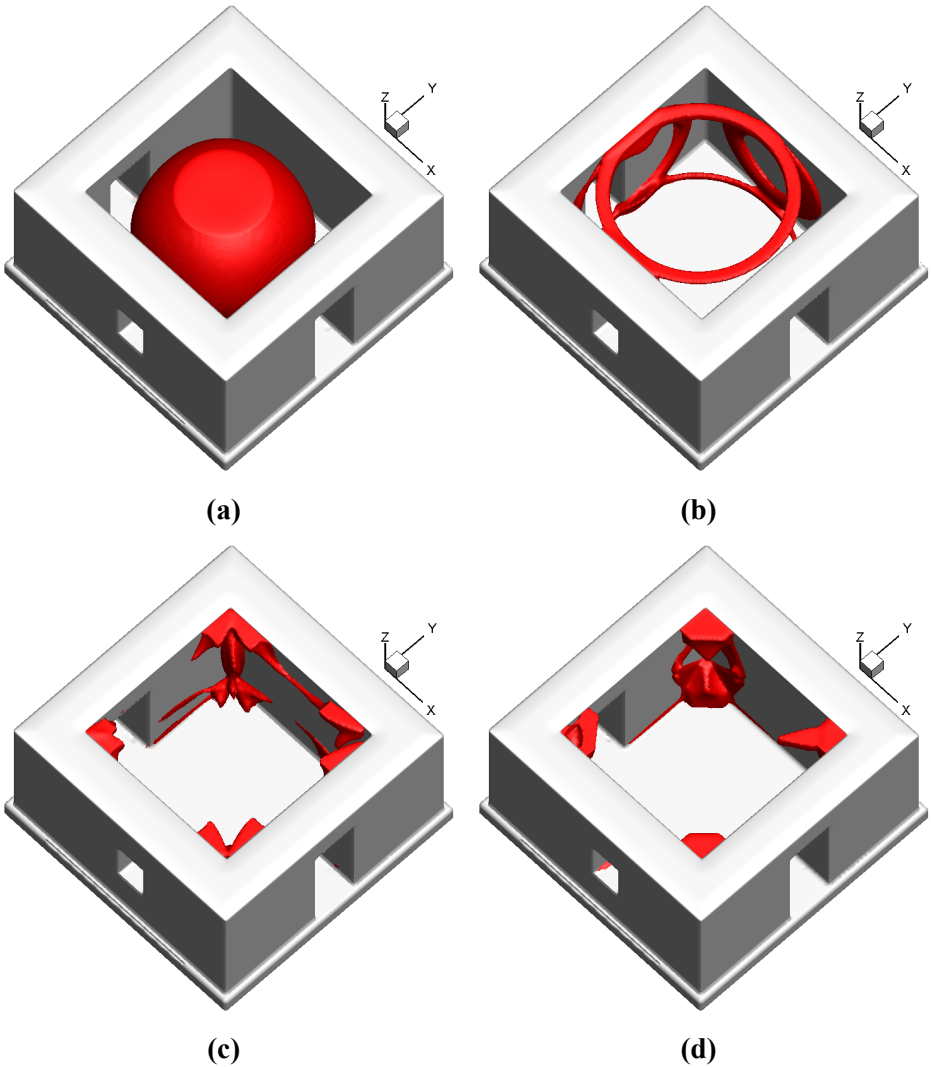

Fig. 5.7. Iso-surface of pressure (p = 3 atm) at (a) 1 ms, (b) 2 ms, (c) 3 ms, and (d) 4 ms.

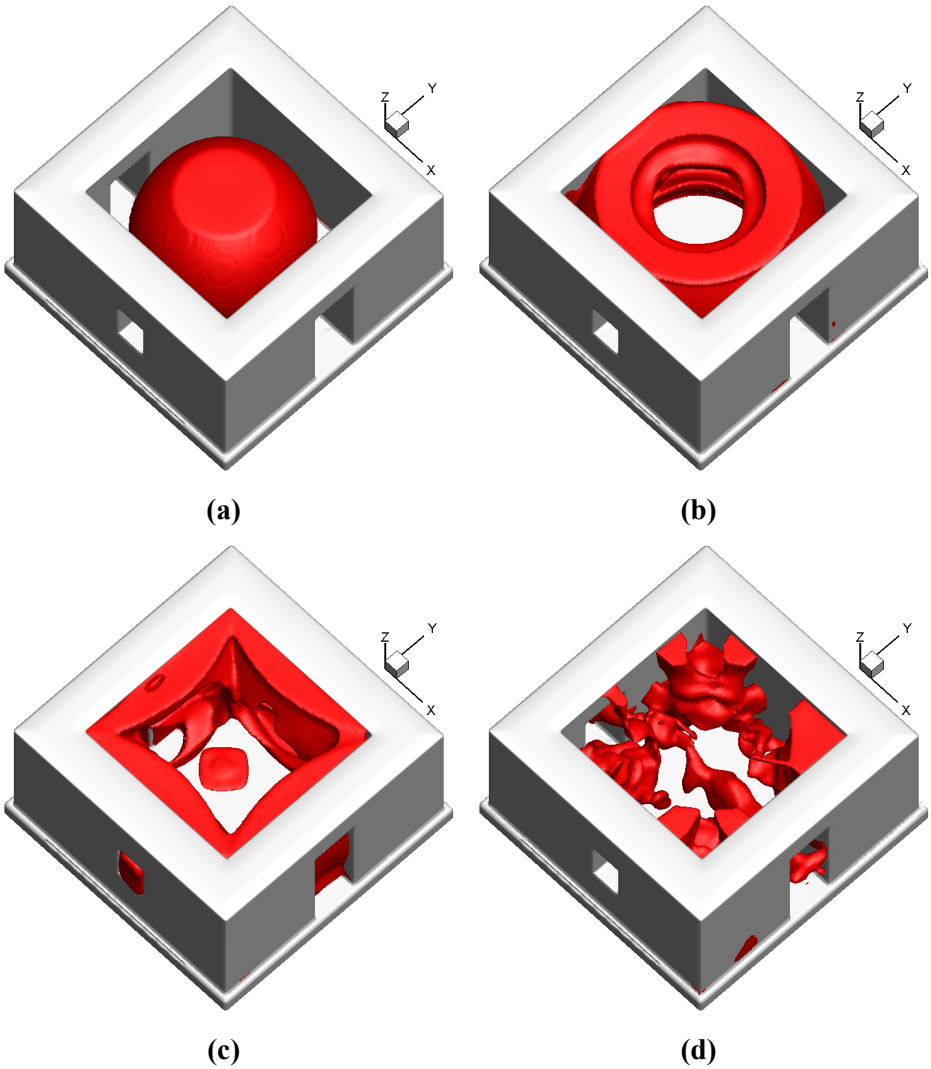

Fig. 5.8. Iso-surface of pressure (p = 1.5 atm) at (a) 1 ms, (b) 2 ms, (c) 3 ms, and (d) 5 ms.

Chapter 6. Detonation in Tube

6.1 Background and motivation

Pulse detonation engine (PDE) uses detonation wave to induce combustion of the fuel and oxidizer. The detonation wave is a shock wave supported by the chemical reaction that results in a higher temperature and pressure than a normal deflagration. Due to its potentially high thermodynamic efficiency attained by the rapid compression of the mixture via the detonation wave at constant volume, there is a considerable volume of literature investigating the performance of such PDE systems [54, 55]. The PDE system has been developed for diverse uses as in ramjet engines and for attitude control in rocket engines. Hydrogen, methane, and kerosene based fuels have been in use for PDE [12, 28, 29, 54-61], and the shock tube experiments [28, 29, 58-61] have been reported for studying reaction properties of these fuels. The kerosene is a compound of many different hydrocarbons, making it extremely challenging to compile a set of realistic chemical kinetics that can precisely describe the reaction response. Instead, a one-step detonation model based on the Arrhenius rate law has been proposed for various fuels [12, 16] and likewise in our research, a simple step reaction model is adapted in tracking the detonation characteristics.

The operation of PDE follows in sequence the detonation ignition, propagation, and reactant refilling. During the detonation propagation, gas temperature can exceed 3000K during a few microseconds of instant wave

propagation. The wall temperature rise during this time is insignificant, and heat transfer at the wall cannot cause wall deformation. However, PDE is operated with multiple pulses of detonation propagation, whose frequency is 10~30 Hz, as the wall is constantly exposed to a harsh thermal conditions [59].

In the section 6.2, the three-dimensional and two-dimensional reactive flow and structure interaction simulation code was verified with experiment results [62]. And in the section 6.3, the numerical simulation of kerosene-air detonation within a thin tube of varying thickness is conducted. In particular, the wall conditions are 1) plastically deforming and 2) temperature varying, to allow thermal softening that may affect the performance of a detonation process. To confirm the thermal softening effect at such harsh temperature conditions, the thermo-plastic response of wall is simulated using the heated wall temperatures ranging from 400 to 1000K. The results are compared with the theoretical values from the dynamic amplification factor and the burst pressure. The heated wall conditions gave rise to thermal softening of the thin-walled tube and subsequent decrease of the yield strength that leads to a rapid plastic deformation of the tube [63]. Furthermore, during PDE operation whose frequency is approximately 100 Hz [64], the PDE could elastically vibrate at its various natural frequencies under both internal and external stimulations. In the previous studies, the detonation tube had been treated as rigid [56, 57], and an elastic vibration may not be a dominant factor of detonation propagation. However, it induces a minutely oscillated wall which ingenerates perturbations of flame in the process of detonation propagation. Considering these circumstances, this study has been proposed.

In the section 6.4, based on a fully Eulerian formulation, the numerical simulation of gaseous mixture detonation within an elasto-plastic steel tube has been conducted by developed FSI code. Here, the detonation reaction model and interface tracking and treatment methods are not mentioned fully in this paper since these has been demonstrated in previous researches [12, 14]. To incorporate dynamic interaction between hydrocarbon detonation and the elasto-plastic tube that influence each other, the tube conditions are set as elasto-plastically deforming and elastically vibrating.

6.2 Validation of detonation-loaded tube

Having completed two representative validation runs, a closer look at elasto-plastic deformation of tube, originated from the detonation loading. A purely plastic deformation of a steel tube under a detonation loading of C_2H_4–O_2 mixture has been investigated previously [12]. Here, we investigate the elasto-plastic deformation of a steel tube as in the same loading condition. Figure 6.1 compares experiment and calculations of the residual strains for an initial condition (2 bar). Purely plastic result seems broader than both experiment and elasto-plastic result. This is because purely plastic model takes into account the liquefied solid phase following a plastic deformation. The three-dimensional and two-dimensional elasto-plastic result seems to reproduce the measurement because the elastic energy and velocity give rise to an elastic recovery after the unloading of detonation.

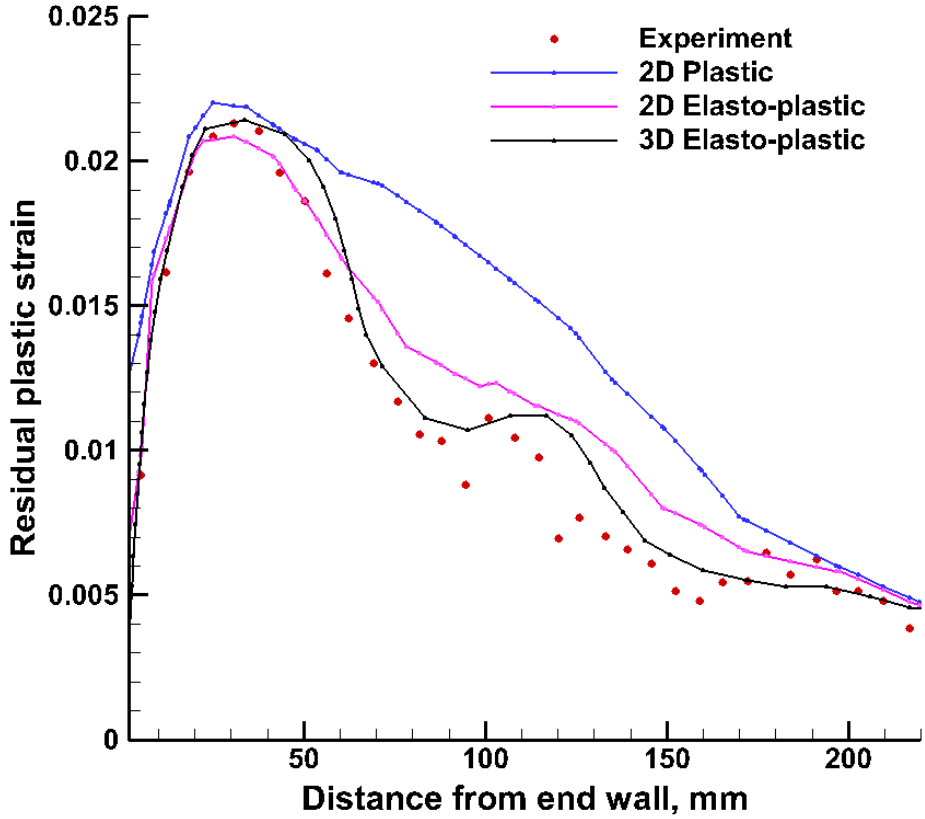

Fig. 6.1. Comparisons of the experiment and calculations of residual plastic strain.

6.3 Detonation-loaded tube

Two-dimensional simulations of plastically deforming copper and 304 stainless steel tubes exposed to the heated wall conditions are considered. In the PDE system, repetitive detonation pulses induce wall temperature to rise which may lead to a change in the structural characteristics of the system. To investigate this potential safety issue in detail, we consider a one-dimensional

heat transfer problem consisting of a hot gas and a copper separated by a wall as shown in Fig. 6.2. In this figure, T_g, T_w, and T_s indicate internal hot gas temperature, heated wall surface temperature, and solid temperature within copper, respectively. The convective heat flux applies at the gas and the wall nodes while the diffusive heat flux is considered only at the inner copper node. The cylindrical Eq. (2.4) is simplified as Eq. (6.1).

$$\rho_w C_{p,w} \frac{\partial T_w}{\partial t} - k \frac{\partial^2 T_w}{\partial r^2} - \varphi q_{conv} = 0 \tag{6.1}$$

where parameters $\varphi = 0$ is for the copper node and $\varphi = 1$ for the wall node. ρ_w, $C_{p,w}$, and q_{conv} are the density, specific heat and convection heat flux at the wall node, respectively. Here, the wall boundary is exposed to multiple detonation pulses during the operation of a PDE, and the convective heat flux at the boundary is given by Eq. (6.2) [65].

$$q_{conv} = C_f \rho_g |u_g| C_{p,g} \left(T_g \left(1 + \frac{\gamma_g - 1}{2} M_g^2 \right) - T_w \right) / 2 \tag{6.2}$$

where T_g, T_w, γ_g, M_g, C_f, ρ_g, and u_g are gas temperature, wall temperature, gas specific heat ratio, gas Mach number, friction coefficient, gas density, and gas velocity, respectively. One notices that the gaseous states are determined from solving the kerosene-air detonation problem, and they are depicted in Fig. 6.3. The frequency range of each detonation pulses of 10 to 30 Hz is considered.

By solving Eq. (6.1), the change of T_w under different operating frequencies in a PDE system using a kerosene-air mixture detonation is obtained as shown in Figure 6.4. Here the comparison between calculation and experiments [59]

is shown. T_w is heated from the ambident temperature to 1000 K as such the high temperature wall (above 873 K) may act as a catalyst during gaseous reaction [66].

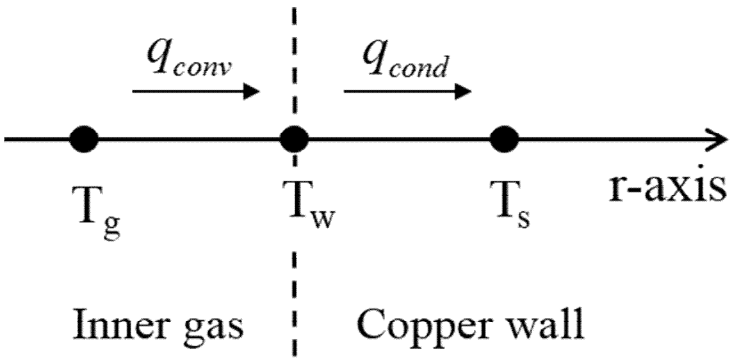

Fig. 6.2. Schematic of wall heating analysis.

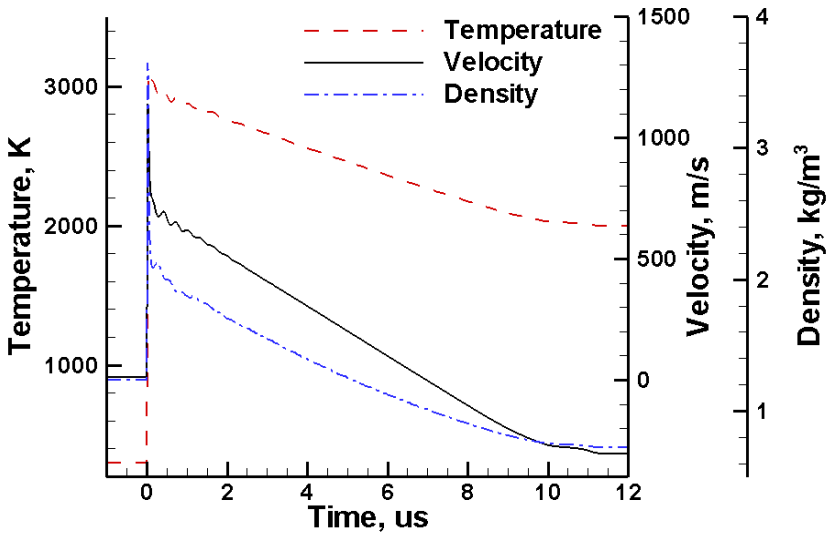

Fig. 6.3. Histories of temperature, velocity, and density during ignition and propagation of a detonation.

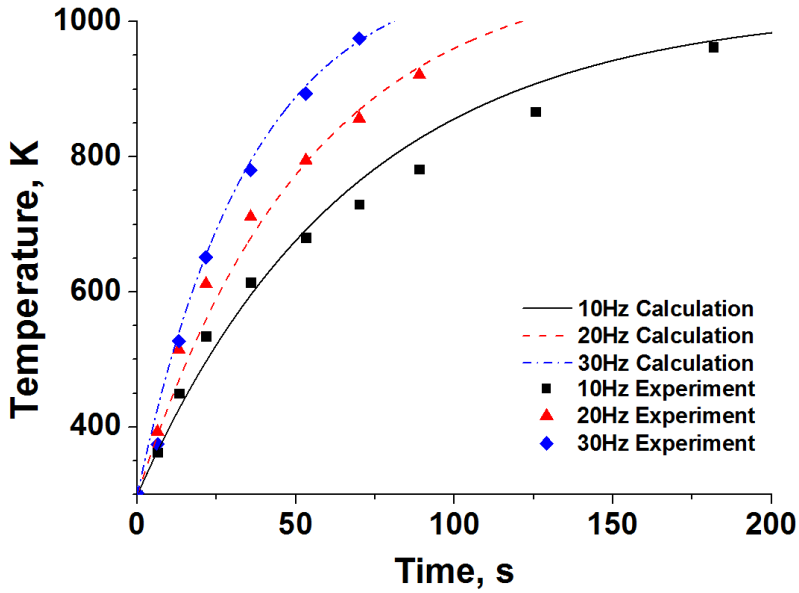

Fig. 6.4. Experimental [59] and numerical wall temperature history under different operating frequencies.

Since copper is an inert material, there should be no affect in the mixture reaction. However at such elevated wall temperature conditions, thermal softening plays a signicant role that gives rise to a change in the metal properties and its thermal stresses. Four different wall temperatures (T_w= 433 K, 573 K, 773 K, and 973 K) are considered for investigating the heated wall effect on the resulting full dynamics of the considered tube loading problem. The considered tube thicknesses for copper tube are 0.15, 0.2, 0.25, 0.3, 0.35, 0.4 and 0.45 mm. As for 304 stainless steel tube, they are 0.05, 0.08, and 0.12mm. All tubes have the same inner radius r_i = 2 mm. The two-dimensional cylindrical domain is depicted in Fig. 6.5 with its cross section (4

mm by 30 mm) shown with a varying tube thickness, t. The boundary conditions on the left, right, top, and bottom are symmetric, zero gradient, zero gradient, and extrapolated $Y_{boundary} = 0.95Y_1+0.05Y_0$, respectively. For initiating a detonation, the CJ values initialize the bottom condition.

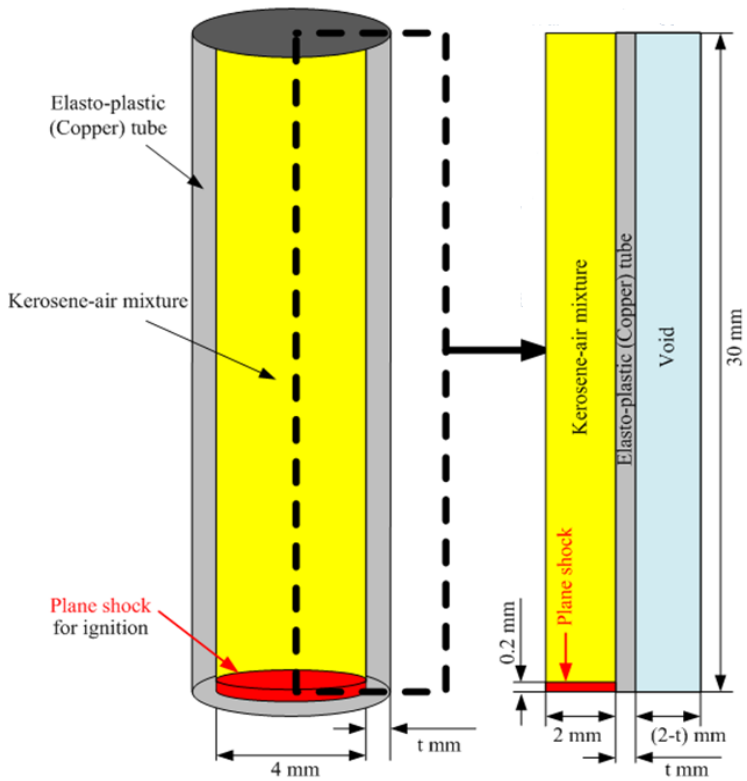

Fig. 6.5. Schematic of detonation-loaded copper and 304 stainless steel tubes

The theory on dynamic amplification factor (DAF), Φ and critical burst pressure, P_{burst} for plastic deformation of thin tube under detonation loading is first considered. DAF is a ratio between the maximum dynamic strain

$\varepsilon_{dynamic,max}$ and the static strain ε_{static} [67]. The critical burst pressure could provide a theoretical critical thickness of tube under kerosene mixture detonation loading, and the thickness is compared with the simulation result.

In Fig. 6.6, DAF for copper is 2.03, and it is 2.02 for 304 stainless steel, which are obtained from the kerosene-air mixture detonation velocity of 1750 m/s. As for the thin tube, the corresponding burst pressure [67] is given by the expression below:

$$p_{burst} \approx \sigma_y \left[1 - \left(\frac{T - T_0}{T_m - T_0} \right)^{1.09} \right] \frac{t}{\Phi\left(r_i + t/2\right)} \tag{6.3}$$

where, T, T_m, T_0, t, r_i, and σ_y are the wall temperature, the melting temperature, the reference temperature (293 K), the tube thickness, the inner radius, and yield stress, respectively. The above equation gives the approximated pressure upon the onset of a plastic deformation. The yield strength of copper tube changes by the thermal softening effect. From this equation, a critical thickness of copper tube is determined from a burst pressure or the detonation pressure of kerosene-air mixture approximately 1.5 MPa. Stainless steel has higher yield strength and melting temperature, thus 0.12 mm wall thickness is considered rigid even in the hot region. However copper tube can deform easily and such interesting observations are noted at high temperature cases.

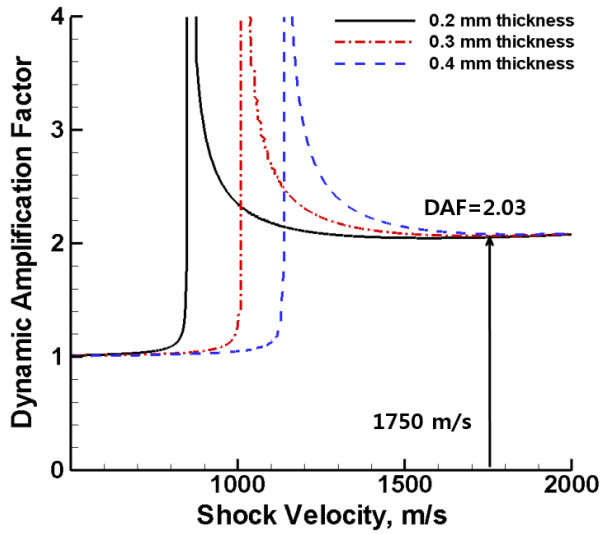

(a)

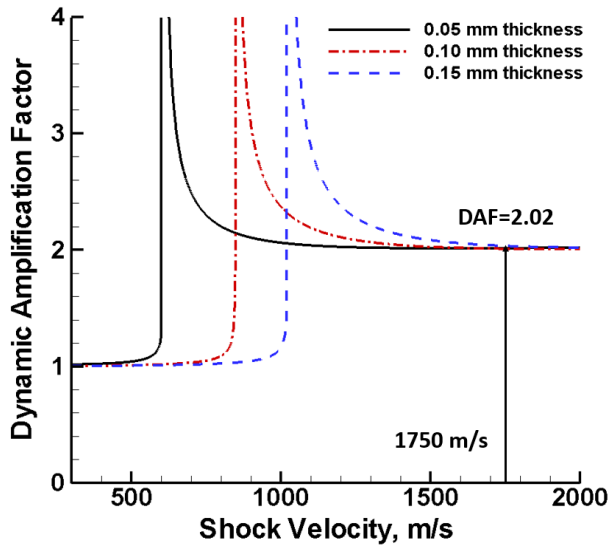

(b)

Fig. 6.6. DAF versus velocity of varying (a) copper and (b) 304 stainless steel tube thicknesses.

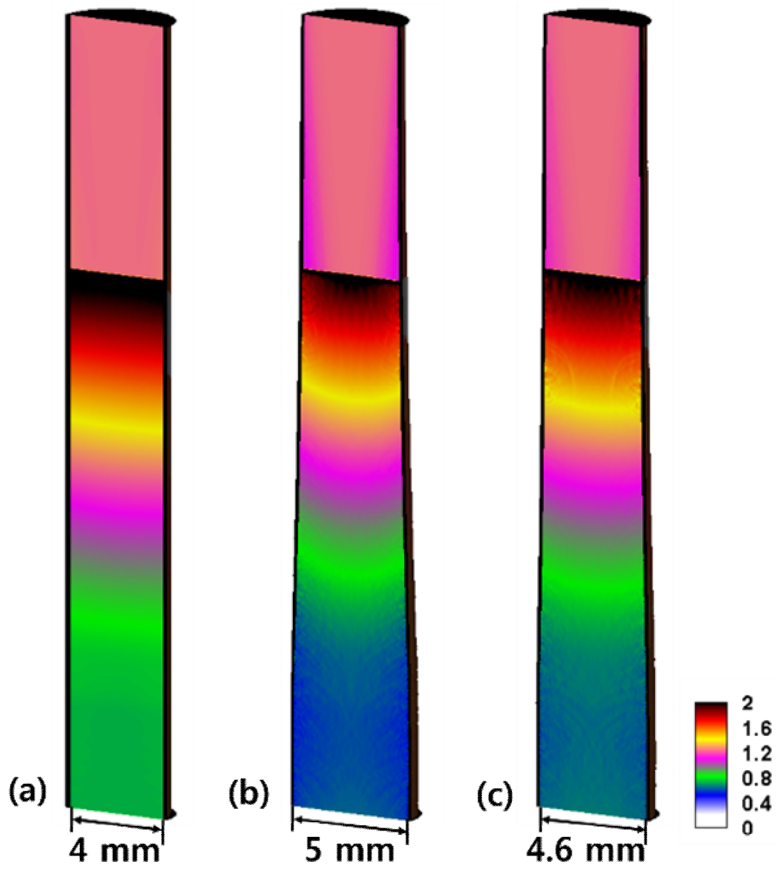

Fig. 6.7. Snapshots of density [unit: kg/m3] in (a): Tw= 433 K, t= 0.2 mm, (b): Tw= 433 K, t= 0.15 mm, and (c) Tw= 973 K, t= 0.15 mm, all of which taken at 11.5 μs without thermal softening.

To point out the errors in making predictions on wall expansion when thermal softening is not considered, Fig. 6.7 is shown with the density for 0.2 and 0.15 mm thickness tubes under 433 K and 973 K wall conditions. There is no deformation for 0.2 mm case. As for 0.15 mm case for both cold

and hot walls, the effective plastic stress exceeds the tube yield stress and thus the tube expansion is expected. The unreacted flow ahead of the detonation wave is affected by the tube expansion since the stress wave propagation within the solid is faster than a gaseous detonation velocity. The r-axis deviatoric stress, s_{rr} of the cold case (b) is approximately twice larger than the hot case (c) since the yield stress is inversely proportional to a temperature. Subsequently the expanding wall speed of cold case is approximately twice faster than the hot case of 973 K.

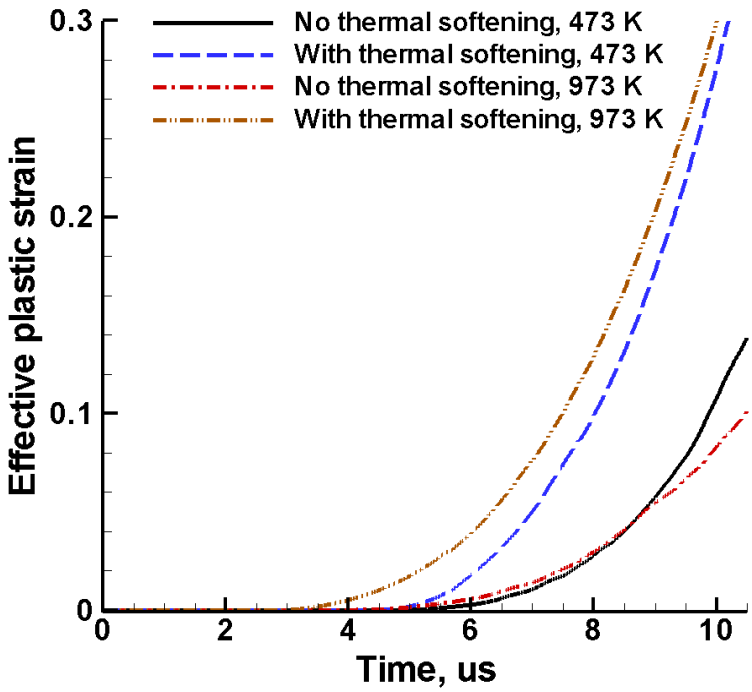

Fig. 6.8. Effect of thermal softening plotted with effective plastic strains at cold (433 K) and hot (973 K) wall temperature conditions

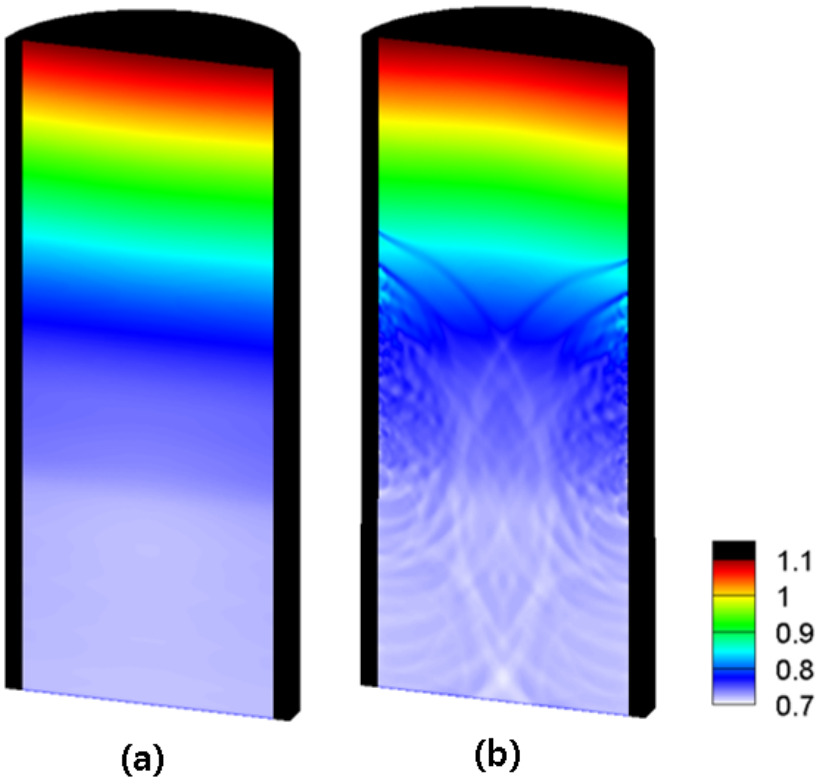

Fig. 6.9. Snapshots of density [unit: kg/m3] in two cases of (a) no thermal softening and (b) with thermal softening under Tw= 773 K and t= 0.25 mm tube at 10 μ.

This is rather unphysical, suggesting that one must include thermal softening in the analysis. Now, with thermal softening included, the thermal stress states change readily, in particular with the rising temperature of the tube such that more wall expansion is expected for the higher temperature wall condition (see Fig. 6.8). In Fig. 6.9, the comparison between (a) without and (b) with thermal softening under the condition, T_w= 773 K and t= 0.25 mm is shown. The tube undergoes minute deformation with multiple

expansion and compression waves that interfere with the internal detonation flow structure. Figure 6.7 shows a safety or failure plot that describes the effect of thermal softening when it comes to providing the prediction of tube responses subjected to an internal detonation loading. The critical thickness from theory shown as a solid line is obtained from Eq. (6.3). Although the hottest temperature region falls short of the theory prediction near the melting temperature of copper, the overall critical thickness is in excellent agreement with the theoretical values. Therefore, the inclusion of thermal softening is critical for a reliable numerical simulation of the tube wall expansion subjected to an internal gaseous detonation loading.

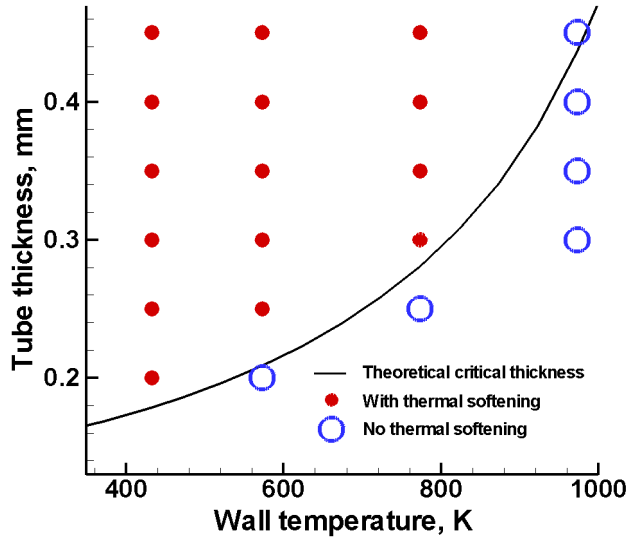

(a) Copper

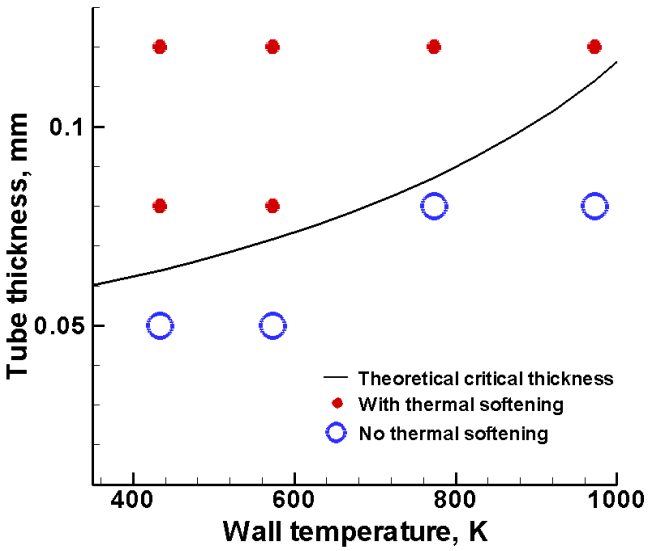

(b) 304 Stainless steel

Fig. 6.10. The calculated (symbol) and theoretical (solid line) critical thickness plotted against heated wall temperature for (a) Copper and (b) 304 Stainless steel

6.4 Detonation in the elastic vibrating steel tube

Figure 6.8 depicts two-dimensional section of the tube (4 mm x 30 mm) shown with a thickness, t= 0.2 mm. The boundary conditions on the bottom, top, right, and left are symmetric, zero gradient, zero gradient, and extrapolated $Y_{boundary} = 0.95Y_1+0.05Y_0$, respectively. For initiating a detonation, the C-J values are prescribed at the inlet as a plane shock wave. The propagation of kerosene-air mixture detonation [12] under vibrating tube with natural frequency is considered. The natural frequency of the tube shown in Fig. 13 is ~31 kHz (the first longitudinal mode and the second radial wave mode), as previously obtained from the Rayleigh method. Thus, we consider a vibrating steel tube at frequency of 31 kHz with three different maximum strain of 0.000125 and 0.00025 which come within the elastic strain range.

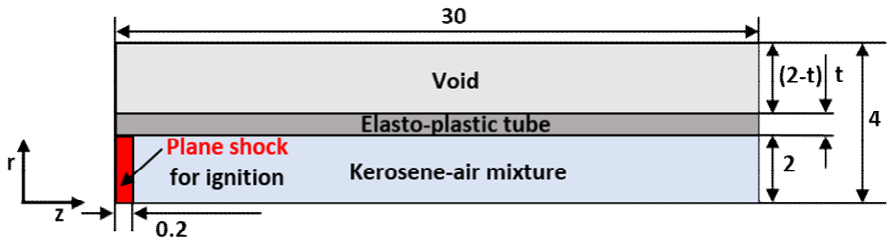

Fig. 6.11. Schematic of kerosene-air detonation tube (unit: mm).

Figure 6.9 shows the pressure histories of detonation for rigid tube and strong/weak vibrating tubes along the center line. Although the detonation velocity for these tubes are measured the same, the pressure for vibrating

tube fluctuated more. And the perturbation of detonation is increased in accordance with increase of maximum strain. Said differently, the elastic vibration of tube disturbs the detonation front as the development of small radial velocities and the formation of pressure gradients along the wall give rise to the strong enhancement of the acoustic wave interaction.

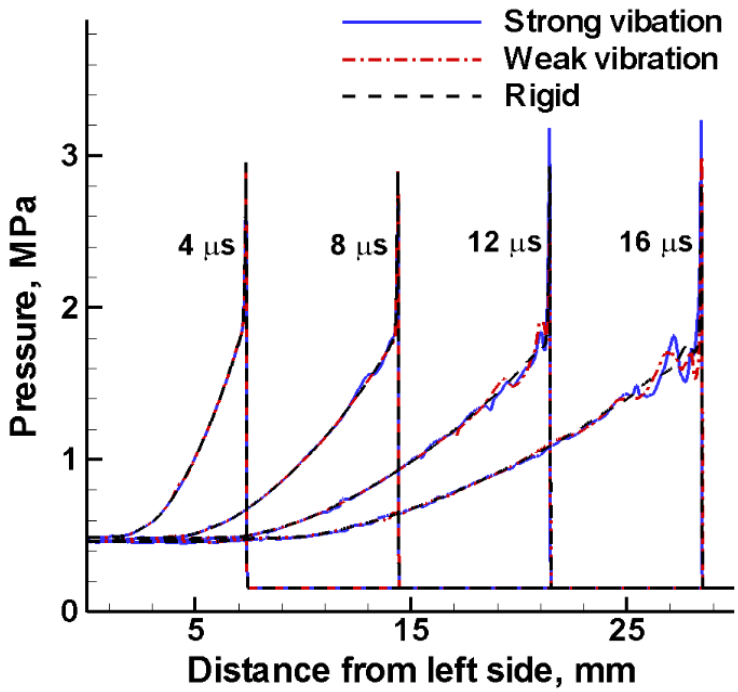

Fig. 6.12. Pressure histories of detonation in the rigid, week vibrating (ε_{max}=0.000125), and strong vibrating (ε_{max}=0.00025) tubes.

These are consistent with the findings represented in Fig. 6.10 which shows the density contour in rigid and strong elastic vibrating tubes at 8 and 14 μs. In the elastic vibrating tubes, the flow field is disturbed, and winding detonation front and acoustic waves in the burned region are appeared.

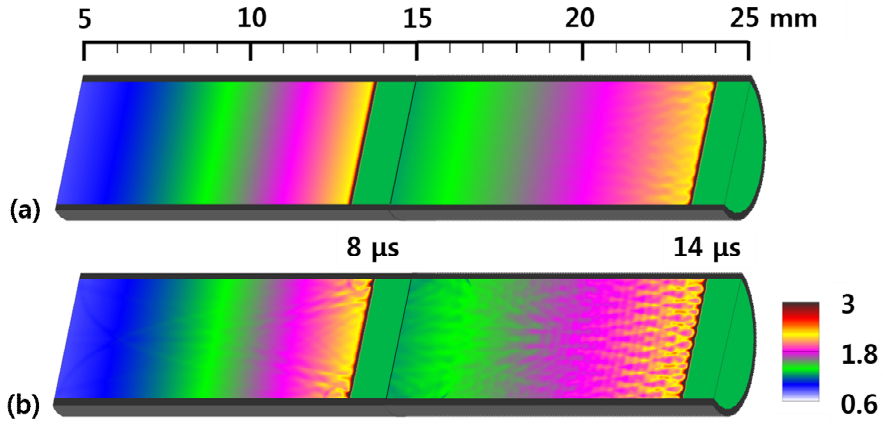

Fig. 6.13. Snapshots of density [unit: kg/m3] at times 8 and 14 µs for (a) rigid wall and (b) strong elastic vibrating tubes.

Chapter 7. Conclusion

In this study, various reactive flows were considered. The ethylene-air mixture and the kerosene-air mixture, which are gaseous high energy materials, simulate the combustion reaction through the 1-step Arrhenius equation. In addition, combustion characteristics of anisotropic PETN and HMX, which are solid energetic materials, were analyzed by using the modified anisotropic I&G model. The developed combustion model compared the C-J condition and the detonation cell size. Structure deformation was performed by using Eulerian or Lagrangian analysis method and the method was verified by comparing with the experimental data of Taylor impact problem. We used a level set technique and a ghost fluid method (GFM) to set boundary values and trace the interface between the reactive flow and the structure. In order to verify the multi-material analysis method, the cantilever motion in the flow field and the tube deformation problem due to detonation load were simulated. The numerical results are verified by comparing with the theoretical and experimental values. For the three dimensional simulation, the STL file to level converting algorithm was developed. Moreover, the adaptive mesh refinement (AMR) and message passing interface (MPI) for parallel processing were conducted to reduce the computation time and resources.

Based on the developed code, we have analyzed the interactions between reactive flow and structure under various thermal hydrodynamic loading systems. The behavior of rear cover which is deformed by the launching

rocket plume inside a vertical launching system (VLS) is analyzed. This analysis results were verified by comparing with the experimental data, and the influence of rear cover deformation on the flow was confirmed through the analysis results. In addition, the explosion of the solid explosives in the three-dimensional concrete building, which cannot be simplified in two dimensions, and the pressure transmitted to the wall are analyzed. The numerical analysis results were compared with experimental data. In the analysis of tube deformation due to detonation inside the metal tube was simulated. The yield stress of metal tube is dependent on wall temperature and thermal softening was considered. In case of Pulse Detonation Engine (PDE), which is exposed to high temperature environment, accurate results can be obtained by using temperature dependent properties and simulation results verified by comparison with theoretical failure model. And we consider the elastically vibrating tube for detonation inside the PDE simulation. Due to the repetitively detonation propagation inside PDE, the PDE wall is vibrated with its natural frequency even if the PDE does not be destroyed. The simulation results confirms that propagation of detonation is affected by the deformation of tube.

References

[1] W. C. de Jesus, A. M. Roma, M. R. Pivello, M. M. Villar, and A. da Silveira-Neto, “A 3D front-tracking approach for simulation of a two-phase fluid with insoluble surfactant,” *Journal of Computational Physics,* vol. 281, pp. 403-420, 2015.

[2] S. K. Sambasivan, M. J. Shashkov, and D. E. Burton, “A cell-centered Lagrangian finite volume approach for computing elasto-plastic response of solids in cylindrical axisymmetric geometries,” *Journal of Computational Physics,* vol. 237, pp. 251-288, 2013.

[3] M. h. Souli, A. Ouahsine, and L. Lewin, “ALE formulation for fluid–structure interaction problems,” *Computer methods in applied mechanics engineering,* vol. 190, no. 5-7, pp. 659-675, 2000.

[4] R. P. Fedkiw, “Coupling an Eulerian fluid calculation to a Lagrangian solid calculation with the ghost fluid method,” *Journal of Computational Physics,* vol. 175, no. 1, pp. 200-224, 2002.

[5] M. Arienti, P. Hung, E. Morano, and J. E. Shepherd, “A level set approach to Eulerian–Lagrangian coupling,” *Journal of Computational Physics,* vol. 185, no. 1, pp. 213-251, 2003.

[6] F. Cirak, and R. Radovitzky, “A Lagrangian–Eulerian shell–fluid coupling algorithm based on level sets,” *Computers Structures,* vol. 83, no. 6-7, pp. 491-498, 2005.

[7] G.-H. Cottet, E. Maitre, and T. Milcent, “Eulerian formulation and level set models for incompressible fluid-structure interaction,” *ESAIM: Mathematical Modelling Numerical*

Analysis, vol. 42, no. 3, pp. 471-492, 2008.

[8] J. H. Seo, and R. Mittal, "A sharp-interface immersed boundary method with improved mass conservation and reduced spurious pressure oscillations," *Journal of Computational Physics,* vol. 230, no. 19, pp. 7347-7363, 2011.

[9] V. Lakshminarayan, C. Farhat, and A. Main, "An embedded boundary framework for compressible turbulent flow and fluid–structure computations on structured and unstructured grids," *International Journal for Numerical Methods in Fluids,* vol. 76, no. 6, pp. 366-395, 2014.

[10] Z. Chen, Z. Wu, and Y. Xiao, "AN ADAPTIVE IMMERSED FINITE ELEMENT METHOD WITH ARBITRARY LAGRANGIAN-EULERIAN SCHEME FOR PARABOLIC EQUATIONS IN TIME VARIABLE DOMAINS," *International Journal of Numerical Analysis Modeling,* vol. 12, no. 3, 2015.

[11] M.-c. Gwak, Y. Lee, K.-h. Kim, H. Cho, S. J. Shin, and J. J. Yoh, "All Eulerian method of computing elastic response of explosively pressurised metal tube," *Combustion Theory Modelling,* vol. 21, no. 2, pp. 293-308, 2017.

[12] M.-c. Gwak, Y. Lee, K.-h. Kim, and J. J. Yoh, "Deformable wall effects on the detonation of combustible gas mixture in a thin-walled tube," *International Journal of Hydrogen Energy,* vol. 40, no. 7, pp. 3006-3014, 2015.

[13] C. M. Tarver, R. D. Breithaupt, and J. W. Kury, "Detonation waves in pentaerythritol tetranitrate," *Journal of applied physics,* vol. 81, no. 11, pp. 7193-7202, 1997.

[14] K.-H. Kim, and J. J. Yoh, "A particle level-set based Eulerian method for multi-material detonation simulation of high explosive and metal confinements," *Proceedings of the*

Combustion Institute, vol. 34, no. 2, pp. 2025-2033, 2013.

[15] Y. Lee, W.-H. Lee, M.-c. Gwak, K. Kim, and J. J. Yoh, "A reactive flow simulation for the anisotropic ignition of an explosive crystal using adaptive mesh refinement," *Journal of Applied Physics,* vol. 124, no. 14, pp. 145903, 2018.

[16] E. S. Oran, and V. N. Gamezo, "Origins of the deflagration-to-detonation transition in gas-phase combustion," *Combustion Flame,* vol. 148, no. 1-2, pp. 4-47, 2007.

[17] H. Udaykumar, L. Tran, D. Belk, and K. Vanden, "An Eulerian method for computation of multimaterial impact with ENO shock-capturing and sharp interfaces," *Journal of Computational Physics,* vol. 186, no. 1, pp. 136-177, 2003.

[18] A. Kapahi, S. Sambasivan, and H. Udaykumar, "A three-dimensional sharp interface Cartesian grid method for solving high speed multi-material impact, penetration and fragmentation problems," *Journal of Computational Physics,* vol. 241, pp. 308-332, 2013.

[19] M. A. Bhatti, *Fundamental finite element analysis and applications: with Mathematica and Matlab computations*: John Wiley Hoboken, NJ, 2005.

[20] E. A. de Souza Neto, D. Peric, and D. R. Owen, *Computational methods for plasticity: theory and applications*: John Wiley & Sons, 2011.

[21] K.-H. Kim, M.-c. Gwak, and J. J. Yoh, "An enhanced particle reseeding algorithm for the hybrid particle level set method in compressible flows," *Journal of Scientific Computing,* vol. 65, no. 1, pp. 431-453, 2015.

[22] J. Moreno, "An invitation to plane topology," *AUSTRALIAN MATHEMATICAL SOCIETY GAZETTE,* vol. 29, no. 3, pp. 149-154, 2002.

[23] X. Y. Hu, and B. C. Khoo, “An interface interaction method for compressible multifluids,” *Journal of Computational Physics,* vol. 198, no. 1, pp. 35-64, 2004.

[24] M. J. Berger, and J. Oliger, “Adaptive mesh refinement for hyperbolic partial differential equations,” *Journal of computational Physics,* vol. 53, no. 3, pp. 484-512, 1984.

[25] J. Bell, M. Berger, J. Saltzman, and M. Welcome, “Three-dimensional adaptive mesh refinement for hyperbolic conservation laws,” *SIAM Journal on Scientific Computing,* vol. 15, no. 1, pp. 127-138, 1994.

[26] E. Schnetter, S. H. Hawley, and I. Hawke, “Evolutions in 3D numerical relativity using fixed mesh refinement,” *Classical Quantum Gravity,* vol. 21, no. 6, pp. 1465, 2004.

[27] M. Van Dyke, "An Album of Fluid Motion: Assembled by Milton Van Dyke," The Parabolic Press Stanford, 1982.

[28] Y. Huang, H. Tang, J. Li, and C. Zhang, “Studies of DDT enhancement approaches for kerosene-fueled small-scale pulse detonation engines applications,” *Shock waves,* vol. 22, no. 6, pp. 615-625, 2012.

[29] H. Shen, G. Wang, K. Liu, and D. Zhang, “Numerical simulation of liquid-fueled detonations by an Eulerian–Lagrangian model,” *International Journal of Nonlinear Sciences Numerical Simulation,* vol. 13, no. 2, pp. 177-188, 2012.

[30] R. Akbar, P. Thibault, P. Harris, L. Lussier, F. Zhang, S. Murray, and K. Gerrard, "Detonation properties of unsensitized and sensitized JP-10 and Jet-A fuels in air for pulse detonation engines." p. 3592.

[31] E. L. Lee, and C. M. Tarver, “Phenomenological model of shock initiation in heterogeneous explosives,” *The Physics of*

Fluids, vol. 23, no. 12, pp. 2362-2372, 1980.

[32] J. Dick, R. Mulford, W. Spencer, D. Pettit, E. Garcia, and D. Shaw, "Shock response of pentaerythritol tetranitrate single crystals," *Journal of applied physics,* vol. 70, no. 7, pp. 3572-3587, 1991.

[33] J. Dick, "Anomalous shock initiation of detonation in pentaerythritol tetranitrate crystals," *Journal of applied physics,* vol. 81, no. 2, pp. 601-612, 1997.

[34] J. F. Baytos, *LASL explosive property data*: Univ of California Press, 1980.

[35] C. Yoo, N. Holmes, P. Souers, C. Wu, F. Ree, and J. Dick, "Anisotropic shock sensitivity and detonation temperature of pentaerythritol tetranitrate single crystal," *Journal of Applied Physics,* vol. 88, no. 1, pp. 70-75, 2000.

[36] K.-H. Kim, L. E. Fried, and J. J. Yoh, "Understanding the anisotropic initiation sensitivity of shocked pentaerythritol tetranitrate single crystals," *Applied Physics Letters,* vol. 103, no. 13, pp. 131912, 2013.

[37] J. House, B. Aref, J. Foster Jr, and P. Gillis, "Film data reduction from Taylor impact tests," *The Journal of Strain Analysis for Engineering Design,* vol. 34, no. 5, pp. 337-345, 1999.

[38] E. Vitali, and D. J. Benson, "Modeling localized failure with arbitrary Lagrangian Eulerian methods," *Computational Mechanics,* vol. 49, no. 2, pp. 197-212, 2012.

[39] W. Riedel, M. Wicklein, and K. Thoma, "Shock properties of conventional and high strength concrete: Experimental and mesomechanical analysis," *International Journal of Impact Engineering,* vol. 35, no. 3, pp. 155-171, 2008.

[40] S. B. Moorhead, "THE LATEST IN SHIP WEAPON LA

UNCHERS-THE VERTICAL LAUNCHING SYSTEM," *Naval Engineers Journal,* vol. 93, no. 2, pp. 90-96, 1981.

[41] J. J. Yagla, "INTERNAL BALLISTICS OF WEAPON LA UNCHING SYSTEMS," *Naval Engineers Journal,* vol. 95, no. 3, pp. 178-191, 1983.

[42] J. BERTIN, R. BERTIN, A. YUNG, and G. SOOHOO, "The launch-tube flow-field for a vertical launching system." p. 332.

[43] K.-S. Lee, S.-K. Hong, and S.-O. Park, "Supersonic jet impingement Navier-Stokes computations for vertical launching system design applications," *Journal of Spacecraft Rockets,* vol. 41, no. 5, pp. 735-744, 2004.

[44] S. Saha, and D. Chakraborty, "Plume-Ducting System Design of Vertical Launcher Using Computational-Fluid-Dynamics Tools," *Journal of Spacecraft Rockets,* vol. 50, no. 3, pp. 715-718, 2013.

[45] W. Cai, P. Thakre, and V. Yang, "A model of AP/HTPB composite propellant combustion in rocket-motor environments," *Combustion Science Technology,* vol. 180, no. 12, pp. 2143-2169, 2008.

[46] B. J. McBride, and S. Gordon, *Computer Program for Calculation of Complex Chemical Equilibrium Compositions and Applications: II*: Nationa Aeronautics and Space Administration, Office of Management, Scientific and Technical Information Program, 1996.

[47] B. Kim, J. Park, K.-C. Lee, and J. J. Yoh, "A reactive flow model for heavily aluminized cyclotrimethylene-trinitramine," *Journal of Applied Physics,* vol. 116, no. 2, pp. 023512, 2014.

[48] B. Kim, M. Kim, and J. J. Yoh, "Shock to detonation transition analysis using experiments and models," *Proceedings of the Combustion Institute,* vol. 36, no. 2, pp. 2699-2707, 2017.

[49] W. Kim, M.-c. Gwak, and J. J. Yoh, “Formation of double front detonations of a condensed-phase explosive with powdered aluminium,” *Combustion Theory Modelling,* vol. 22, no. 2, pp. 378-393, 2018.

[50] B. Kim, J. Park, and J. J. Yoh, “Analysis on shock attenuation in gap test configuration for characterizing energetic materials,” *Journal of Applied Physics,* vol. 119, no. 14, pp. 145902, 2016.

[51] B. Kim, S.-g. Jang, and J. J. Yoh, “A full-scale hydrodynamic simulation of energetic component system,” *Computers Fluids,* vol. 156, pp. 368-383, 2017.

[52] B. Kim, H. Yu, and J. J. Yoh, “Ignition sensitivity study of an energetic train configuration using experiments and simulation,” *Journal of Applied Physics,* vol. 123, no. 22, pp. 225901, 2018.

[53] W. Kim, M.-c. Gwak, Y.-h. Lee, and J. J. Yoh, “A two-phase model for aluminized explosives on the ballistic and brisance performance,” *Journal of Applied Physics,* vol. 123, no. 5, pp. 055902, 2018.

[54] G. Roy, S. Frolov, A. Borisov, and D. Netzer, “Pulse detonation propulsion: challenges, current status, and future perspective,” *Progress in Energy Combustion Science,* vol. 30, no. 6, pp. 545-672, 2004.

[55] P. G. Harris, R. Ripley, and S. Guzik, “Pulse detonation engine as a ramjet replacement,” *Journal of propulsion Power,* vol. 22, no. 2, pp. 462-473, 2006.

[56] N. Smirnov, and V. Nikitin, “Modeling and simulation of hydrogen combustion in engines,” *International Journal of Hydrogen Energy,* vol. 39, no. 2, pp. 1122-1136, 2014.

[57] N. Tsuboi, Y. Watanabe, T. Kojima, and A. K. Hayashi,

"Numerical estimation of the thrust performance on a rotating detonation engine for a hydrogen–oxygen mixture," *Proceedings of the Combustion Institute,* vol. 35, no. 2, pp. 2005-2013, 2015.

[58] F. K. Lu, and E. M. Braun, "Rotating detonation wave propulsion: experimental challenges, modeling, and engine concepts," *Journal of Propulsion Power,* vol. 30, no. 5, pp. 1125-1142, 2014.

[59] K. Wang, W. Fan, X.-d. Zhu, Y. Yan, and Z. Gao, "Experimental investigations on effects of wall-temperature on performance of a pulse detonation rocket engine," *Experimental Thermal Fluid Science,* vol. 48, pp. 230-237, 2013.

[60] M.-H. Wu, T.-H. J. J. o. M. Lu, and Microengineering, "Development of a chemical microthruster based on pulsed detonation," vol. 22, no. 10, pp. 105040, 2012.

[61] N. Smirnov, V. Betelin, V. Nikitin, Y. G. Phylippov, and J. Koo, "Detonation engine fed by acetylene–oxygen mixture," *Acta Astronautica,* vol. 104, no. 1, pp. 134-146, 2014.

[62] J. A. Karnesky, "Detonation induced strain in tubes," California Institute of Technology, 2010.

[63] B. Singh, A. Kumar, and J. Singh, "Reflection of generalized thermoelastic waves from a solid half-space under hydrostatic initial stress," *Applied Mathematics Computation*

vol. 177, no. 1, pp. 170-177, 2006.

[64] K. Kailasanath, "Recent developments in the research on pulse detonation engines," *AIAA journal,* vol. 41, no. 2, pp. 145-159, 2003.

[65] Z. C. Owens, and R. K. Hanson, "The influence of wall heat transfer, friction, and condensation on detonation tube

performance," *Combustion Science Technology*
vol. 182, no. 8, pp. 1104-1140, 2010.
[66] Y. Saiki, and Y. Suzuki, "Effect of wall surface reaction on a methane-air premixed flame in narrow channels with different wall materials," *Proceedings of the Combustion Institute,* vol. 34, no. 2, pp. 3395-3402, 2013.
[67] S.-C. Tang, "Dynamic response of a tube under moving pressure," *Journal of the Engineering Mechanics Division,* vol. 91, no. 5, pp. 97-122, 1965.

초 록

기존에 수행되어온 유체-구조 연성 해석은 대부분 유동의 화학 반응을 고려하지 않는 비반응성 유동과 구조체의 상호작용을 해석해 왔다. 이는 폭발이나 연소 같은 화학반응을 동반하는 고온, 고압의 유동과 구조의 연성 해석 시에 구조체의 대변형이 일어나기 때문이다. 기존의 유체-구조 연성 해석 기법으로 급격하게 변형되는 구조의 형상을 즉각적으로 유동장에 적용하는데 매우 많은 계산 시간과 오차가 있기 때문에 반응성 유동과 구조의 상호작용을 동시에 해석하는 연구는 많이 수행되지 않았다. 따라서 기존 연구에서는 고정된 구조체에서 해석된 화학반응을 포함한 유동의 온도와 압력을 구조 해석에 적용하는 방법으로 유체-고체 연성 해석을 제한적으로 수행하였다. 이 경우, 구조의 거동에 따라 바뀌는 유동을 해석하지 못하므로 구조에 전달되는 정확한 압력 및 온도 조건을 반영할 수 없다. 특히 3차원의 복잡한 형상에서는 구조 변형을 유동 해석에 적용하기 매우 어렵기 때문에 3차원의 반응성 유동과 구조의 연성 연구는 거의 수행되지 않았다. 따라서 본 연구에서는 화학반응을 포함하는 반응성 유동과 이에 따르는 구조체의 대변형을 함께 해석할 수 있는 기법을 개발하였고 이를 3차원에 확장시키기 위하여 다양한 수치적 기법들을 개발하고 적용하였다. 개발된 해석 기법은 실험 값과 비교하여 그 타당성을 검증하였다.

본 연구에서는 다양한 반응성 유동을 고려하였다. 기체 고에너지

물질인 에틸렌-공기 혼합물, 케로신-공기 혼합물 뿐만 아니라 고체 고에너지 물질인 이방성 PETN과 HMX의 연소 반응 모델을 제시하였다. 기체의 경우 1단계 아레니우스식을 통하여 연소반응을 모사하였고, 고체의 경우 변형된 이방성 I&G 모델을 사용하여 충격 방향에 따른 연소 특성을 해석하였다. 개발된 연소 모델은 C-J 조건 및 데토네이션 셀 크기를 비교 검증 하였다. 구조체 변형은 오일러리안과 라그랑지안의 기반의 구조 해석 방식을 사용하여 정확한 구조해석을 수행하였으며 테일러 충격문제를 실험값과 비교하여 검증하였다. 반응성 유동과 구조체의 경계면 추적과 경계값 설정을 위하여 각각 레벨셋 기법과 가상유체기법을 활용하였다. 다물질 해석의 적절성을 검증하기 위하여, 유동장 내에서의 외팔보의 움직임과 데토네이션 하중에 의한 관 변형 문제를 이론값 및 실험값과 비교하여 검증하였다. 3차원에서의 해석을 위하여 STL 파일을 레벨로 변환하는 알고리즘을 개발 하였으며 계산 시간 단축을 위하여 적응적 격자 세분화 기법 및 병렬 처리 기법을 적용하였다.

개발된 코드를 바탕으로 다양한 열부하 시스템의 반응성 유동 및 구조의 상호작용을 해석하였다. 수직발사대 내부에서 발사되는 로켓 화염에 의해 변형되는 발사대 하부의 후방 덮개 거동을 해석 하였다. 해석 결과는 실험값과 비교하여 검증하였고, 해석 결과를 통해 후방 덮개의 변형이 유동에 미치는 영향을 확인 하였다. 또한 2차원으로 단순화 할 수 없는 3차원 벙커 내부에서 발생하는 고체 화약의 폭발 현상과 벽면으로 전달되는 압력을 해석하였다. 해석결과는 실험값과 비교하여 검증하였다. 금속관 내부에서의

폭발에 의한 관 변형 해석에서는 관의 온도에 따른 항복응력을 고려하여 해석하였다. 고온의 환경에 노출되는 Pulse Detonation Engine(PDE)의 경우에는 온도가 고려된 물성치를 사용하여야 정확한 결과를 얻을 수 있고 이론적인 파괴 모델과 비교하여 검증하였다.

유체-고체 연동 해석에 있어서 실제 현상에 보다 근접하기 위하여 떨리는 관 내부에서의 데토네이션 현상을 확인하였다. PDE의 경우, 연속적인 데토네이션이 관 내부를 지나기 때문에 관의 파괴가 일어나지 않더라도 고유진동수로 떨리고 있을 것을 감안하여 고유진동수로 떨리는 관 내부에서의 데토네이션을 해석하였다. 이를 통해 데토네이션의 전파가 관의 변형에 영향을 받는 것을 확인하였다.

주요어: 가연성 기체 혼합물, 고체 폭약, 데토네이션, 탄소성 금속, 다물질 해석, 유체−고체 연성 해석

학 번: 2014−30357